



Defense Threat Reduction Agency  
8725 John J. Kingman Road, MS 6201  
Fort Belvoir, VA 22060-6201



DTRA-TR-03-3

# TECHNICAL REPORT

## *Near Field and Regional Modeling of Explosions at the Degelen Test Site*

Approved for public release; distribution is unlimited.

January 2006

DTRA 01-00-C-0050

J.L. Stevens, et al.

Prepared by:  
Science Applications International  
Corporation  
10260 Campus Point Drive  
San Diego, California 92121

## **DESTRUCTION NOTICE**

**FOR CLASSIFIED** documents, follow the procedures in DoD 5550.22-M, National Industrial Security Program Operating Manual, Chapter 5, Section 7 (NISPOM) or DoD 5200.1-R, Information Security Program Regulation, Chapter 1X.

**FOR UNCLASSIFIED** limited documents, destroyed by any method that will prevent disclosure of contents or reconstruction of the document.

Retention of this document by DoD contractors is authorized in accordance with DoD 5220.22-M, Industrial Security Manual.

PLEASE NOTIFY THE DEFENSE THREAT REDUCTION AGENCY, ATTN: BDLMI, 8725 JOHN J. KINGMAN ROAD, MS-6201, FT BELVOIR, VA 22060-6201, IF YOUR ADDRESS IS INCORRECT, IF YOU WISH IT DELETED FROM THE DISTRIBUTION LIST, OR IF THE ADDRESSEE IS NO LONGER EMPLOYED BY YOUR ORGANIZATION.



## DISTRIBUTION LIST UPDATE

This mailer is provided to enable DTRA to maintain current distribution lists for reports. (We would appreciate you providing the requested information.)

- ☐ Add the individual listed to your distribution list.
- ☐ Delete the cited organization/individual.
- ☐ Change of address.

**Note:**

Please return the mailing label from the document so that any additions, changes, corrections or deletions can be made easily. For distribution cancellation or more information call DTRA/BDLMI (703) 767-4725.

NAME: \_\_\_\_\_

ORGANIZATION: \_\_\_\_\_

**OLD ADDRESS**

**NEW ADDRESS**

\_\_\_\_\_  
\_\_\_\_\_  
\_\_\_\_\_

\_\_\_\_\_  
\_\_\_\_\_  
\_\_\_\_\_

TELEPHONE NUMBER: (    ) \_\_\_\_\_

**DTRA PUBLICATION NUMBER/TITLE**

**CHANGES/DELETIONS/ADDITONS, etc.**

*(Attach Sheet if more Space is Required)*

\_\_\_\_\_  
\_\_\_\_\_  
\_\_\_\_\_

\_\_\_\_\_  
\_\_\_\_\_  
\_\_\_\_\_

DTRA or other GOVERNMENT CONTRACT NUMBER: \_\_\_\_\_

CERTIFICATION of NEED-TO-KNOW BY GOVERNMENT SPONSOR (if other than DTRA):

SPONSORING ORGANIZATION: \_\_\_\_\_

CONTRACTING OFFICER or REPRESENTATIVE: \_\_\_\_\_

SIGNATURE: \_\_\_\_\_

DEFENSE THREAT REDUCTION AGENCY  
ATTN: BDLMI  
8725 John J Kingman Road, MS 6201  
Fort Belvoir, VA 22060-6201

DEFENSE THREAT REDUCTION AGENCY  
ATTN: BDLMI  
8725 John J Kingman Road, MS 6201  
Fort Belvoir, VA 22060-6201

REPORT DOCUMENTATION PAGE			Form Approved OMB No. 0704-0188	
Public reporting burden for this collection of information is estimated to average 1 hour per response, including the time for reviewing instructions, searching existing data sources, gathering and maintaining the data needed, and completing and reviewing the collection of information. Send comments regarding this burden estimate or any other aspect of this collection of information, including suggestions for reducing this burden, to Washington Headquarters Services, Directorate for Information Operations and Reports, 1215 Jefferson Davis Highway, Suite 1204, Arlington, VA 22202-4302, and to the Office of Management and Budget, Paperwork Reduction Project (0704-0188), Washington, DC 20503				
1. AGENCY USE ONLY (Leave Blank)	2. REPORT DATE 07-11-2005	3. REPORT TYPE AND DATES COVERED Technical, 5/23/2000 - 12/31/2002		
4. TITLE AND SUBTITLE Near Field and Regional Modeling of Explosions at the Degelen Test Site		5. FUNDING NUMBERS C - DTRA01-00-C-0050 PE - 463D PR - BI TA - AD WU - DHEA109		
6. AUTHORS J.L. Stevens, N. Rimer H. Xu, G.E. Baker S.M. Day				
7. PERFORMING ORGANIZATION NAME(S) AND ADDRESS(ES) Science Applications International Corporation 10260 Campus Point Drive San Diego, CA 92121		8. PERFORMING ORGANIZATION REPORT NUMBER  SAIC 02/2050		
9. SPONSORING / MONITORING AGENCY NAME(S) AND ADDRESS(ES) Defense Threat Reduction Agency 8725 John J. Kingman Road, MS 6201 Fort Belvoir, VA 22060-6201 TDND/D. Barber		10. SPONSORING / MONITORING AGENCY REPORT NUMBER  DTRA-TR-03-3		
11. SUPPLEMENTARY NOTES  This work was sponsored by the Defense Threat Reduction Agency under RDT&E RMC code B 463D D BI AD EA109 K500 2590RD.				
12a. DISTRIBUTION / AVAILABILITY STATEMENT  Approved for public release; distribution is unlimited.		12b. DISTRIBUTION CODE		
13. ABSTRACT (Maximum 200 words) We develop improved dynamic failure models constrained by a large data set of near field waveforms and parametric data from Soviet explosions at the Degelen test site. The Institute for the Dynamics of the Geospheres (IDG) provided digitized data from 23 nuclear tests with yields from 0.3 to 125 KT. The complete data set consists of 77 near field waveforms recorded underground at shot depth and 115 near regional waveforms recorded at 9 stations between 10 and 100 km distance. This data set provides a rare opportunity to observe and model the seismic wavefield as it evolves from the near field to regional distances. We find two distinctly different types of near field waveforms: "narrow-pulse" waveforms suggest that there is little if any strength reduction after failure from this subset of explosions; "wide-pulse" waveforms are more consistent with U.S. experience that material strength is reduced substantially by shock. We implement and test a numerical model of acoustic fluidization in nonlinear explosion simulations. Acoustic fluidization is a possible physical mechanism for strength reduction, and we compare it with other strength reduction mechanisms. Differences in data fit between strength reduction mechanisms are insufficient to uniquely identify which mechanisms is operating.				
14. SUBJECT TERMS Nuclear Explosion Degelen Acoustic fluidization Nuclear Monitoring Rock Mechanics			15. NUMBER OF PAGES 90	
			16. PRICE CODE	
17. SECURITY CLASSIFICATION OF REPORT UNCLASSIFIED	18. SECURITY CLASSIFICATION OF THIS PAGE UNCLASSIFIED	19. SECURITY CLASSIFICATION OF ABSTRACT UNCLASSIFIED	20. LIMITATION OF ABSTRACT SAR	

## SUMMARY

The objective of this research program is to improve the capability to predict the seismic source characteristics of underground explosions in rock. We have developed improved dynamic failure models constrained by a large unique data set of near field waveforms and parametric data from historic Soviet explosions at the Degelen test site. In addition, we have analyzed regional seismic data along a seismic line located north of the Degelen test site that recorded data at 9 stations spaced approximately evenly from the test site to a distance of about 100 km. This project is a collaborative effort between SAIC and the Russian Institute for the Dynamics of the Geospheres (IDG).

IDG has provided digitized data from 23 nuclear tests at the Degelen test site. The complete data set consists of 77 near field waveforms recorded underground at shot depth and 115 near regional seismic records (283 seismic records including multiple components or recordings). Most seismic records include both a vertical and radial waveform. The events in this data set have explosive yields ranging from 0.3 kt up to 125 kt. This data set provides a rare opportunity to observe and model the seismic wavefield of the explosions as they evolve from the near field of the explosion out to regional distances. Our goal is to develop material models that are consistent with the data and have a realistic physical basis. Work at SAIC has focused on implementation and testing of improved numerical modeling procedures and simulation of near regional data. We have implemented and tested acoustic fluidization as a physical mechanism for strength reduction in nonlinear explosion simulations. Near regional data has been modeled using wave number integration. We also have compared the Degelen data with similar data from the Nevada Test Site (NTS) PILEDRIVER and Hardhat explosions in granitic rocks.

To more easily compare these data, we scaled all of the Degelen and NTS near-field particle velocity records to the same explosive yield. These data were then organized based on yield-scaled pulse widths and pulse shapes. The NTS events, the 8 Degelen explosions with yields greater than 17 kt, and some of the lower yield events, gave records with positive and negative pulse widths that strongly suggest free-field ground motion. The records from a few of the other, lowest yield explosions have unusual shapes that indicate probable contamination by nearby fault or block motion. There is considerable variation among the pulse amplitudes and shapes of the free-field data. Some of this variation, particularly the consistent differences in pulse width, indicates some interesting and potentially important differences in physical mechanisms operating for subsets of explosions. Peak velocities at a given scaled range from the free-field events vary by a factor of 4, while positive pulse widths from Degelen vary by a factor of 3. Even the widest pulse widths at Degelen, however, with one exception, are narrower than the pulse widths from the NTS events. Three of the higher yield explosions from Degelen, with yields of 125, 100, and 23.7 kt, form a "narrow pulse set" that were numerically simulated without the use of any strength reduction mechanism. The other 5 higher yield Degelen explosions, with yields from 18 to 78 kt, and some of the lower yield events, form a "wide pulse set", encompassing a gradation of pulse widths, that require the use of a gradation of strength reduction parameters in the numerical simulations. Simulation of the even wider pulses from the NTS explosions may be accomplished using different parameters in the same strength reduction model. We are able to simulate the near field pulses from both the NTS and Degelen explosions

using either the acoustic fluidization strength reduction model or a shock damage model that relates the magnitude of strength reduction in a rock element to the maximum shear strain seen during the ground motion.

The effects on pulse widths resulting from changes in Degelen site material properties due to earlier nearby explosions has yet to be quantified. Our analyses to date of both regional waveforms and body wave magnitudes show only small differences in amplitudes between the explosions that show wide and narrow near field particle velocity pulses. A possible explanation for this anomaly is that the near field data, which are recorded at shot level, may be more affected by cracks and joints than the downgoing waves which control the far field body waves. The data set of near field and regional waveforms is being delivered to DTRA and the Center for Monitoring Research together with this report.

## **PREFACE**

We thank Boris Ivanov and Gevorg Kocharyan of the Institute for the Dynamics of the Geospheres in Moscow, Russia for the use of their data and for their work on this project.



## CONVERSION TABLE

Conversion factors for U.S. Customary to metric (SI) units of measurement

MULTIPLY TO GET	BY	TO GET DIVIDE
angstrom	1.000 000 X E -10	meters (m)
atmosphere (normal)	1.013 25 X E +2	kilo pascal (kPa)
bar	1.000 000 X E +2	kilo pascal (kPa)
barn	1.000 000 X E -28	meter <sup>2</sup> (m <sup>2</sup> )
British thermal unit (thermochemical)	1.054 350 X E +3	joule (J)
calorie (thermochemical)	4.184 000	joule (J)
cal (thermochemical)/cm <sup>2</sup>	4.184 000 X E -2	mega joule/m <sup>2</sup> (MJ/m <sup>2</sup> )
curie	3.700 000 C E +1	* giga becquerel (GBq)
degree (angle)	1.745 329 X E -2	radian (rad)
degree Fahrenheit	$t_k = (t_f + 459.67)/1.8$	degree kelvin (K)
electron volt	1.602 19 X E -19	joule (J)
erg	1.000 000 X E -7	joule (J)
erg/second	1.000 000 X E -7	watt (W)
foot	3.048 000 X E -1	meter (m)
foot-pound-force	1.355 818	joule (J)
gallon (U.S. liquid)	3.785 412 X E -3	meter <sup>3</sup> (m <sup>3</sup> )
inch	2.540 000 X E -2	meter (m)
jerk	1.000 000 X E +9	joule (J)
joule/kilogram (J/kg) (radiation dose absorbed)	1.000 000	Gray (Gy)
kilotons	4.183	terajoules
kip (1000 lbf)	4.448 222 X E +3	newton (N)
kip/inch <sup>2</sup> (ksi)	6.894 757 X E +3	kilo pascal (kPa)
ktap	1.000 000 X E +2	newton-second/m <sup>2</sup> (N-s/m <sup>2</sup> )
micron	1.000 000 X E -6	meter (m)
mil	2.540 000 X E -5	meter (m)
mile(international)	1.609 344 X E +3	meter (m)
ounce	2.834 952 X E -2	kilogram (kg)
pound-force (lbs avoirdupois)	4.448 222	newton (N)
pound-force inch	1.129 848 X E -1	newton-meter (N•m)
pound-force/inch	1.751 268 X E +2	newton/meter (N/m)
pound-force/foot <sup>2</sup>	4.788 026 X E -2	kilo pascal (kPa)
pound-force/inch <sup>2</sup> (psi)	6.894 757	kilo pascal (kPa)
pound-mass (lbm avoirdupois)	4.535 924 X E -1	kilogram (kg)
pound-force/foot <sup>2</sup> (moment of inertia)	4.214 011 X E -2	kilogram-meter <sup>2</sup> (kg•m <sup>2</sup> )
pound-mass/foot <sup>3</sup>	1.601 846 X E +1	kilogram-meter <sup>3</sup> (kg•m <sup>3</sup> )
rad (radiation dose absorbed)	1.000 000 X E -2	** Gray (Gy)
roentgen	2.579 760 X E -4	coulomb/kilogram (C/kg)
shake	1.000 000 X E -8	second (s)
slug	1.459 390 X E +1	kilogram (kg)
torr (mm HG, 0°C)	1.333 22 X E -1	kilo pascal (kPa)

\* The becquerel (Bq) is the SI unit of radioactivity; 1Bq = 1 event/s.

\*\* The Gray (GY) is the SI unit of absorbed radiation.

A more complete listing of conversions may be found in "Metric Practice Guide E 380-74," American Society for Testing and Materials.



## TABLE OF CONTENTS

SECTION	PAGE
SUMMARY .....	ii
PREFACE .....	iv
CONVERSION TABLE .....	v
FIGURES .....	vii
TABLES .....	xi
1 INTRODUCTION .....	1
2 DEGELEN NEAR FIELD AND NEAR REGIONAL SEISMIC DATA.....	4
2.1 Degelen RDP Comparisons .....	23
2.2 Near Regional Data Analysis.....	27
3 NUMERICAL MODELING OF U.S. EXPLOSIONS .....	32
3.1 Results for YF-SS Model Combination .....	37
3.2 The Revised Acoustic Fluidization Model .....	39
3.3 Results for SA-AF Model Combination .....	40
3.4 Results for YF-AF Model Combination .....	42
4 NUMERICAL MODELING OF DEGELEN EXPLOSIONS .....	45
4.1 Degelen Results for SA-SS Model Combination .....	46
4.2 Degelen Results for YF-SS Model Combination .....	52
4.3 Degelen Results for YF-AF Model Combination.....	52
4.4 Degelen Results for SA-AF Model Combination.....	53
4.5 Narrow Pulse Degelen Simulations .....	67
4.5.1 Results for Different Depths of Burial .....	67
4.5.2 Seismic Source Functions for Degelen Models .....	70
5 CONCLUSIONS AND RECOMMENDATIONS .....	71
6 REFERENCES .....	73
DISTRIBUTION LIST.....	DL-1

## FIGURES

Figure	Page
1 Particle velocity measurements at working point depth from PILEDRIIVER compared with data from a calculation using the laboratory strength of granite with no weakening. ....	2
2 Particle velocity measurements at working point depth from PILEDRIIVER compared to numerical simulation pile570 using the effective stress law. ....	3
3 Map showing the locations of the former Soviet Degelen and Balapan test sites, faults, and seismic stations in the region. ....	4
4 Near field (left) and near regional seismic (right) waveforms from the 1987/07/17 event. ....	6
5 Near field (left) and near regional seismic (right) waveforms from the 1988/11/23 event. ....	7
6 Near field (left) and near regional seismic (right) waveforms from the 1988/04/22 event. ....	7
7 Synthetic and observed seismograms for the 1987/07/17 event. Synthetics were created using wavenumber integration and were low pass filtered at 2 Hz. ....	8
8 (a) Peak particle velocity vs. scaled range for historic data from U.S. and French explosions (left) and for the 19 Degelen digitized explosions (right). The solid line is the prediction from the pile570 effective stress simulation shown earlier in Figure 2. The dashed line is the predicted peak velocity for the Degelen DE12 simulation using the Sammis failure model plus frictional strength reduction (Rimer, et al, 1999). (b) Peak displacement vs. scaled range for historic data from U.S. and French explosions (left) and for the 12 Degelen explosions that could be integrated to peak displacement (right). The solid line is the prediction from the pile570 effective stress simulation shown earlier in Figure 2. The dashed line is the predicted peak velocity for the Degelen DE12 simulation using the Sammis failure model plus frictional strength reduction (Rimer, et al, 1999). ....	11
9 Peak particle velocity vs. scaled range for the 14 Degelen explosions designated as showing free-field pulse shapes (left), and for the full set of 19 Degelen explosions, as already shown in Figure 8a (right). The solid, pile570, and dashed, DE12, simulation results are shown as in Figure 8a. ....	13

## FIGURES (Continued)

10	Particle velocity pulses at the smaller (scaled to PILEDRIVER) ranges from the “wide pulse” Degelen data subset compared with the results of simulation DE12 (solid curves). .....	14
11	Particle velocity pulses at the larger (scaled to PILEDRIVER) ranges from the “wide pulse” Degelen data subset compared with the results of simulation DE12 (solid curves). .....	16
12	Particle velocity pulses at (scaled to PILEDRIVER) ranges from the “narrow pulse” Degelen data subset compared with the results of simulation DE12 (solid curves).....	18
13	Comparisons between particle velocity pulses at three ranges from PILEDRIVER and Degelen “wide pulse” explosion records (scaled to 62 kt) at nearby scaled ranges. ....	22
14	Scaled-to-62 kt particle velocity records (left) and computed RDPs (right) from simulation DE12 (solid curves) and from the scaled-to-62 kt range of 704 m from the 19 kt Degelen explosion (dashed curves).....	24
15	Arrival times at near-field gauge locations.....	26
16	Log of the P wave amplitude vs. distance for five events with wide velocity pulses in the near field (polygonal symbols) and three events with narrow velocity pulses in the near field (+, x, and *). Most regression curves have a similar slope, and we use the average, weighted by the number of points in each event, to correct all records back to 10 km distance from the source. ....	27
17	The same data as in Figure 16, with the best fit lines for the average distance correction. The separation between lines reflects the dependence of amplitude on yield. ....	28
18	Mean log amplitude vs. log yield for 5 wide pulse (squares) and 3 narrow pulse events (diamonds). Confidence intervals are one standard deviation. There is no apparent separation of the two groups, as the very optimistic confidence intervals overlap nearly completely. ....	29
19	Distance and yield corrected log amplitudes of vertical seismograms recorded from 13 to 84 km distance. Open symbols (+, *, and x) are used for events that have narrow velocity pulses in the near field, and polygons are used for events that have wide pulses in the near field.....	29
20	Mean values with one standard deviation confidence intervals for each event, for the data shown in Figure 19. ....	30

## FIGURES (Continued)

21	$m_b$ vs. yield for all 13 Degelen events with known $m_b$ and yield. The best fit line is $mb=0.72\log_{10}Y+4.53$ .....	30
22	$m_b$ vs. yield for the three narrow pulse events. The best fit line is $m_b=0.67\log_{10}Y+4.67$ .....	31
23	$m_b$ vs. yield for the 7 wide-pulse Degelen events that show good free-field near field data. The best fit line is $mb=0.63\log_{10}Y+4.60$ . ....	31
24	Calculated particle velocity pulses at four ranges for Run PD10 and PILEDRIIVER measurements. ....	35
25	Calculated particle velocity pulses at four ranges for YF-SS case 9 vs. PILEDRIIVER data.....	38
26	Calculated particle velocity pulses at four ranges for best fit YF-SS case 10 vs. PILEDRIIVER data. ....	39
27	Calculated particle velocity pulses at four ranges for best fit SA-AF case 7 vs. PILEDRIIVER data.....	42
28	Calculated particle velocity pulses at four ranges for best fit YF-AF case 4 vs. PILEDRIIVER data.....	43
29	Comparison between particle velocity pulses at the smaller scaled ranges from the wide pulse Degelen data subset and the results of the best fit simulation (case 7) using the SA-SS model combination (the solid curves).....	48
30	Comparison between particle velocity pulses at the larger scaled ranges from the wide pulse Degelen data subset and the results of the best fit simulation (case 7) using the SA-SS model combination (the solid curves).....	50
31	Comparison between particle velocity pulses at the smaller scaled ranges from the wide pulse Degelen data subset and the results of the best fit simulation (case 9) using the YF-SS model combination (the solid curves). ....	54
32	Comparison between particle velocity pulses at the larger scaled ranges from the wide pulse Degelen data subset and the results of the best fit simulation (case 9) using the YF-SS model combination (the solid curves).....	56
33	Comparison between particle velocity pulses at the smaller scaled ranges from the wide pulse Degelen data subset and the results of the best fit simulation (case 7) using the YF-AF model combination (the solid curves). ....	59



## FIGURES (Continued)

34	Comparison between particle velocity pulses at the larger scaled ranges from the wide pulse Degelen data subset and the results of the best fit simulation (case 7) using the YF-AF model combination (the solid curves).....	61
35	Comparison between particle velocity pulses at the smaller scaled ranges from the wide pulse Degelen data subset and the results of the best fit simulation (case 3) using the SA-AF model combination (the solid curves). ....	63
36	Comparison between particle velocity pulses at the larger scaled ranges from the wide pulse Degelen data subset and the results of the best fit simulation (case 3) using the SA-AF model combination (the solid curves).....	65
37	Comparison between particle velocity pulses from the narrow pulse Degelen data subset and the results of the best fit simulation (case 2 of Table 12) using the YF-AF model combination with acoustic fluidization turned off (the solid curves). ....	68
38	Calculated source spectra (reduced velocity potential) for explosions in Degelen granite using four combinations of nonlinear models, and a calculated source spectrum for the US explosion Piledriver (evaluated at 62 KT). ....	70

## TABLES

Table	Page
1	Degelen events with near field and/or seismic records, and waveforms digitized. Some stations have multiple recordings. Total number of digitized recordings, including separate components and multiple records from a single site, are shown in parentheses. Explosion yield, ISC $m_b$ , and depth of burial are shown (where there are 2 depths, the smaller indicates slant range to a free surface).....5
2	Peak RDPs (scaled to 62 kt) computed from the Degelen particle velocity data and computed from the empirical Mueller-Murphy (MM) source for 62 kt nuclear explosions at granite sites. ....24
3	P-wave velocities computed from arrival time data. ....26
4	United States explosions in granite.....32
5	Results for PILEDRIIVER simulations using the YF-SS model combination with $epw = 500 \text{ ergs/cm}^3$ .....37
6	Results for PILEDRIIVER simulations using the SA-AF model combination.....41
7	Results for PILEDRIIVER simulations using the YF-AF model combination with $epw = 500 \text{ ergs/cm}^3$ . ....42
8	Degelen modeling constraints (scaled to 62kt).....45
9	Simulation results and comparisons between some characteristics of measured Degelen pulses and best fit wide-pulse simulations using 4 combinations of failure/rubblization and strength reduction models. ....46
10	Results for Degelen wide pulse simulations using the SA-SS model combination.....47
11	Results for Degelen wide pulse simulations using the YF-SS model combination.....52
12	Results for Degelen wide pulse simulations using the YF-AF model combination.....53
13	Results for Degelen wide pulse simulations using the SA-AF model combination.....58
14	Results of overburden variations for Degelen wide pulse simulations using the YF-AF model combination. ....67
15	Results of overburden variations for Degelen narrow pulse simulations using the YF-AF model combination with acoustic fluidization turned off. ....67

## SECTION 1 INTRODUCTION

The main objectives of this joint project between SAIC and IDG are to obtain a better understanding of the explosion source function, and to model the evolution of the explosion source from the close in hydrodynamic region out to near regional distances. To accomplish this, we have modeled a unique data set of near source and near regional data provided by IDG.

Empirical and numerical models of explosion sources do a fairly good job of matching observed seismic signals, however the physical basis for the explosion source is still not well understood. In particular, numerical models of explosion sources developed using laboratory measurements of rock properties fail to predict observed near field ground motion in hardrock. This is illustrated in Figure 1, which shows the near field waveforms from the explosion PILEDRIIVER together with waveforms from a finite difference calculation of the near field ground motion made using rock properties measured in the laboratory. The basic problem is that the strength of the rock measured in the laboratory is much larger than the apparent strength of the rock as determined from the near field ground motion. Furthermore, additional investigation shows that

1. The strength of the rock is not initially low, but rather decreases dynamically as, or after, the shock wave passes.
2. The strength of the rock is reduced to a level well below that predicted for rubbleized rock under hydrostatic dynamic friction.

A number of solutions to these problems have been proposed over the years, including the effective stress model (Rimer, et al, 1984), and various types of damage models. These models all have the characteristic that the material strength is reduced dynamically to a very low level when it fails. The effective stress model says that the weakness comes from water within the rock matrix, and that the broken rock in effect floats on water that is squeezed out of pores or fractures when the rock fails. Although there are questions about the realism of this physical model, it works fairly well to explain the near field waveforms. Figure 2 shows a comparison of the PILEDRIIVER waveforms with waveforms calculated using the effective stress model. The agreement is quite good, particularly at the closer two stations. Furthermore, when the PILEDRIIVER solution was scaled to the appropriate yield and compared with other U.S. explosions in granite (Hardhat and Shoal), agreement with the observed waveforms was also quite good (Stevens, et al, 1986).

Under a previous DTRA contract, SAIC (at the time Maxwell Technologies) worked together with the IDG and the University of Southern California, to develop improved micro-mechanical material models. IDG provided extensive measurements of material properties close to nuclear and chemical explosions both before and after the explosions were detonated (Rimer, et al, 1998). In addition, we implemented the damage mechanics model which was developed by Prof. Charles Sammis at the University of Southern California into SAIC's nonlinear finite difference codes and used this model to simulate the observed explosion damage and a small set of near



field waveforms that were also provided by IDG. The results of this work are discussed in detail in the final report (Rimer et al, 1999). The damage model referred to above actually applies to the growth and coalescence of cracks just prior to failure, and does not predict what happens to the rock after failure occurs. Calculations using the damage model followed by a rubbleized model with realistic values of friction did not provide enough strength reduction and thus did not match the near field data. We were more successful in matching the data by dropping the coefficient of friction to very low values (as low as 0.02), but this again leaves the question of what physical mechanism could be responsible for these very low values and corresponding low strength.

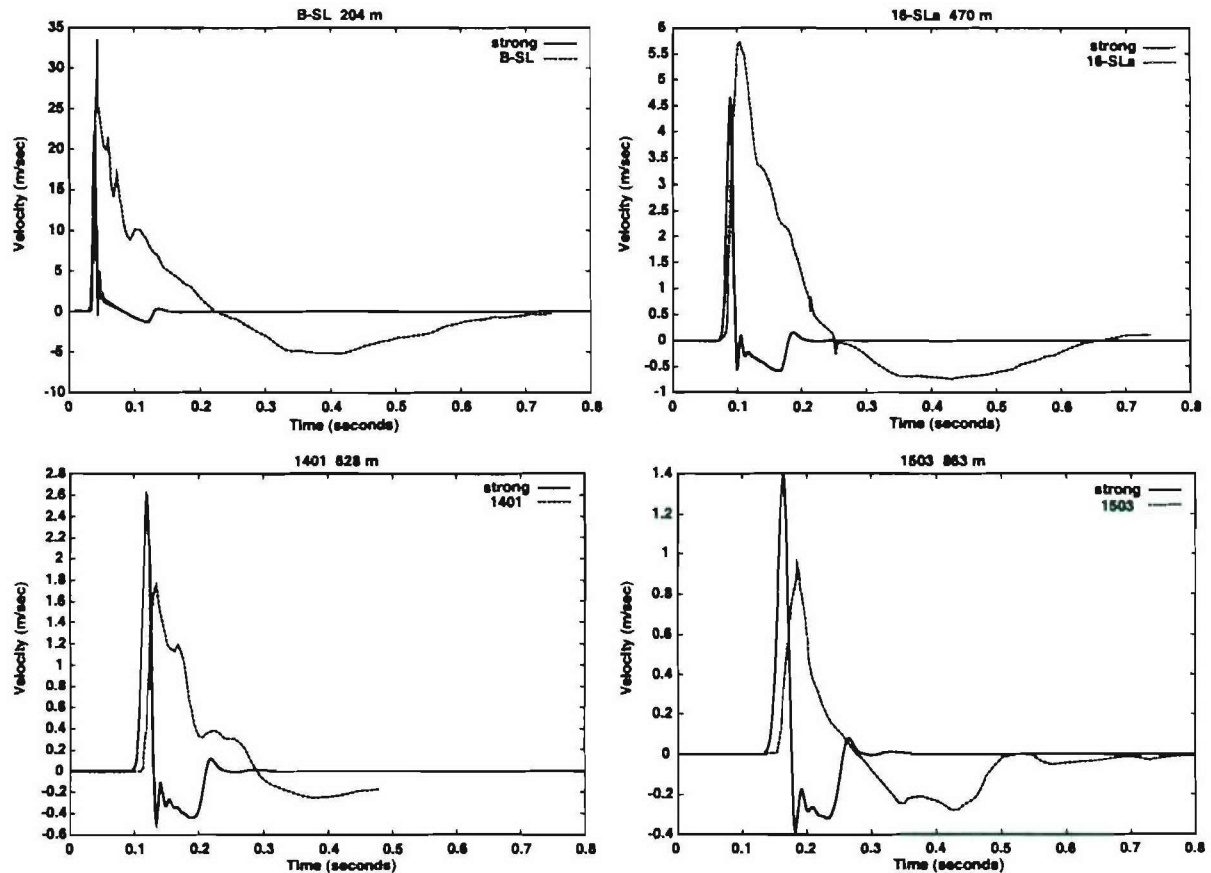
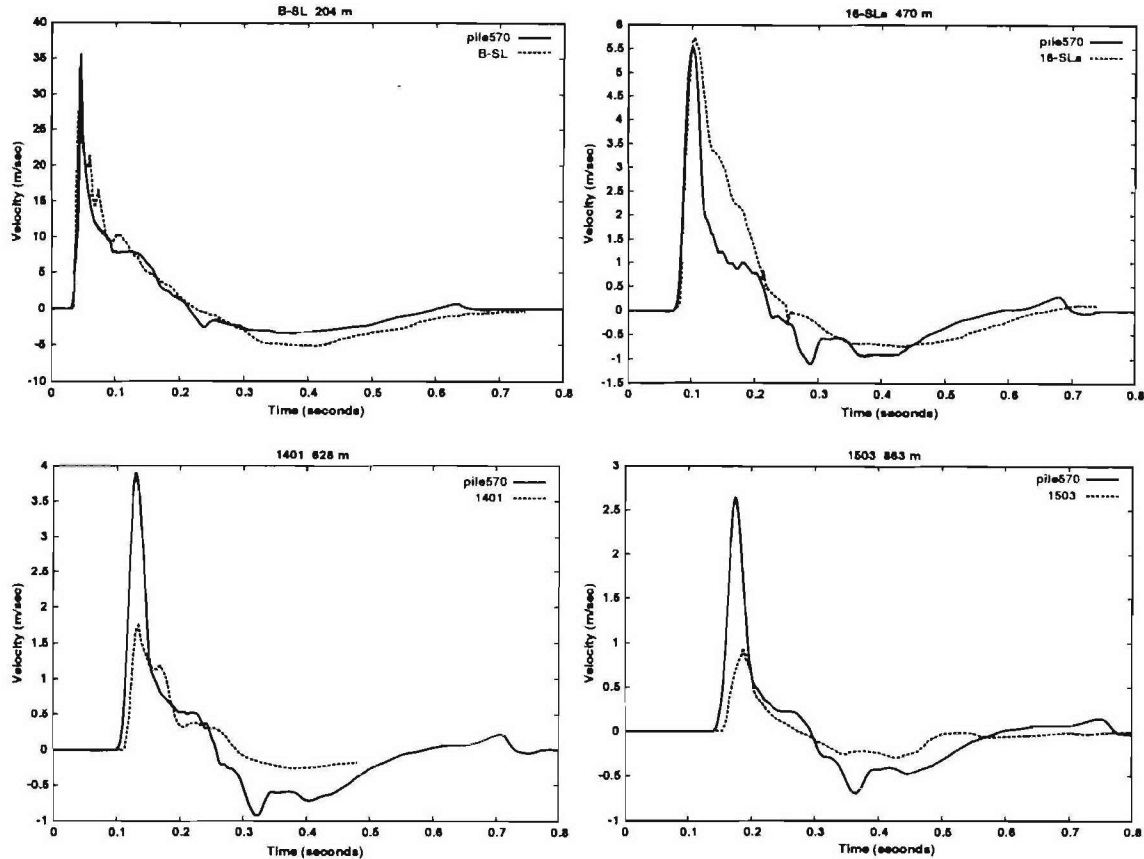


Figure 1. Particle velocity measurements at working point depth from PILEDRIVER compared with data from a calculation using the laboratory strength of granite with no weakening.



**Figure 2.** Particle velocity measurements at working point depth from PILEDRIIVER compared to numerical simulation pile570 using the effective stress law.

A possible answer initially proposed by Melosh (1979) is “acoustic fluidization”. The physics behind this mechanism is that during the fracturing process there is a complex dynamic acoustic wavefield that causes high frequency vibrations in the broken rock. These vibrations cause rapidly changing regions of high and low normal stress, and remove the frictional normal stress from parts of the rock as it moves. Consequently parts of the rock are not confined by the frictional stress and in effect have much lower strength. Acoustic fluidization has been used to explain other phenomena such as landslides and craters (Melosh and Ivanov, 1999), which have been similarly difficult to explain because of anomalously low apparent friction. Initial efforts to include acoustic fluidization in our numerical models for the simulation of the PILEDRIIVER event were described in section 4 of Annual Report No. 1 (Stevens, et al, 2001).

Our most recent efforts to apply the acoustic fluidization strength reduction model to the numerical simulation of the near-field data from explosions at the Degelen site are described in Section 4 of the current report. First, however, we must discuss, in Section 2, our analyses to date of the near-field, near regional seismic, and teleseismic data from the Degelen site, and, in Section 3, our attempts to use numerical simulations of the PILEDRIIVER event to distinguish between various candidate physical models of the failure and strength reduction processes, including acoustic fluidization.

## SECTION 2

### DEGELEN NEAR FIELD AND NEAR REGIONAL SEISMIC DATA

The numerical modeling component of this project is being constrained by a much better data set than has been available in the past. Near field waveforms are only available from a small number of U.S. nuclear tests in hard rock, and until recently, none have been available from the testing program of the former Soviet Union. IDG has near field records from a number of nuclear explosions at the Degelen test site that have been digitized for this project. IDG also provided near source material properties measurements for some of these events. This unique data set places strong constraints on the numerical modeling work, as well as providing data from a new and important area to augment our previous data sets which have come primarily from the western United States. In addition, IDG has data from a seismic line located north of the Degelen test site that was maintained with consistent instrumentation for many years during the Soviet testing program. Figure 3 shows a map illustrating the location of the test sites and the seismic stations. The 9 seismic stations are spread out at approximately even intervals from the Degelen test site out to a distance of about 100 km. IDG also digitized seismic data from these stations for all of the events that have near field records. This provides a rare opportunity to observe and model the seismic wavefield of the explosions as they evolve from the near field of the explosion out to regional distances. The data that IDG has identified for digitization, and the data digitized are listed in Table 1.

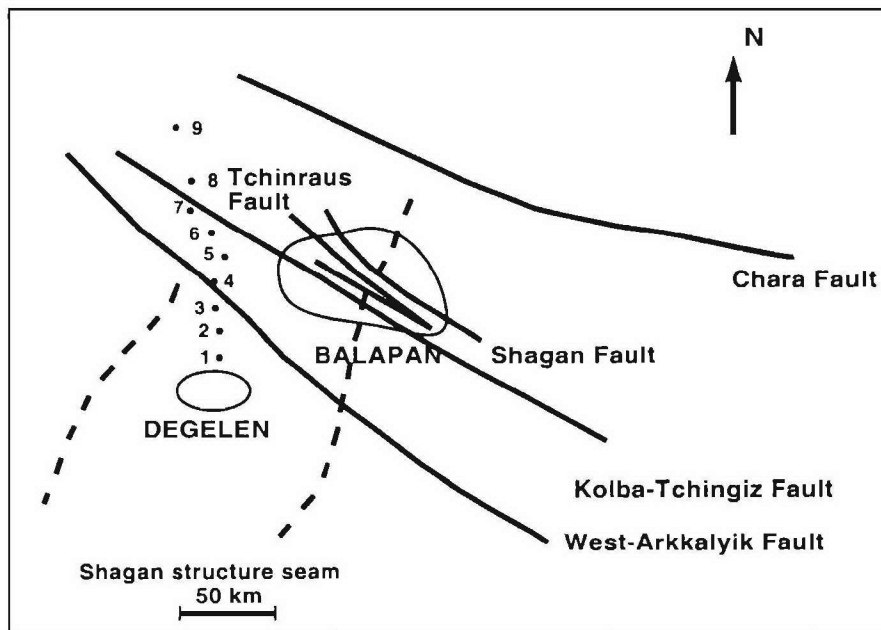


**Figure 3.** Map showing the locations of the former Soviet Degelen and Balapan test sites, faults, and seismic stations in the region.



**Table 1.** Degelen events with near field and/or seismic records, and waveforms digitized. Some stations have multiple recordings. Total number of digitized recordings, including separate components and multiple records from a single site, are shown in parentheses. Explosion yield,  $m_b$ , and depth of burial are shown (where there are 2 depths, the smaller indicates slant range to a free surface). IDG provided explosion yields and depths, and waveform or tabulated data for all events.

Event				Near Field Records			Near Regional Records		
Date	Yield (Kt)	$m_b$ *	Depth of burial, m	No. of near field records	Number digitized	Distance range, m	No. of seismic records	Number digitized	Distance range, km
1964/05/16	23.7	5.6	253/ 262	4	4	150-600	9	peaks	13-79
1965/02/04	18	-	262	4	4	147-750	9	peaks	14-83
1966/02/13	125	6.1	297/ 343	4	4	350-600	9	peaks	14-79
1966/03/20	100	6.0	294/ 320	4	4	300-600	9	peaks	15-84
1968/07/12	6	5.3	172/190	2	2	81-98			
1970/06/28	37	5.7	332/360	2	2 (3)	306-500			
1971/12/15	1.5	4.9	115/145				9	9 (28)	7.4-77
1973/12/31	0.5	-	157	4	4 (5)	110-230			
1974/12/16	3.8	4.8	126	4	2 (5)	100-200			
1978/03/26	30	5.6	260	6	6	76-316			
1980/06/25	0.3	-	152	3	3	155-310			
1980/09/25	2.2	4.77	110	3	3 (6)	100-160			
1981/07/17	9.3	5.16	146	3	3	115-310	8	8 (27)	15-80
1982/12/25	1.7	4.8	112	4	4	90-190			
1984/10/18	1.4	4.5	106	5	5	35-160			
1987/05/06	32	5.6	-				9	9 (28)	13-83
1987/07/17	78	5.8	267	14	14	170-900	7	7 (23)	14.5-84
1987/10/16	1.1	4.6	82	4	4	55-132	8	8 (27)	4-64
1987/12/20	3.2	4.7	105				9	9 (26)	13-83
1988/04/22	2.3	4.9	124	2	2	69-183	3	3 (11)	57-81
1988/10/18	2.5	-	125				9	9 (26)	11-77
1988/11/23	19	5.4	204	4	3	280-475	9	9 (28)	14-83
1989/10/04	1.8	4.7	94	4	4 (5)	45-285	8	8 (25)	16-85

\* magnitude data for explosions before 1986 are from Sykes and Ruggi (1986), after 1986 from ISC.

Figures 4-6 show waveforms for three of the explosions. The near field records show the evolution of the waveform from the nonlinear to linear regions. The near regional records show the evolution of the waveform from 14 to 83 km. Note the strong Rg phase present in several seismograms that persists to quite a long distance. Some of the records end before the start of the Rg phase and therefore do not show it. Figure 7 shows a comparison of synthetic and observed seismograms for three of the near regional waveforms from the 1987/07/17 event. The synthetic seismograms were constructed using wavenumber integration (Luco and Apsel, 1983) using the East Kazakh structure from Stevens (1986). The synthetic seismograms were low-pass filtered at 2 Hz. The persistence of Rg calls into question the explanation of Rg scattering as the source of Lg since that mechanism requires most of Rg to scatter into Lg within a few kilometers of the source.

Figure 8 shows comparisons between near-field peak particle velocity and peak displacement measurements from the first 19 Degelen explosions listed in Table 1 and the corresponding measurements from explosions at the U.S. and French (Hoggar) granite sites. Although expanded scales must be used in the left plot of Figure 8a in order to include all of the PILEDRIVER and SHOAL peak velocity data, both plots include the same solid curve, representing peak velocities from pile570, the effective stress simulation that was shown earlier in Figure 2. Almost all of the historic granite data for both peak velocity and peak displacement, and the Degelen data, lie on or below this prediction. The four shaded triangles in the left plot of Figure 8a are the peak velocities from the records shown in Figures 1 and 2, all from gauges emplaced at the PILEDRIVER source depth of burial. At the first range, the velocity pulse was obtained from

both a particle velocity gauge and an accelerometer that were in excellent agreement out to the latest times plotted

07-17-87

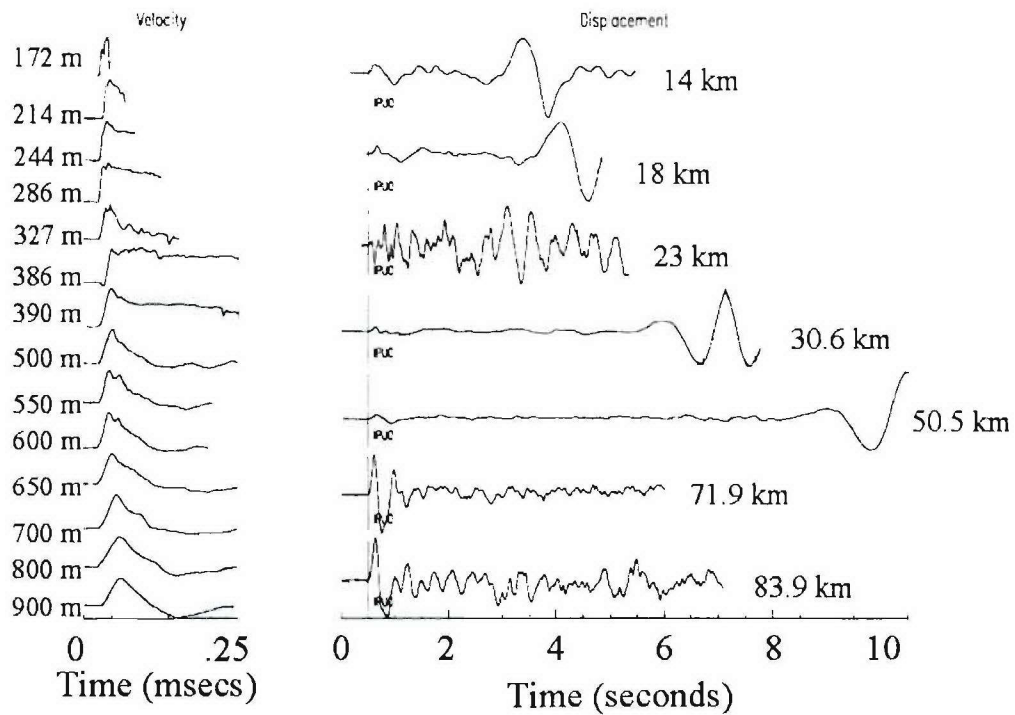


**Figure 4.** Near field (left) and near regional seismic (right) waveforms from the 1987/07/17 event.

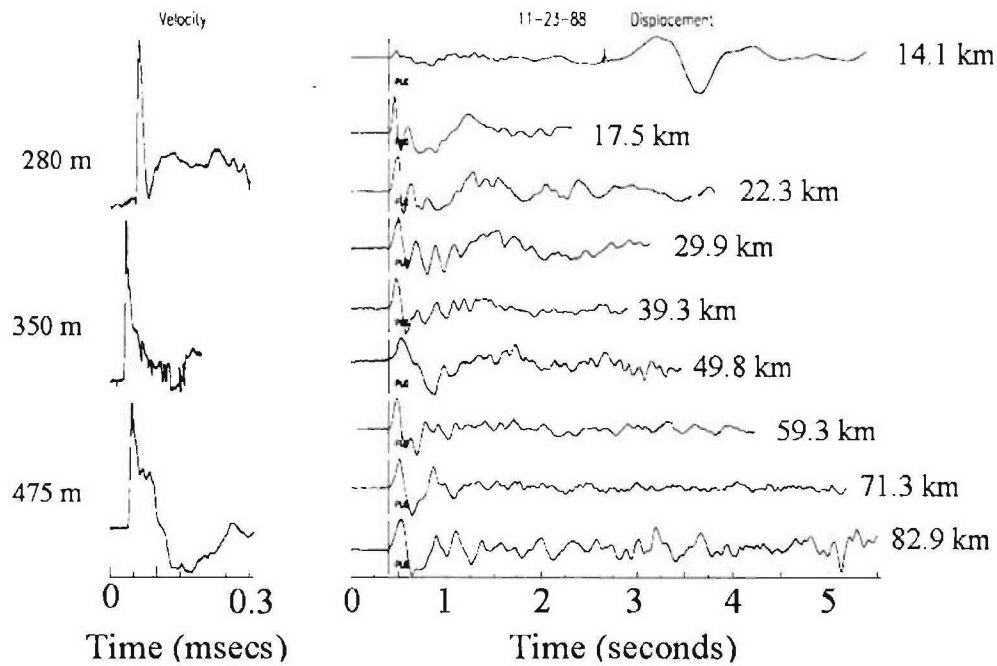


**Figure 5.** Near field (left) and near regional seismic (right) waveforms from the 1988/11/23 event.

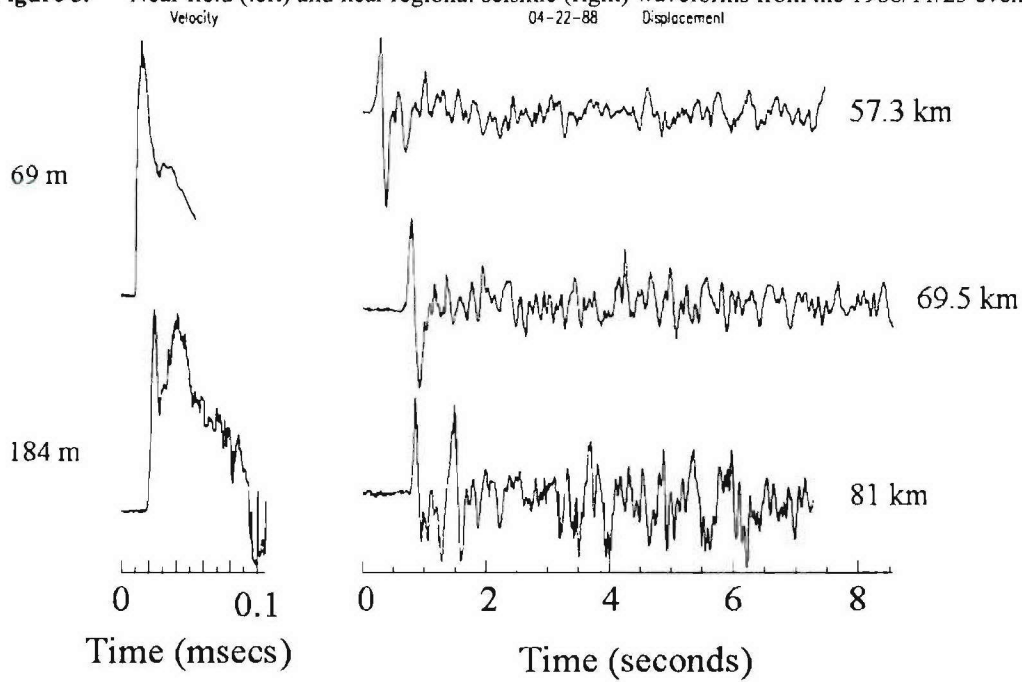


**Figure 6.** Near field (left) and near regional seismic (right) waveforms from the 1988/04/22 event.

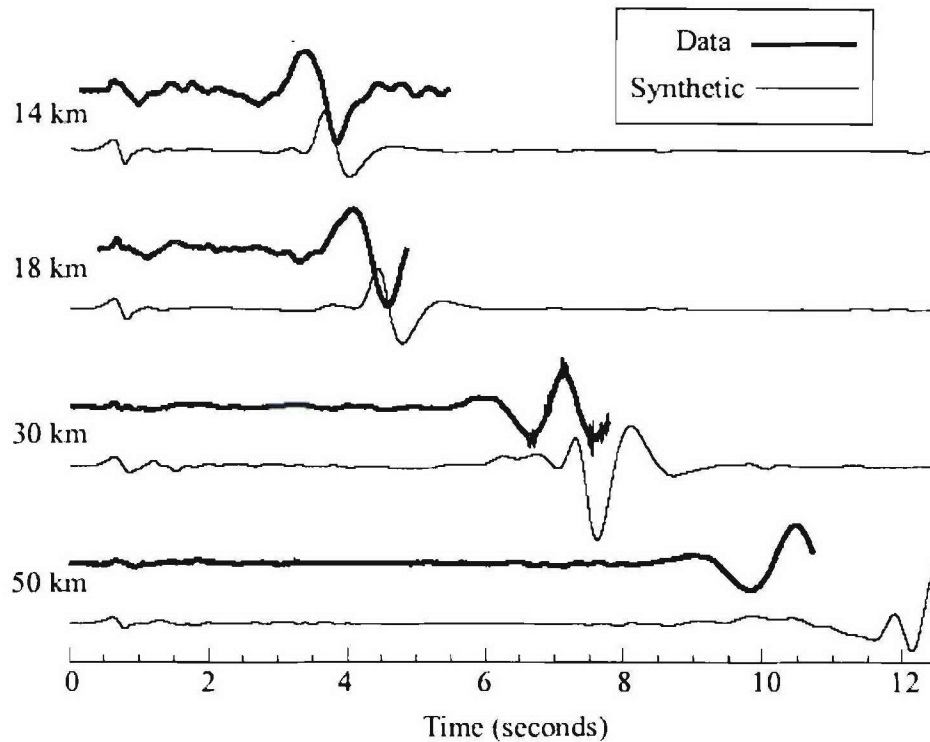


**Figure 7.** Synthetic and observed seismograms for the 1987/07/17 event. Synthetics were created using wavenumber integration and were low pass filtered at 2 Hz.

in Figures 1 and 2. The two gauges at larger ranges, that give relatively lower peak velocities, and most of the other gauges emplaced at depths above the explosion working point, were located on the opposite side of the source from the two closer-in gauges.

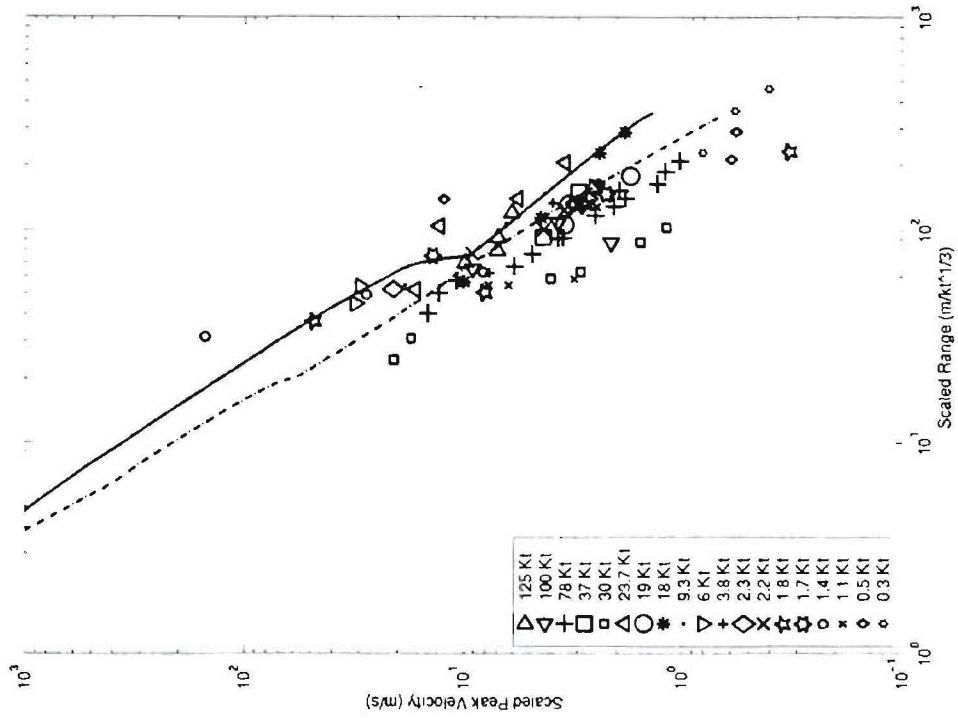
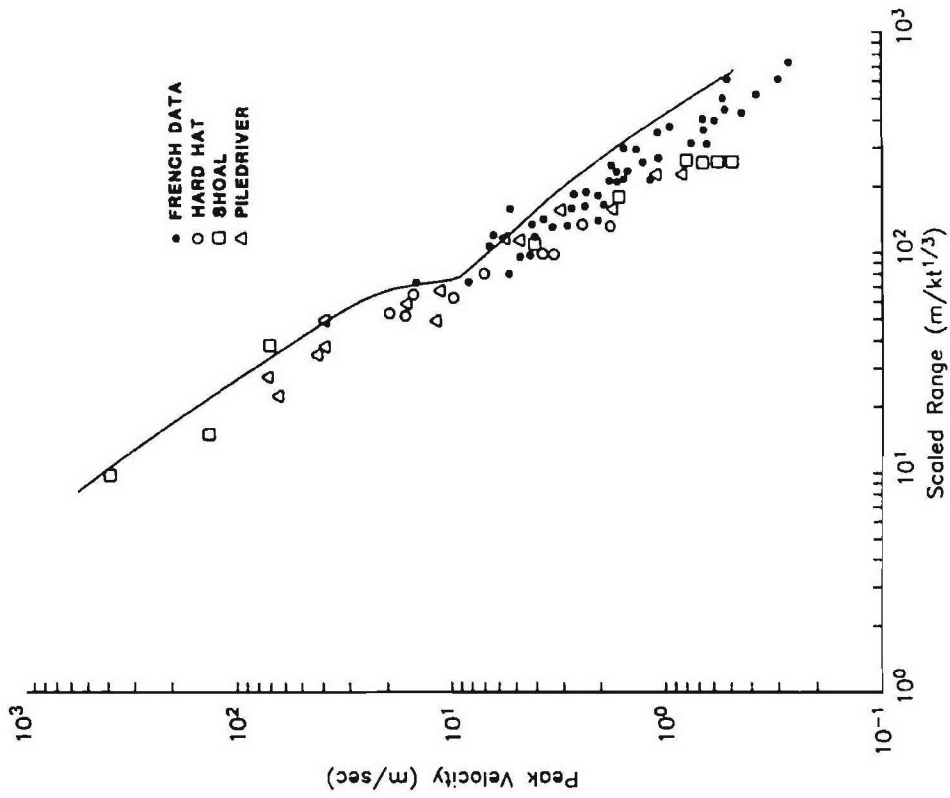
It should be noted that the very first sets of digitized data received from IDG (plotted in Rimer, et al, 1999, and Stevens, et al, 2001) did not include the Degelen explosions with relatively high peak velocities. Thus, these early Degelen peak velocities appeared at that time to be near the lower bound of the historic granite data. A Degelen simulation model, consisting of the Sammis failure model, followed by a large reduction in frictional strength for rubbleized rock elements, was developed to match the pulse widths from the first sets of digitized Degelen data. This model, labeled as DE12 in Rimer, et al (1999), is shown as a dashed curve in the right plots of Figure 8. It provides a better fit on average to all of the Degelen particle velocity and displacement peaks than does the higher pile570 simulation. However, this DE12 model, as will be shown below, is consistent with only a subset of the Degelen peak displacement data received more recently from IDG.

We have carefully analyzed the near-field particle velocity pulses from the first 19 Degelen explosions of Table 1 and excluded the data from five of these events as more characteristic of localized fault or block motions than of free-field ground motion. Pulse widths from four of the five events in general show very wide positive velocity pulses with almost constant outward velocity plateaus extending from some point after peak velocity to the end of the digitized data.

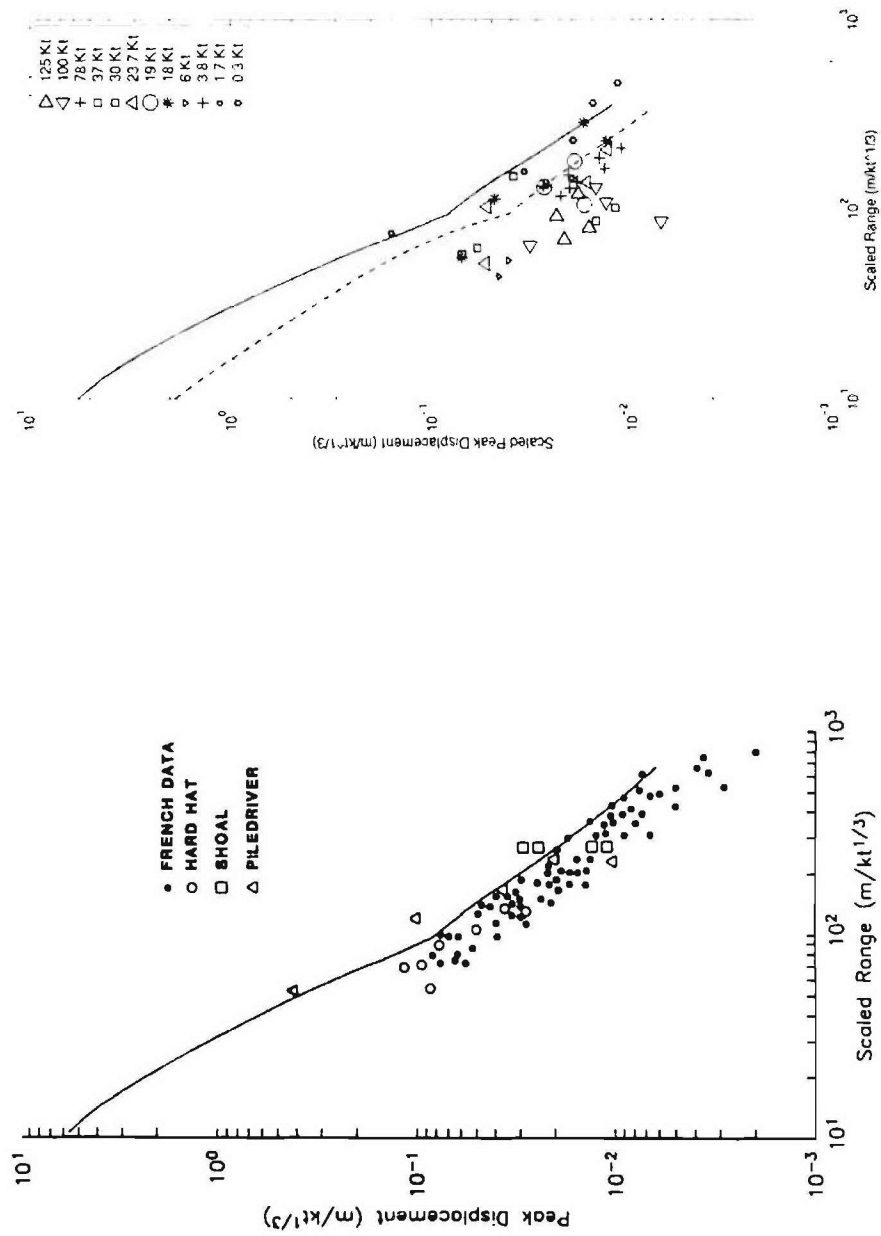


These excluded events have explosive yields of 1.1, 1.8, 1.4, and 2.2 kt. The fifth event, having a yield of 0.5 kt, has two records that look like the block motions from the first four excluded events, and two at larger scaled ranges with very large positive pulses that do have more of a free-field shape, but have almost no negative velocities. Another event, with explosive yield of 0.3 kt, is borderline, with reasonable pulse shapes obtained at scaled ranges larger than any of the other Degelen data. These records, however, have scaled positive and negative pulse widths much larger than the rest of the data. We have included this event in the free-field data set, but recognize that the positive pulse widths at the larger ranges from the excluded 0.5 kt event (but not the negative pulse widths) are quite similar to those from the included 0.3 kt event.

Figure 9 compares the peak particle velocity data for those 14 Degelen events having free-field pulse shapes (the left plot) with the full 19 event data set (the right plot), reproduced from Figure 8a. This “free-field set” of data includes the 10 explosions with yields greater than 5 kt and only 4 events with lower yields (3 kt or less). It is not surprising that a significant fraction of the data from the lower yield, and thus shorter wave length, explosions appear to be more contaminated by local block motion. This free-field set, apart from the data from the high velocity 23.7 kt explosion, and the very low velocity 30 kt explosion, shows considerably less scatter about the dashed DE12 prediction than did the full data set.



(a)



(b)

**Figure 8.**

(a) Peak particle velocity vs. scaled range for historic data from U.S. and French explosions (left) and for the 19 Degelen digitized explosions (right). The solid line is the prediction from the pile570 effective stress simulation shown earlier in Figure 2. The dashed line is the predicted peak velocity for the Degelen DE12 simulation using the Sammis failure model plus frictional strength reduction (Rimer, et al, 1999). (b) Peak displacement vs. scaled range for historic data from U.S. and French explosions (left) and for the 12 Degelen explosions that could be integrated to peak displacement (right). The solid line is the prediction from the pile570 effective stress simulation shown earlier in Figure 2. The dashed line is the predicted peak velocity for the Degelen DE12 simulation using the Sammis failure model plus frictional strength reduction (Rimer, et al, 1999).

To more easily compare the individual Degelen “free-field” particle velocity pulses from explosions of different yields, we have cube-root-of-yield-scaled these data to the PILEDRIVER yield of 62 kt. (All of our numerical simulations were performed at this explosive yield.) Figures 10-12 show 34 of these 56 individual (scaled to 62 kt) velocity pulses from 12 Degelen free-field events, together with the results at the same range, from the Degelen DE12 simulation. (The more recent simulations of different subsets of these data are shown in Section 4 of this report.)

It should be noted that data from the 6 and 37 kt free-field events (and the 2.2 kt event) of Table 1 were received after the modeling work was completed and waveform comparison plots were made, and so are not included in the waveform plots in this report. These data are included in Figures 8 and 9 where appropriate.

The quality of the particle velocity pulse data shown in Figures 10-12 vary greatly between explosions and even between records from the same explosion. In reducing the plotted “free-field” data from 56 particle velocity pulses to a somewhat more manageable best 34, we have chosen not to plot the following; (1) duplicate pulses, (2) the noisiest records such as three from the 9.3 kt event, (3) most of the early-time fragments of positive pulses measured at scaled to PILEDRIVER ranges of less than 280 m, (4) the more complete but extremely low amplitude closest-in records from the 30 kt explosion (these are self-consistent with the pulses that are shown for this event), (5) several inconsistent fragments of records and several complete records that are very consistent with those 7 data records from the 78 kt explosion that are plotted, and (6) single records having consistent pulse shapes but unusual amplitudes from the 23.7 kt (too high) and 100 kt explosions (too low).

The remaining 34 free-field records have been further subdivided into a subset of 24 records from 8 explosions that have relatively wide positive pulses (shown in Figures 10 and 11), and a smaller subset of 10 records from three explosions (having yields of 23.7, 100, and 125 kt) that have narrower positive pulses (shown in Figure 12). In each of these three figures, the records have been ordered by increasing scaled range from the (62 kt) explosion. Almost all of the free-field records not shown in Figures 10-12 are from the larger “wide pulse” subset. Each individual pulse in the three figures is identified by an event number, the explosive yield, and the (scaled to 62 kt) range. Since the original digitized data did not contain the actual explosion zero times (we now have arrival time data for some of these events), the data in each plot has been time-shifted to correspond roughly to the arrival times of the numerical simulation. In the following discussions, individual particle velocity records will always be referenced by their scaled to 62 kt ranges and original explosive yields. To compare with the peak velocity vs. scaled (to 1 kt) range data of Figures 8 and 9, simply divide the range (and the plotted times) given on each individual plot by a factor of 4.

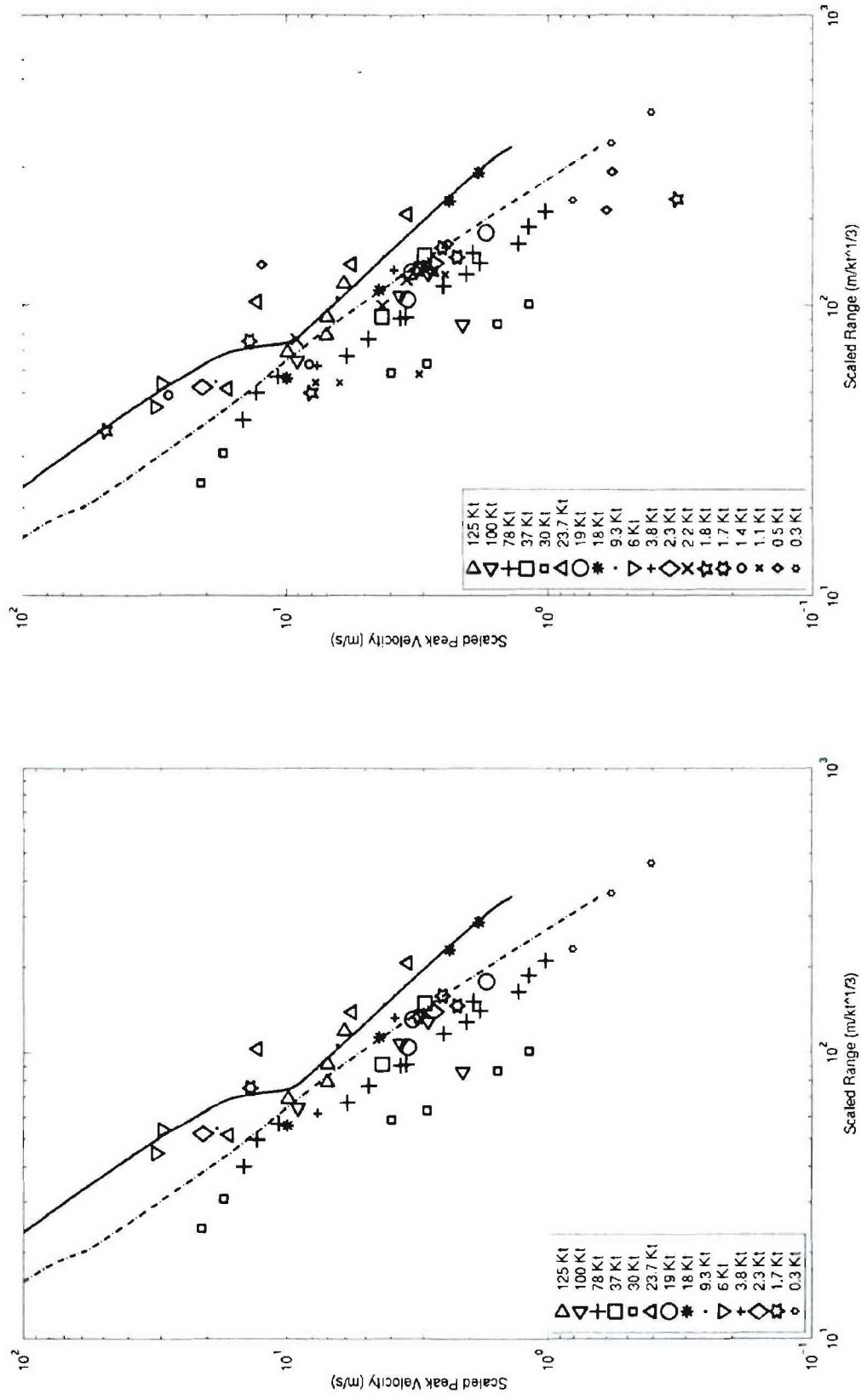


**Figure 9.** Peak particle velocity vs. scaled range for the 14 Degelen explosions designated as showing free-field pulse shapes (left), and for the full set of 19 Degelen explosions, as already shown in Figure 8a (right). The solid, pile570, and dashed, DE12, simulation results are shown as in Figure 8a.



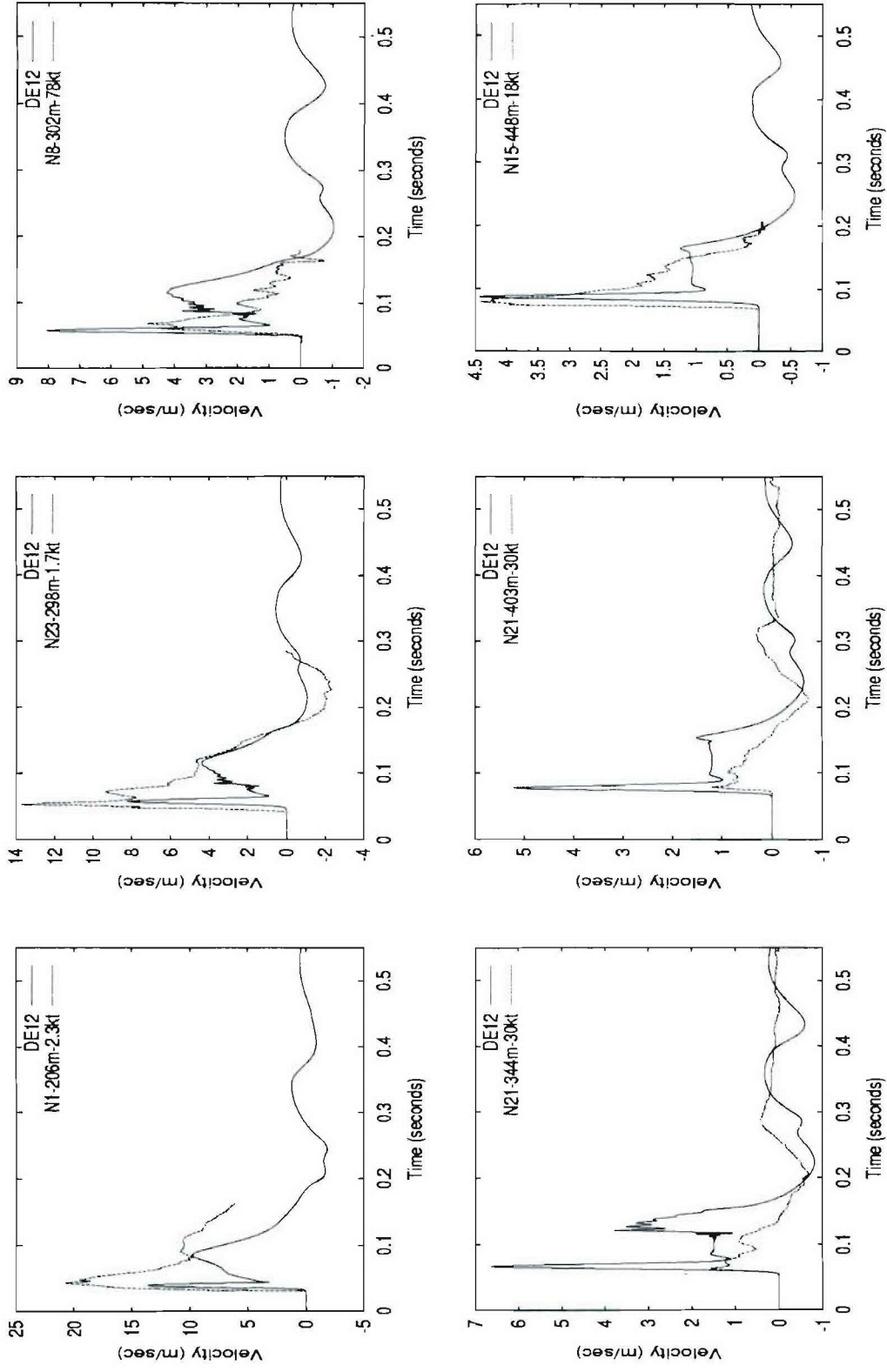


**Figure 10.** Particle velocity pulses at the smaller (scaled to PILEDRIVER) ranges from the “wide pulse” Degelen data subset compared with the results of simulation DE12 (solid curves).

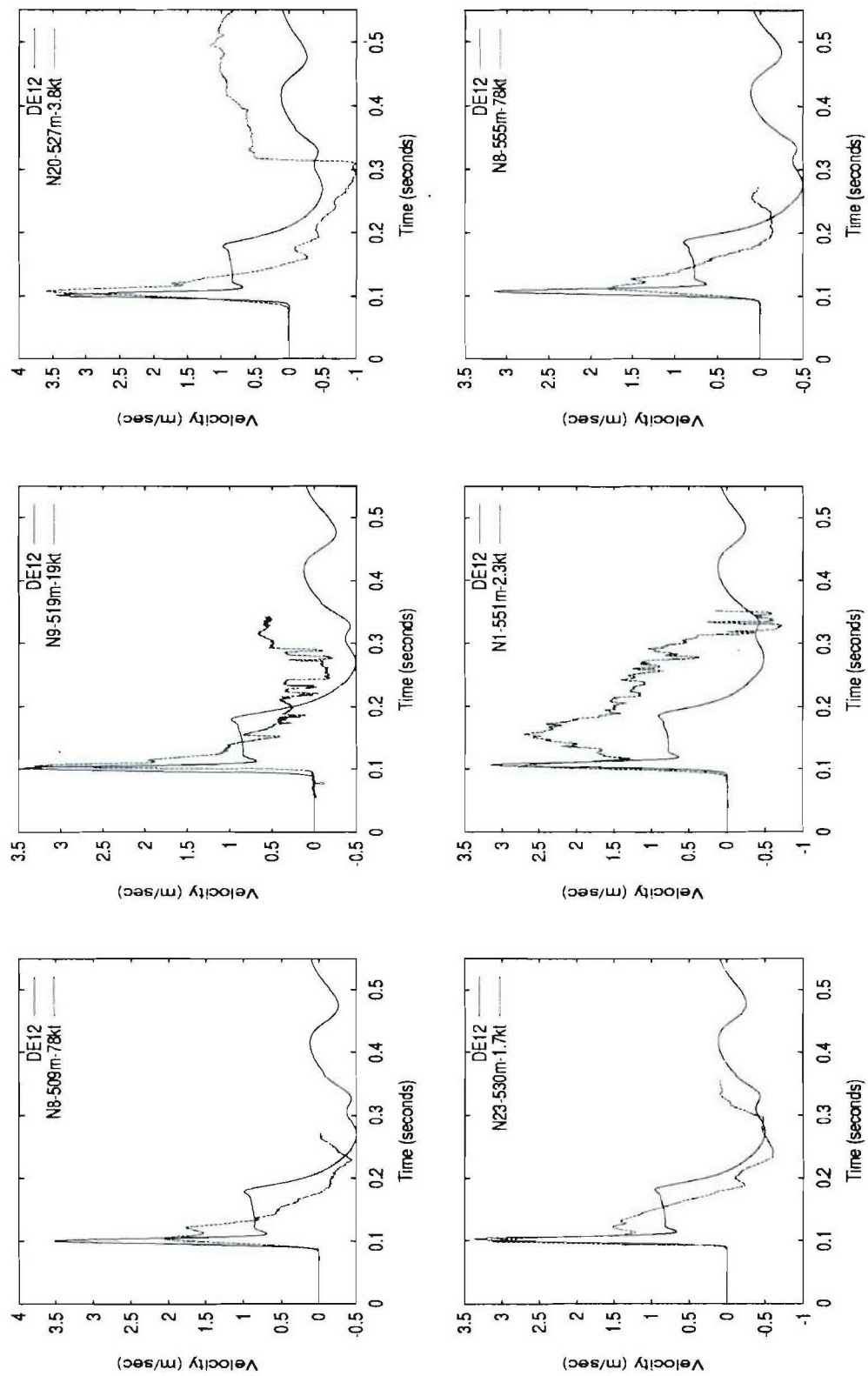
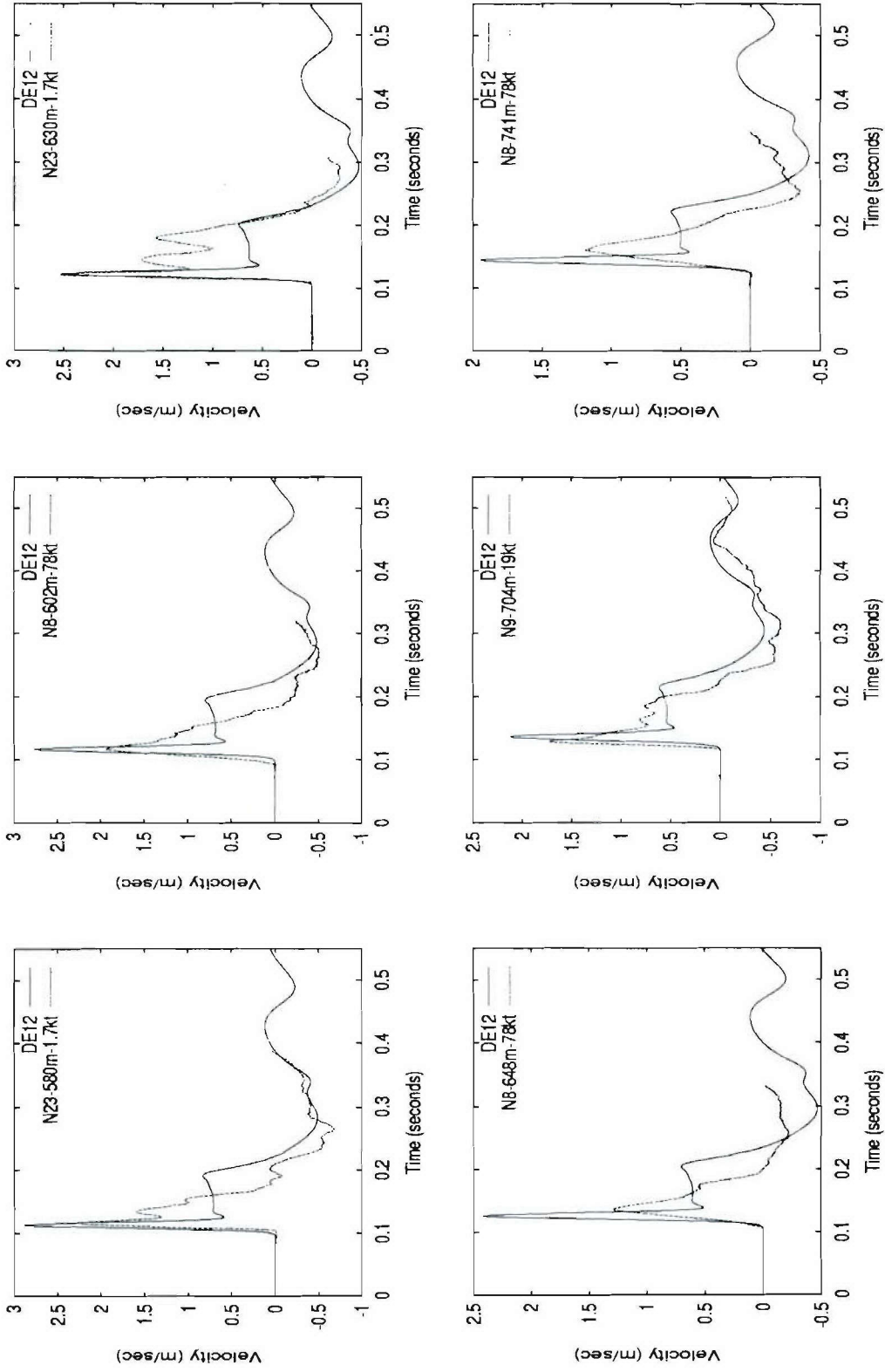


Figure 10. Continued.





**Figure 11.** Particle velocity pulses at the larger (scaled to PILEDRIVER) ranges from the “wide pulse” Degelen data subset compared with the results of simulation DE12 (solid curves).

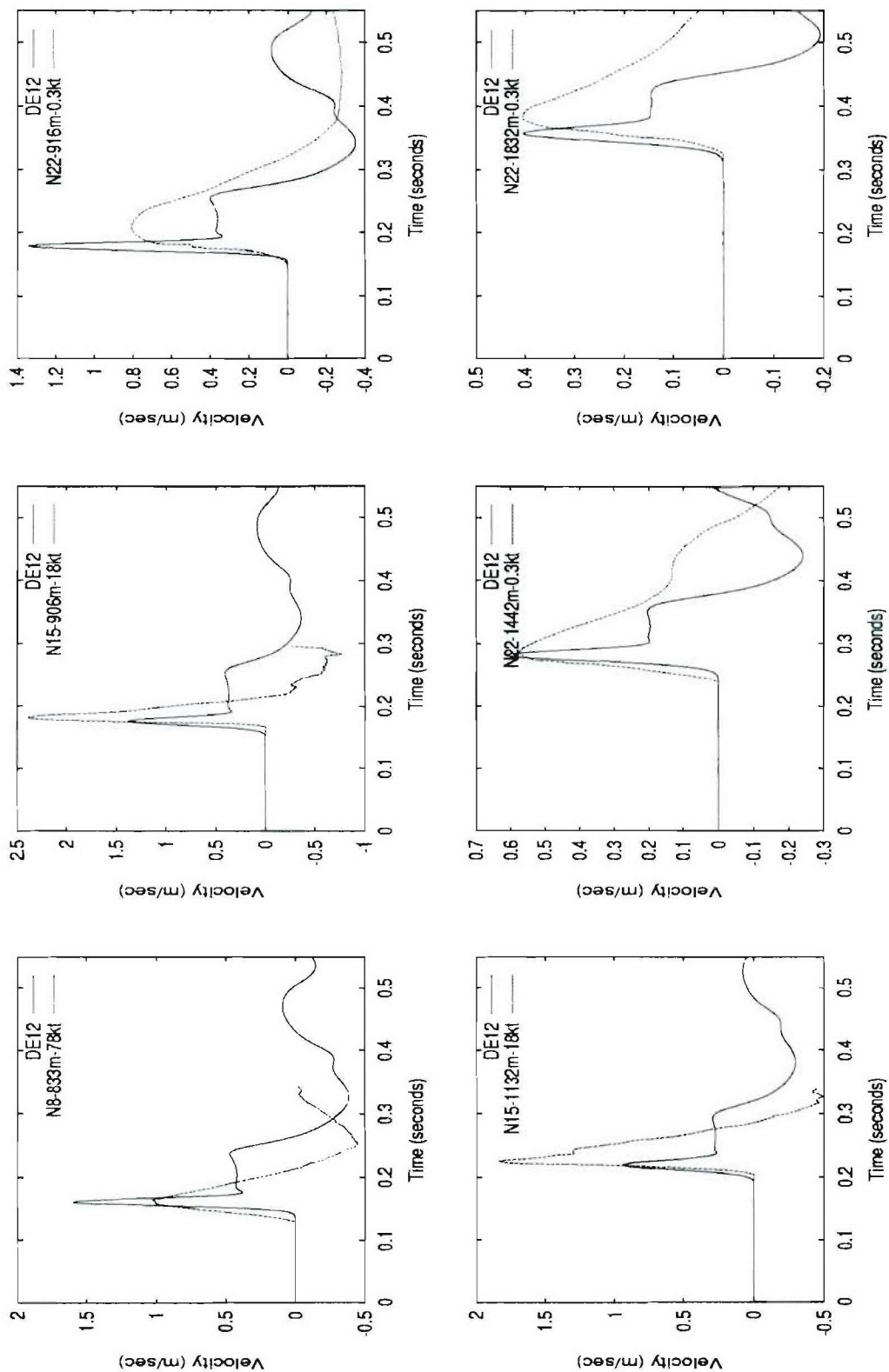
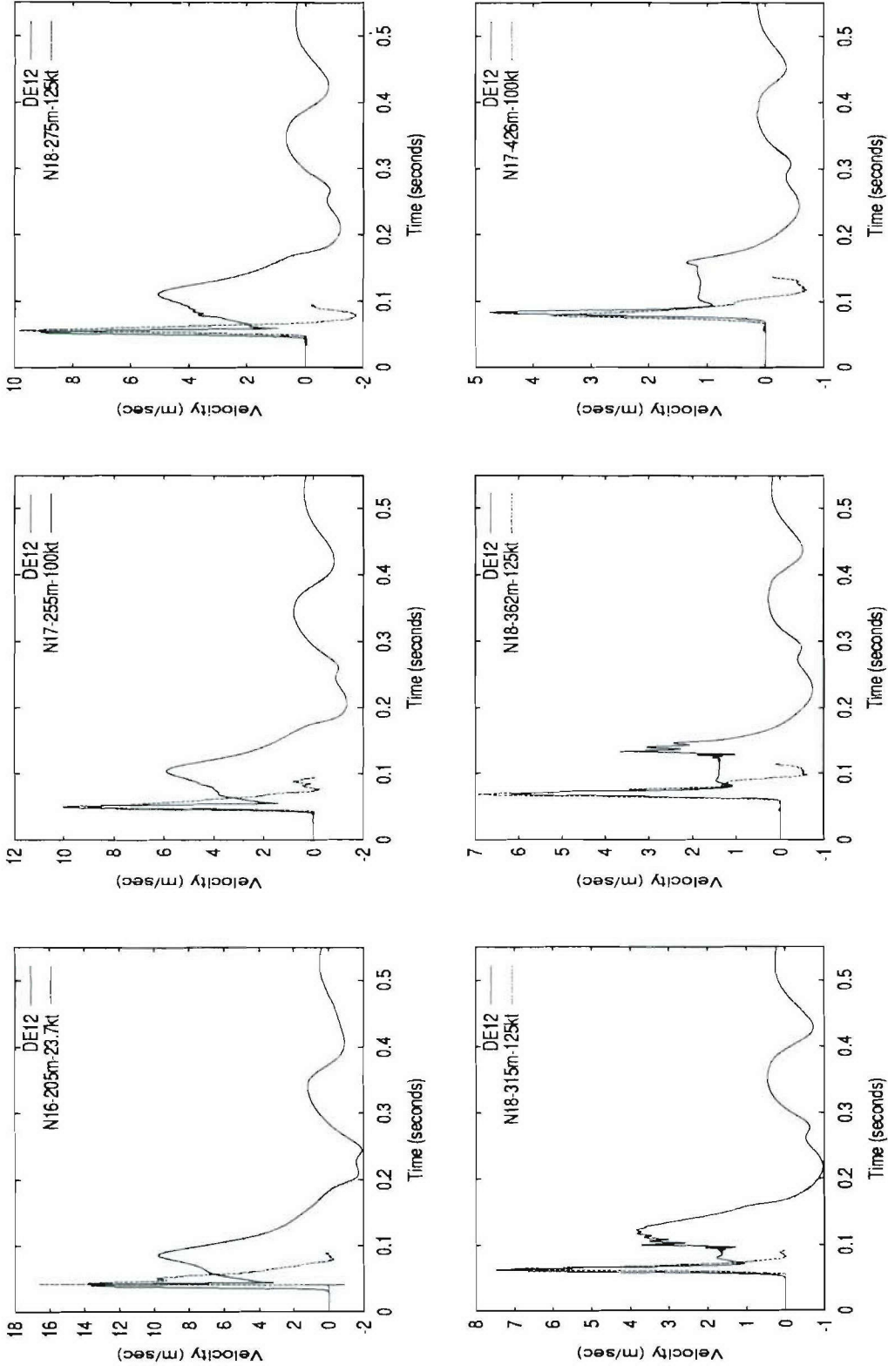
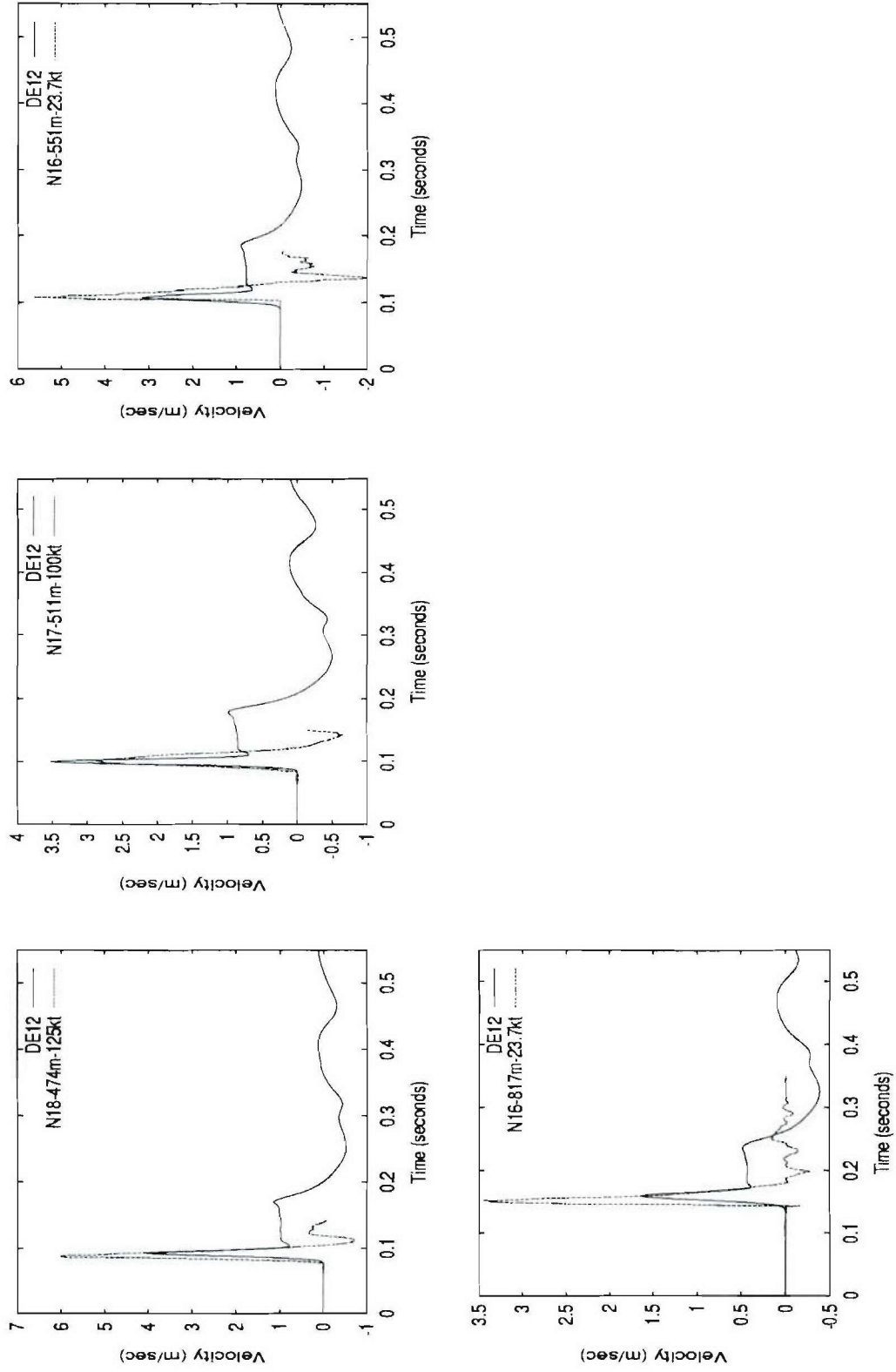


Figure 11. Continued.



**Figure 12.** Particle velocity pulses at (scaled to PILEDRIVER) ranges from the “narrow pulse” Degelen data subset compared with the results of simulation DE12 (solid curves).



**Figure 12.** Continued.

The DE12 model (Rimer, et al, 1999) was designed to simulate the pulse widths from the digitized Degelen data available at that time. These included only the records from the first two explosions listed in Table 1 (2.3 and 19 kt) as well as a few of the records from the third (78 kt) explosion. All three of these free-field explosions were later categorized as belonging to the wide pulse subset. This simulation was also required to provide a cavity radius and a Reduced Displacement Potential (RDP) consistent with more general observations from the Degelen site. Agreement between simulated and measured positive and negative pulses was best at the 704 m range from the 19 kt explosion, but the measured positive pulse at the 741 m range (and other ranges) from the 78 kt explosion are somewhat narrower than those simulated. Only two partial records are available from the 2.3 kt explosion, with one of these, at 551 m, considerably wider than other explosion records at similar scaled ranges.

As more digitized data were received from the 78 kt event, and still later from the other events of the data set, it became clear that there is a significant gradation of pulse widths within even the wide pulse subset. Moreover, some of these data exhibit a second positive pulse with either a second obvious peak or traces of a plateau similar to both the DE12 simulation and the data at 704 m from the 19 kt explosion, while others show no evidence of such a second pulse. As an example, for the 1.7 kt event, all four of the records shown in Figures 10 and 11 appear to give qualitatively consistent shapes that include such a second pulse. The gauges from the closest-in and furthest-out of the four ranges, located near the emplacement tunnel, give positive pulse widths in good agreement with DE12, while the middle two gauges, at substantially different azimuths from the others, give narrower pulses. In contrast to these data from the 1.7 kt event, most of the records from the 78 kt and 18 kt explosions exhibit either no second pulse or only a little suggestion of such a pulse.

It is of course possible that some or all of the recorded second pulses are either the result of some systematic errors in gauge response or perhaps indications of some non-free-field response of the rock at these sites. In the absence of convincing evidence, we are choosing to treat these records as free-field. This leads to the hypotheses that the material models required to simulate the records from even just the wide pulse subset, or more likely the material constants within any one particular set of material models, may be different for each explosion site.

The particle velocity records from the three “narrow pulse” explosions shown in Figure 12 give somewhat different peak amplitudes, but very similar positive pulse shapes. In general, these records do not exhibit the two pulse structure apparent in much of the wide pulse subset. The majority of these plots also show narrow negative pulses, although at least one record from each of the three explosions does not show such a negative.

With one exception, every positive pulse shown from the 8 explosions in Figures 10 and 11 is much wider than any of the pulses from the three explosion “narrow pulse” subset shown in Figure 12. This exception is the 18 kt explosion that does not fit very well in either the wide or narrow subsets. The 18 kt explosion has one wide pulse, at the smaller range of 448 m in Figure 10, one narrow pulse, at the middle range of 906 m in Figure 11, and a pulse slightly narrower than the wide pulse subset at the larger range of 1132 m. We have chosen to place this explosion in the wide subset because the narrow pulse explosions of Figure 12 also tend to show very



narrow negative pulses, while the most complete negative pulse record from the 18 kt event, at 906 m, is wider than those of Figure 12.

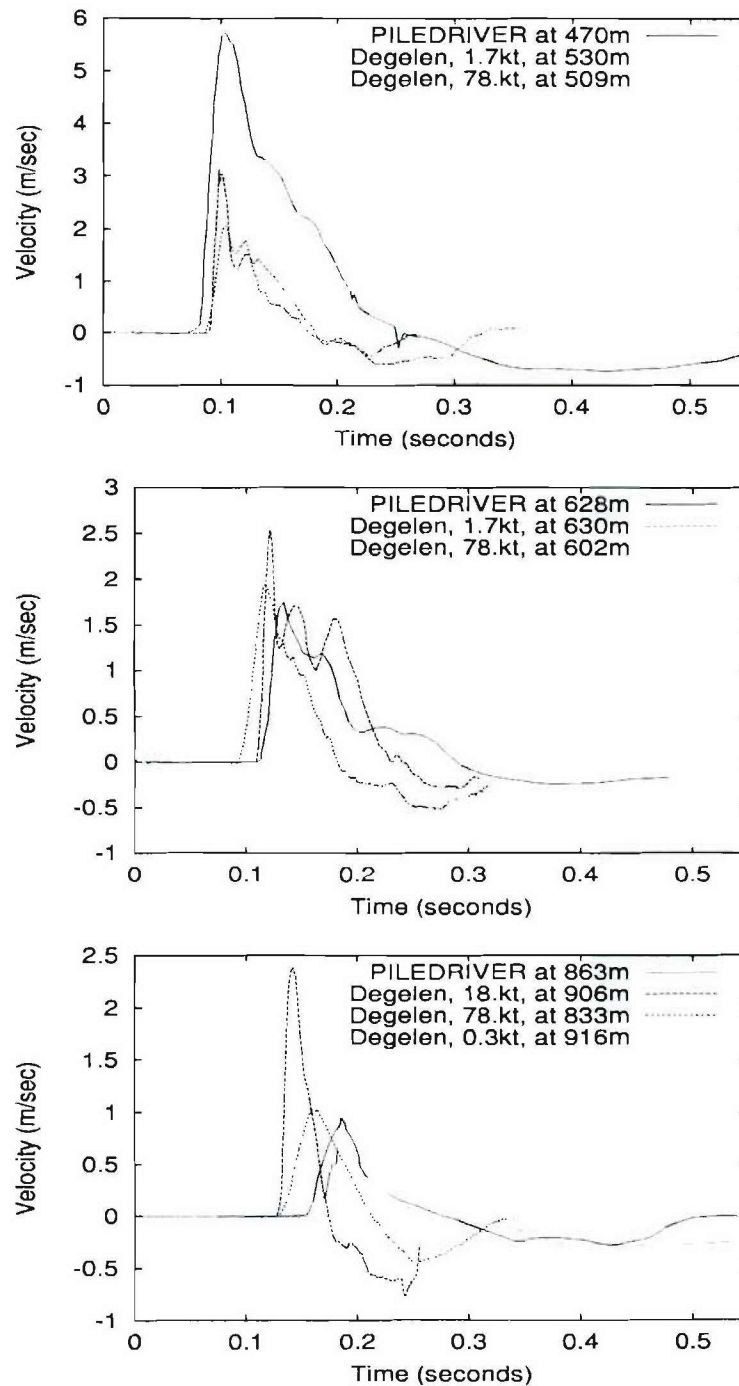
The two very low amplitude records from the 30 kt explosion that are shown in Figure 10 (and those at smaller ranges that are not shown) have pulse shapes and pulse widths similar to others of the wide pulse subset. In the absence of specific site material properties for this and other explosion sites, we have no satisfactory explanation for the unusual low peak amplitudes from the 30 kt explosion. Depth of burial for this explosion is consistent with those for the other large explosions of Table 1 that were at sites described as in granite. Only the narrow pulse 100 and 125 kt explosions, at sites described as in quartz porphyry, and the 37 kt wide pulse event were more deeply buried. The  $m_b$  values given in Table 1 also do not provide any confirmation of the unusually low near-field particle velocity amplitudes from the 30 kt explosion.

Figure 13 shows comparisons between particle velocity records at the three largest of the four ranges shown earlier from PILEDRIIVER (the solid curves) and some of the records from similar scaled ranges from wide pulse Degelen explosions scaled to 62 kt. Since representative, relatively complete records from the wide pulse Degelen explosions are not available at scaled ranges approximating the 207 m range of the first (and widest) PILEDRIIVER particle velocity record, comparisons at the 207 m range are not shown in Figure 13. Near the 470 m range, the PILEDRIIVER positive and negative pulses are clearly much wider than those from Degelen explosions, although the general shapes of the PILEDRIIVER and Degelen positive pulses are quite similar.

Differences between the records from the U.S. and Degelen granite sites are less obvious at the two larger ranges. We have seen earlier that the peak amplitudes from PILEDRIIVER are small at these two ranges relative to those that would be predicted from the two closer-in records. At 628 m, the PILEDRIIVER record looks very similar to the record from the 78 kt explosion out to a time of roughly 0.2 seconds (especially if the arrival time of the 78 kt record is time-shifted to coincide with the PILEDRIIVER arrival time). Near 0.2 seconds, the PILEDRIIVER positive pulse at 628 m begins to stretch out in time, with a clear almost constant velocity plateau visible on this record, giving a much later time zero crossing and a wider negative pulse than both the Degelen records. At this range, the record from the 1.7 kt explosion shows a steeper rise to peak, multiple peaks, and a significantly wider positive pulse than the PILEDRIIVER record, at least until that record begins to stretch out in time. The PILEDRIIVER record at 863 m also shows such a stretching, but not the constant velocity plateau recorded at 628 m. Once again, the record from the 78 kt explosion, when time shifted, is in good agreement with it until this stretching begins. At both ranges, the 78 kt negative pulses show larger peaks but smaller widths than the PILEDRIIVER records.

The particle velocity comparisons made near the 863 m range illustrate the large gradation in pulse shapes and pulse widths recorded from Degelen "wide pulse" explosions, with the 18 kt record showing a much steeper rise, a much higher peak, a narrower pulse, than the 78 kt record, but a similar negative peak. These are contrasted with the narrowest of the three very wide pulses obtained from the scaled 0.3 kt explosion. This pulse is wider than the PILEDRIIVER record at a slightly smaller scaled range. When these particle velocity records are time-integrated, only the PILEDRIIVER records at the two closest-in ranges (207 and 470 m) give peak displacements significantly larger than all of the Degelen records at comparable scaled

ranges. Peak displacement from the 1.7 kt explosion is similar in magnitude to that from PILEDRIIVER near 628 m, while peak displacement from the 0.3 kt explosion is larger than from PILEDRIIVER near 863 m.



**Figure 13.** Comparisons between particle velocity pulses at three ranges from PILEDRIIVER and Degelen “wide pulse” explosion records (scaled to 62 kt) at nearby scaled ranges.



## 2.1 Degelen RDP Comparisons

Before attempting to correlate the near-field particle velocity data with data from the same explosions at near regional seismic distances, we first will compare the RDPs computed from some of the Degelen records that have been already shown in Figures 10-12 with those obtained both from the data from U. S. explosions in granite (see Murphy, 1977 and 1978) and from the pile570 and DE12 simulations. As before, all comparisons are made for records scaled to the 62 kt PILEDRIVER yield. Murphy (1978) has shown that the RDPs computed from the closer-in PILEDRIVER gauges are considerably larger than those from gauges located at larger scaled ranges. Our PILEDRIVER simulations indicate that the two closer-in records are at ranges well within the elastic radius. We will limit our comparisons here to Degelen records from near or beyond the presumed (based on earlier granite simulations) granite elastic radius of about 600 m for 62 kt. (We have relaxed this range restriction for some of the “narrow pulse” Degelen data since these indicate elastic behavior at somewhat smaller scaled ranges.)

In general, the comparisons that follow will also be limited to the peak values of the RDP obtained from the Degelen data, rather than to the final or static RDP. The RDPs computed by Murphy (1978) from PILEDRIVER and other U. S. granite events indicate that particle velocity records at multiple stations from an explosion rarely give similar static values of the RDP even when the records exist to sufficiently late times that the remaining motions should become negligible. (Baseline correction problems during the time integration of accelerometer records are a well-known source of late-time errors in particle velocity records.) Also, most of the digitized Degelen particle velocity data shown in Figures 10-12 terminate at scaled times of 0.3-0.4 seconds (or earlier), well before the ground motions have ended.

Figure 14 shows the particle velocity record at 704 m from the 19 kt explosion (one of the more complete records available) and the RDP obtained from it, together with results of the DE12 simulation. The RDPs obtained from the simulation and from the data both show well-defined, and in this example similar, peak values, but differ considerably at later times, even though the differences between the two particle velocity records appear small. The static value of the RDP of course would be directly proportional to the final displacement, i.e., the difference between the areas under the complete positive and negative particle velocity pulses. Computation of the RDP, in general, involves convolving the particle velocity with an exponential function, thus giving increasing weight to later time (negative pulse) data. In the example illustrated in Figure 14, the area under the negative pulse in the data record is clearly greater than that from the DE12 simulation, resulting in smaller later-time displacements and RDP.

Table 2 gives values of peak RDP (scaled to 62 kt) computed from Degelen particle velocity records from both the “wide pulse” subset and the “narrow pulse” subset. Almost all (15 of 17) of the wide pulse records that we integrated gave RDP versus time plots that look qualitatively similar to those shown in Figure 14, with a rise to a peak RDP value, followed by decreasing RDP. However, all four of the narrow pulse records but only two of the wide pulse records, with

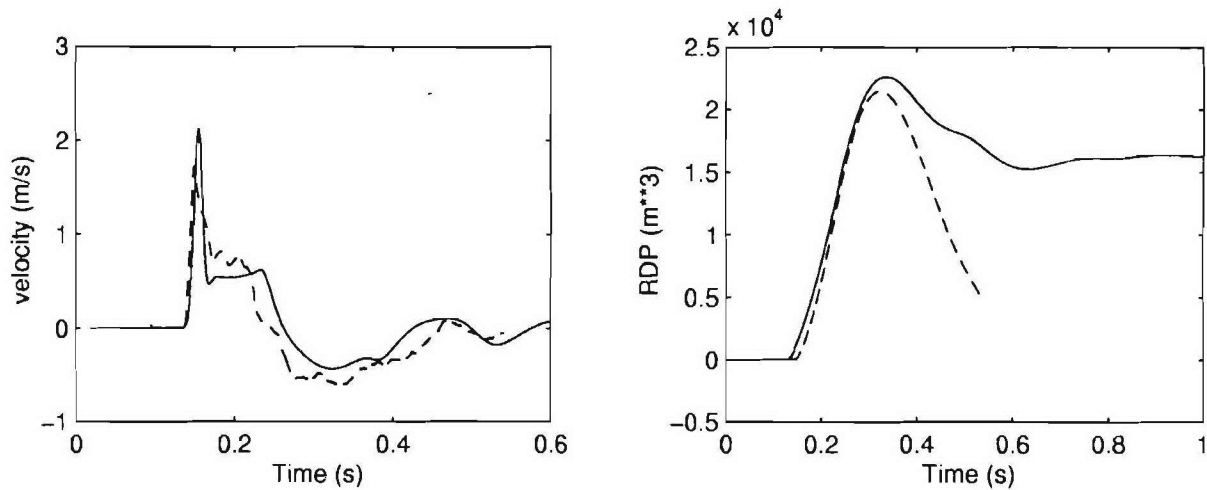


**Figure 14.** Scaled-to-62 kt particle velocity records (left) and computed RDPs (right) from simulation DE12 (solid curves) and from the scaled-to-62 kt range of 704 m from the 19 kt Degelen explosion (dashed curves).

relatively small negative particle velocity pulse widths, gave RDPs that are still increasing with time at the end of the records. This RDP shape, equivalent to a Reduced Velocity Potential (RVP) that is positive throughout the time interval of the record, may be indicative of strong dilatant behavior of the rock at a few of the explosion sites.

**Table 2.** Peak RDPs (scaled to 62 kt) computed from the Degelen particle velocity data and computed from the empirical Mueller-Murphy (MM) source for 62 kt nuclear explosions at granite sites.

Explosion Yield (kt)	Depth of Burial (m)	Peak RDP from data ( $10^3 \text{ m}^3$ )	Peak RDP from MM ( $10^3 \text{ m}^3$ )
<b>Wide pulse subset:</b>			
0.3	152	40, 75, 83, increases with range	37.8
1.7	112	17, 37*	41.3
18	262	15, 30*	32.2
19	204	23	34.6
30	260	5, 5	32.3
78	267	13-18, from 7 records	32.0
<b>Narrow pulse subset:</b>			
23.7	262	7*, 24*	32.2
100	320	5*	30.4
125	343	6*	29.8

\*denotes that RDP is still increasing at end of record.



The wide and narrow pulse subsets have been ordered in Table 2 from smallest to largest explosive yields. If all of the explosion sites were identical, and the depths of burial were the same, one would expect that the computed peak RDPs, after scaling to 62 kt, would all be very similar. In fact, the larger scaled peak RDPs were obtained from the widest pulses that were from the smallest explosions, but the smallest RDPs were obtained from the largest yield, narrow pulse, explosions (and also from the unusually low amplitude 30 kt explosion). Possible explanations may include the different depths of burial (these are also given in Table 2), different site characteristics or material properties, and/or material behavior that does not yield scale. The variation in RDP results clearly does not correlate all that well with depths of burial, since the 18, 23.7, 30, and 78 kt explosion sources all have similar burial depths. However, the larger RDP 0.3 and 1.7 kt explosions are among the most shallowly buried of the explosions listed in Table 2 and the smaller RDP 100 and 125 kt events are the most deeply buried. It is more likely that these differences in depths of burial may correspond to more significant differences in site material properties and other site characteristics such as fault frequency, apertures, etc. If the fault characteristics are the dominant effects, then yield scaling itself may be suspect.

The empirical Mueller-Murphy (MM) source for nuclear explosions at granite sites, as given in Murphy (1977), implies a peak RDP of roughly 25 (in units of  $10^{+3}$  cubic meters) and a static RDP of about 16 for PILEDRIVER explosive yield and depth of burial, in good agreement with the DE12 simulation shown in Figure 14. However, the DE12 simulation was made for a DOB of about 200 m. The relatively small depth dependence in the empirical MM source is given in Table 2 for the Degelen explosions. The MM source implies a roughly 25-30% increase in peak RDP from the PILEDRIVER depth of burial to the depth shown for the 19 kt source. It should be noted however that the MM source, which accurately predicts the  $m_b$  values for PILEDRIVER, HARDHAT, and SHOAL, is also less peaked than the RDPs computed from particle velocity records from these U. S. explosions. The pile570 simulation, in better agreement with the closer-in PILEDRIVER stations, gives a static RDP of 16.6, similar to the MM source, but a much higher peak RDP of 55, more in agreement with the peak RDPs obtained from the 0.3 kt explosion. Neither of these two simulations nor the MM empirical source predict some of the lower peak RDP values given in Table 2.

IDG has provided arrival time data (shown in Table 3 and Figure 15) at the near-field gauges for some of the explosions of Table 1. In Figure 15, these arrival times have been plotted for each gauge vs. distance to the gauge location from the explosion point. With only a few exceptions, these data are quite consistent with a global P-wave velocity of 5.0-5.6 km/s. (Our Degelen simulations have used a speed of 5.175 km/s.) A least squares technique was used to determine wave speeds from the arrival data for each individual explosion. Table 3 shows the resulting wave speed for each of the events for which we have received arrival time data. When the wave speeds from Table 3 were used, instead of 5.175 km/s, to compute peak RDP's, only small changes in the results of Table 2 were calculated.

**Table 3.** P-wave velocities computed from arrival time data.

Event	Yield, kt	Wave speed (km/s)	Pulse width subset
1980/06/25	0.3	4.58	Wide
1984/10/18	1.4	3.83	Not free field
1982/12/25	1.7	5.00	Wide
1988/04/22	2.3	4.66	Wide
1981/07/17	9.3	5.24	Wide
1965/02/04	18	5.5	Wide
1964/05/16	23.7	5.55	Narrow
1987/07/17	78	5.32	Wide
1966/03/20	100	5.3	Narrow
1966/02/13	125	5.8	Narrow

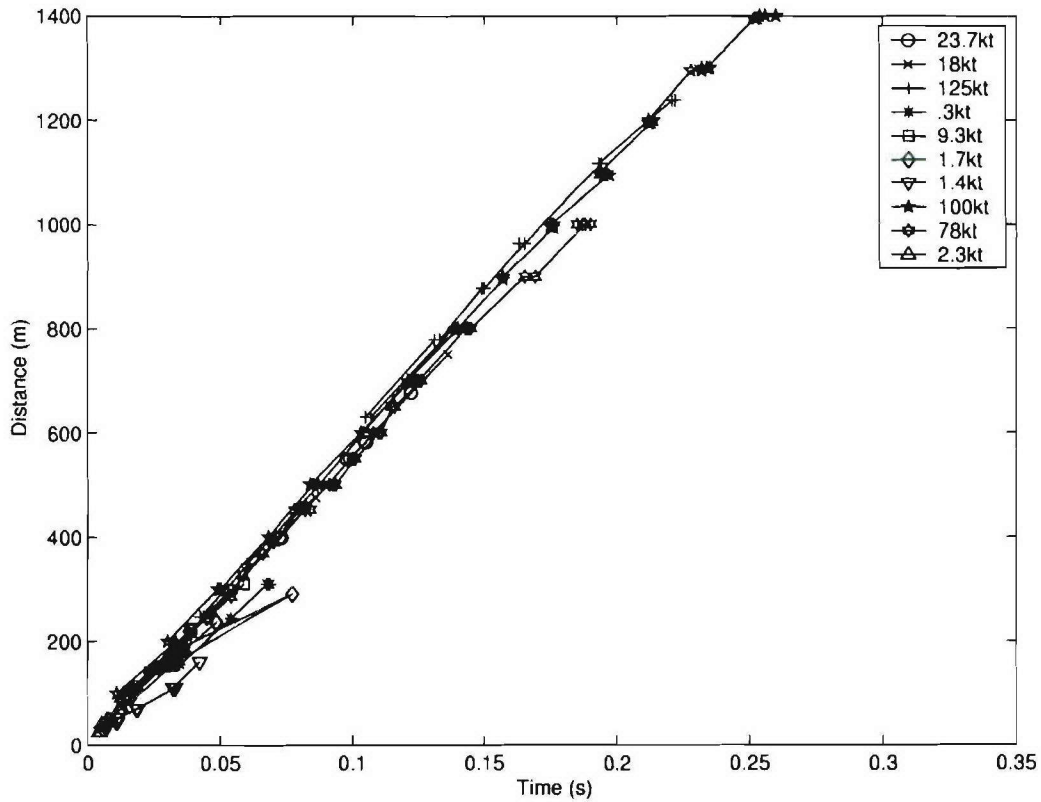
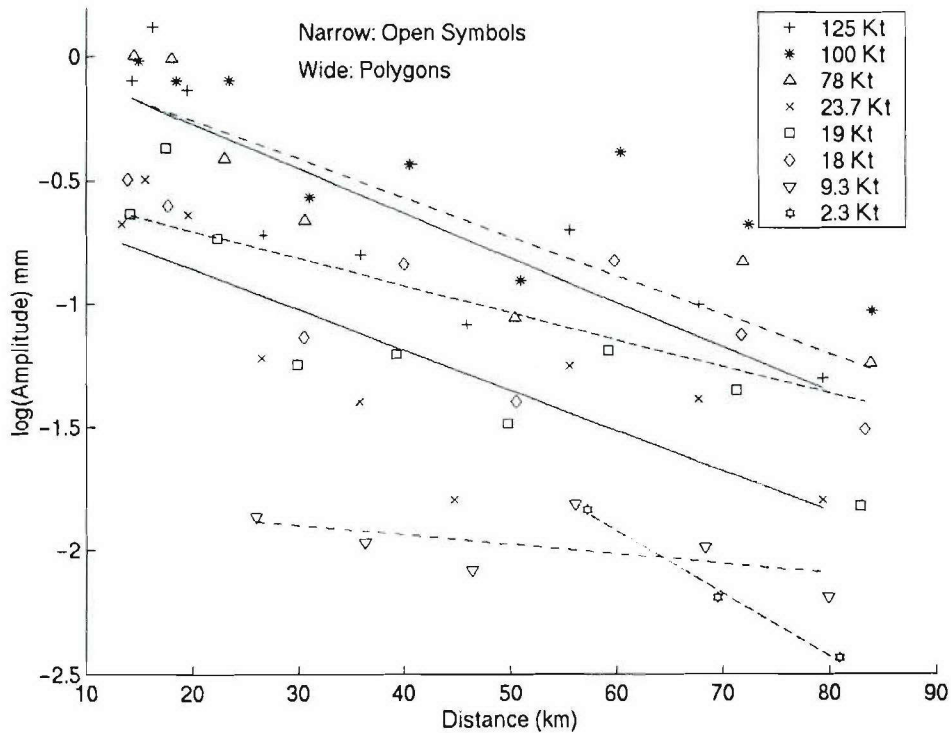


**Figure 15.** Arrival times at near-field gauge locations.

## 2.2 Near Regional Data Analysis

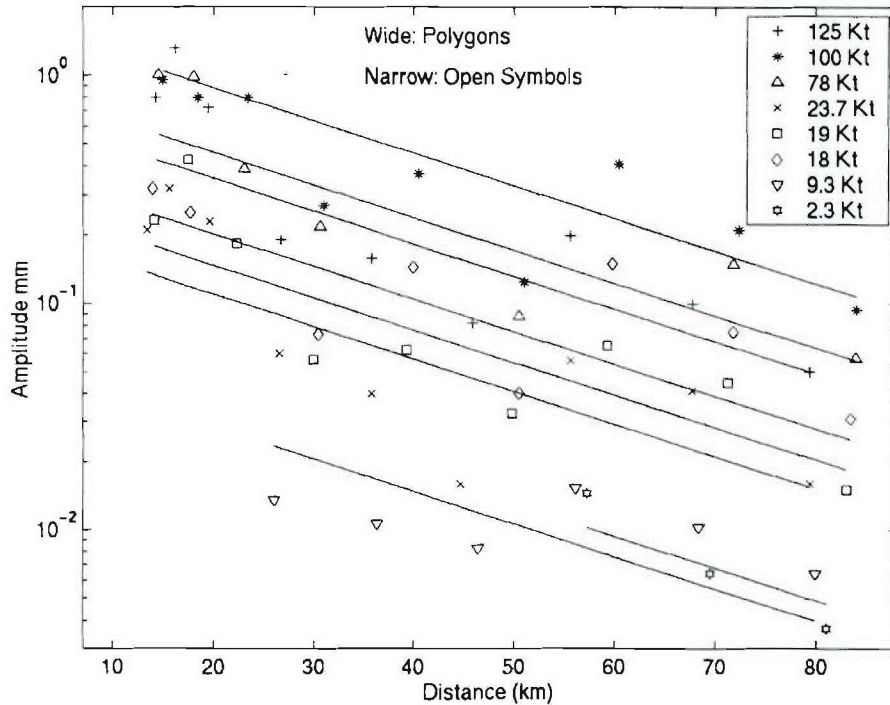
We next examine the digitized near regional seismic records. The 8 explosions to be studied include all 3 of the narrow pulse subset, and 3 of the 6 wide pulse explosions for which we have computed RDPs (we do not have digitized seismic data from the 30, 1.7, and 0.3 kt events of Table 2). The wide pulse 2.3 and 9.3 kt explosions, for which the near-field data look “free-field” but do not last long in time enough to compute representative RDPs, are also included. The primary purpose of this analysis of the 8 largest Degelen explosions for which we have digitized seismic data is to determine whether or not the differences in pulse widths and RDP observed for the near-field data are observable at larger, seismic ranges. Based on the near-field observations described in this report, we would expect the seismograms at larger ranges from the “narrow pulse” subset of explosions to have relatively smaller amplitudes.

We first empirically determine a distance correction for the 8 explosions (see Figure 16). We determine a slope of  $\log(\text{Amplitude})$  vs. distance for each event, and then find the average of the slopes, weighted by the number of points contributing to each curve. The distance correction is approximately  $-0.014$  of  $\log(\text{amplitude})$  in mm per km. Figure 17 shows the best fit line to each event’s vertical P wave displacements, using the average slope. The separation between curves reflects the dependence of amplitude on yield.



**Figure 16.** Log of the P wave amplitude vs. distance for five events with wide velocity pulses in the near field (polygonal symbols) and three events with narrow velocity pulses in the near field (+, x, and \*). Most regression curves have a similar slope, and we use the average, weighted by the number of points in each event, to correct all records back to 10 km distance from the source.





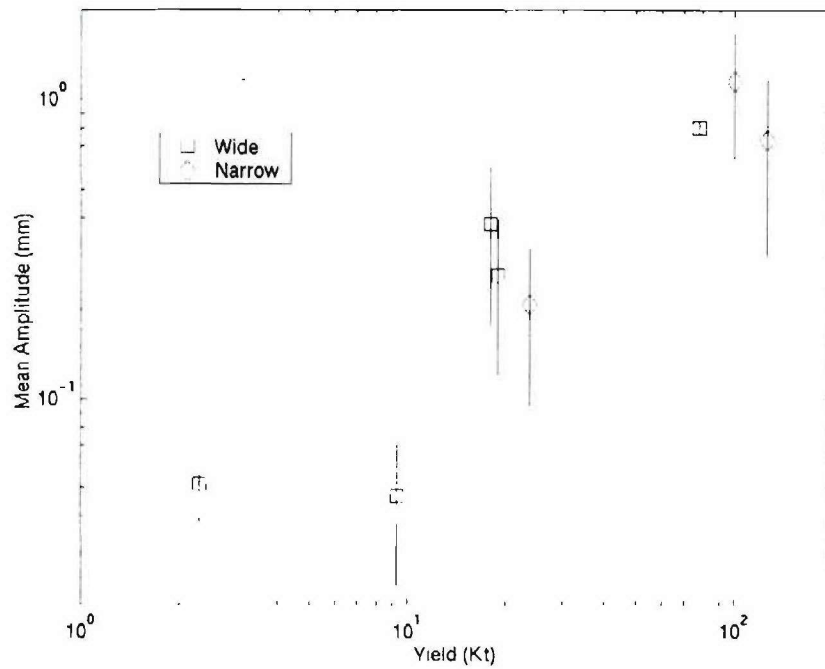
**Figure 17.** The same data as in Figure 16, with the best fit lines for the average distance correction. The separation between lines reflects the dependence of amplitude on yield.

Figure 18 shows the log amplitude of each vertical P wave displacement, corrected to 10 km distance, vs. log yield. Assuming  $\log_{10}(\text{amplitude}) = B \cdot \log_{10}(\text{yield}) + C$ , these data are used to estimate a B of 0.76 and a C of -1.76. These values do not change significantly if we determine them separately from the narrow and wide pulse data subsets. From just the wide pulse data we obtain  $B=0.83$  and  $C=-1.8$ , and from the narrow pulse data we obtain  $B=0.79$  and  $C=-1.7$ .

Figure 19 shows log amplitude versus distance, corrected for distance and yield using the values of B and C above obtained for all the seismic data. Figure 20 shows the mean values for each event, of the data in Figure 19. Amplitudes from the explosions with narrow pulses appear to be slightly lower than amplitudes from wide pulse events, but not by enough to be sure that the difference is significant.

We next examine the far-field body wave magnitude,  $m_b$ , data of Table 1 in order to uncover any significant differences between  $m_b$  values from the explosions with narrow near-field particle velocity pulses and those with wide pulses. Figure 21 shows the best fit line for  $m_b$  vs. yield for the 13 Degelen explosions for which we have such data, while Figure 22 shows the best fit line for just the 3 narrow pulse explosions. Figure 23 shows the best fit line for just the 7 explosions of the free-field wide pulse subset, eliminating 3 small yield events that give near-field particle velocity pulse shapes that look more like block motion than free-field.  $m_b$  from explosions with narrow pulses in the near field appear to be slightly higher than  $m_b$  from wide pulse explosions, but not by enough to be sure that the difference is significant.





**Figure 18.** Mean log amplitude vs. log yield for 5 wide pulse (squares) and 3 narrow pulse events (diamonds). Confidence intervals are one standard deviation. There is no apparent separation of the two groups, as the very optimistic confidence intervals overlap nearly completely.

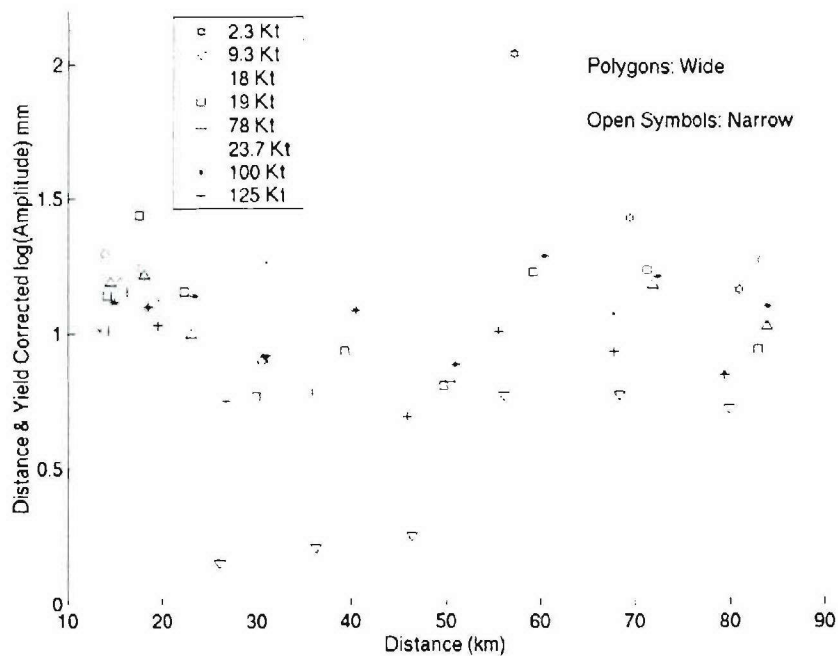


**Figure 19.** Distance and yield corrected log amplitudes of vertical seismograms recorded from 13 to 84 km distance. Open symbols (+, \*, and x) are used for events that have narrow velocity pulses in the near field, and polygons are used for events that have wide pulses in the near field.

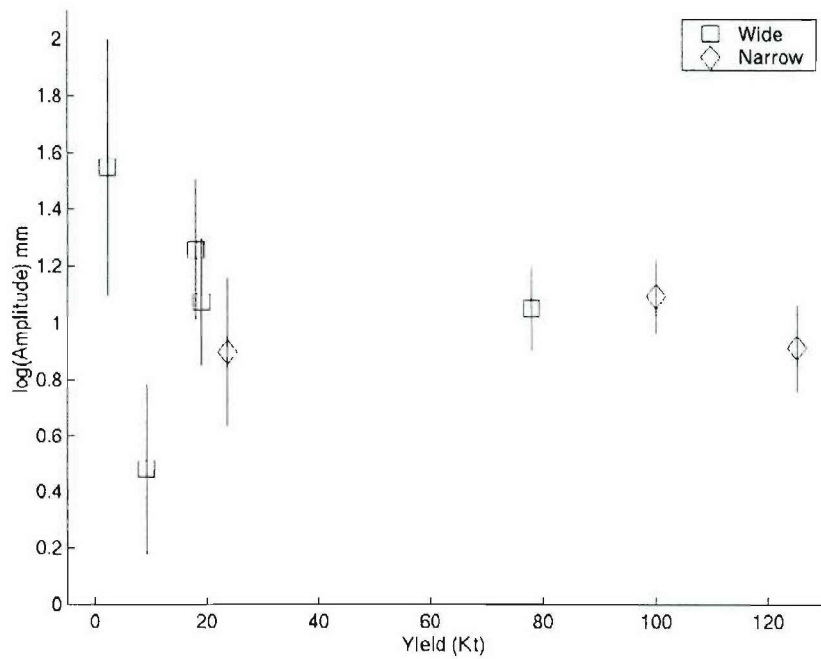


**Figure 20.** Mean values with one standard deviation confidence intervals for each event, for the data shown in Figure 19.

It is not clear why the differences in near field particle velocity pulses between explosion subsets apparently are not seen in either the near regional or far-field data from these explosions.

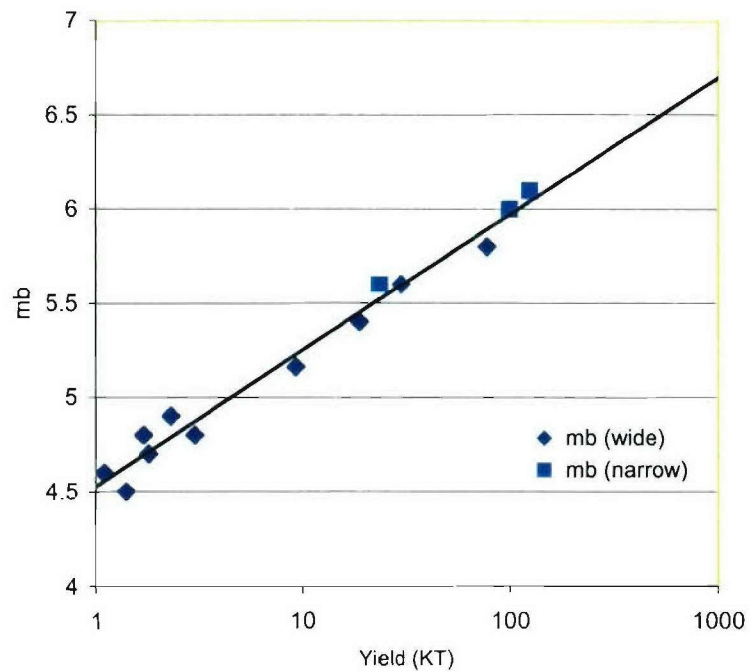


**Figure 21.**  $m_b$  vs. yield for all 13 Degelen events with known  $m_b$  and yield. The best fit line is  $m_b = 0.72 \log_{10} Y + 4.53$ .

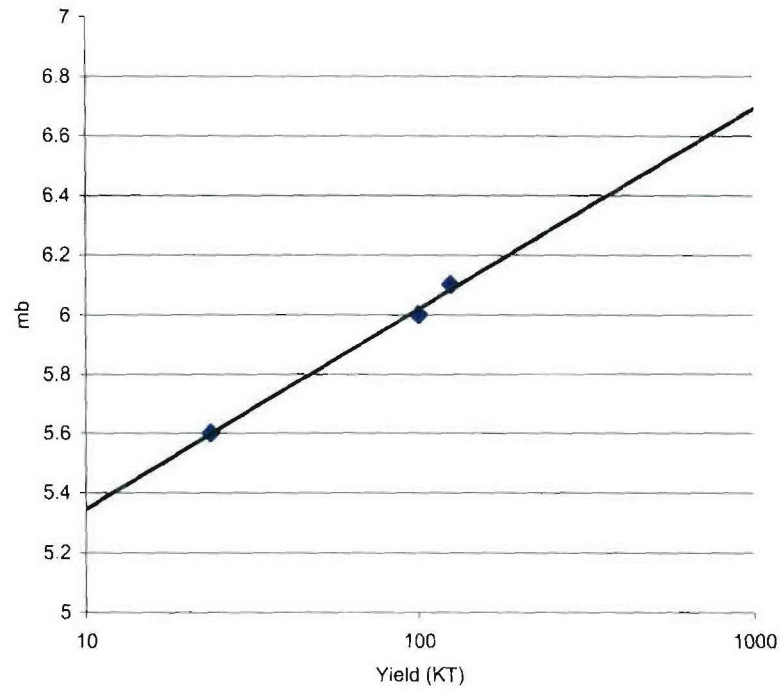


**Figure 22.**  $m_b$  vs. yield for the three narrow pulse events. The best fit line is  $m_b=0.67\log_{10}Y+4.67$ .

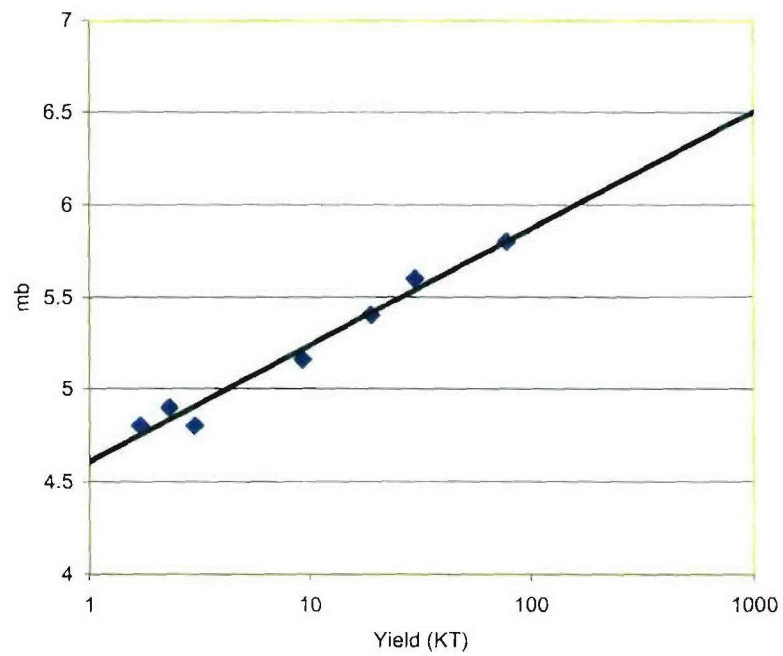


**Figure 23.**  $m_b$  vs. yield for the 7 wide-pulse Degelen events that show good free-field near field data. The best fit line is  $m_b=0.63\log_{10}Y+4.60$ .

### SECTION 3

## NUMERICAL MODELING OF U. S. EXPLOSIONS

The parameters used in numerical simulations of underground nuclear explosions are constrained by laboratory material properties tests and by direct observations of ground motion from underground explosions. Quasi-static laboratory tests on small rock samples are used to determine the following parameters: density, elastic moduli, pressure-volume (P-V) relation, material strength, porosity, and water content. Of these quantities, the density, moduli, and P-V relation seem to be quite consistent with *insitu* rock properties. In brittle hardrocks such as granite, porosity and water content are more variable *insitu* due to the presence of joints and are therefore less well constrained by laboratory data. Laboratory measurements of strength for brittle hardrocks seem to be very inconsistent with *insitu* strength as inferred by modeling of underground explosions. In particular, finite difference calculations of ground motion in granite, made using the laboratory measurements of shear strength, have invariably given much narrower particle velocity pulses and much smaller displacements than those measured in the field.

Constitutive models have been developed (Rimer and Lie, 1982, Rimer, et al., 1984) which attribute this weaker behavior of *insitu* granite and other rocks under explosive loading to ground-motion-induced rock damage or pore fluid pressure increases. These models have been shown by Day, et al, (1983) and Rimer, et al, (1986), (1987), using one- and two-dimensional calculations, to accurately reproduce the pulse broadening and most other aspects of the ground motion data from U.S. events in granite (PILEDRIIVER, for example). The models for granite have since been used to simulate the seismic source function from explosions conducted in the Soviet Union (Stevens, et al, 1991, for example). Figure 2 of Section 1 compares the particle velocity measurements at working point depth from the 62 kt PILEDRIIVER event with the results of the pile570 numerical simulation, made using the effective stress model discussed in Rimer, et al (1984, 1998, 1999). Numerical results from pile570 are also in good agreement with the measured cavity radius and with the estimated seismic source function (Table 4).

**Table 4.** United States explosions in granite.

Explosion	Yield (kt)	Measured Cavity Radius (m)	Calculated (570) Cavity Radius (m)
PILEDRIIVER	62.0	40.1/44.5	42.5
HARDHAT	5.9	19.4	19.4
SHOAL	12.5	26.8	24.9

For this simulation, effective stress model parameters were calibrated to best match the velocity peak and pulse shape at the closest-in gauge station (B-SL). This required a rapid buildup of pore pressure during the loading, leading to a large strength reduction very near the propagating shock front. Note that the pulse shapes at all four stations are rather consistent, with all including a long duration shallow negative velocity pulse. The peak velocities at the two smallest ranges agree very well with the simulation, but the measured peaks at the two larger ranges are a factor of two or more lower than the calculated peaks. The two closest PILEDRIIVER



gauges were located along roughly a 180 degree different azimuth than the other more distant gauges. However, a connection between possible site anisotropies and the measured ground motions has never been established. It should be noted that the 5.9 kt HARDHAT event, which was detonated in similar rock, near the later PILEDRIIVER event, but at a shallower depth of burial, gave particle velocity pulses which were more similar to the PILEDRIIVER pulses at the larger ranges. (See Rimer, Stevens, and Day, 1987, for a comparison between the results of the pile570 simulation and the HARDHAT measurements.)

The constitutive models used in these simulations are phenomenological in nature and do not explicitly account for the dynamic response of the *insitu* fractures in the source environment. That is, crystalline rock massifs in the earth's crust are heterogeneous over a wide range of scales from micro-cracks in grains at the micron scale to faults and joints which span many tens of kilometers. It has been observed that this fracture heterogeneity is responsible for nonlinear effects near the source of underground explosions which affect seismic coupling and the resultant seismic waveform. Very near the source, pre-existing cracks nucleate new fractures which granulate the rock, thereby significantly reducing its shear strength and elastic moduli. At greater distances, a network of radial tension cracks are formed which also degrade the mechanical properties of the rock. Even at large distances, movement on pre-existing faults and joints can produce significant deviations from numerical computer simulations which assume a simply connected elastic continuum.

Over the past several years, Professor Sammis and his associates at the University of Southern California have been working to understand the physics and micro-mechanics describing the nucleation and growth of new fractures from pre-existing cracks in crystalline rock under the compressive loading states inherent in laboratory tri-axial compression tests. Similar compressive loading states characterize the shock wave loading near the source of an underground explosion. This work (see Sammis and Ashby, 1988, Ashby and Sammis, 1990, and Sammis, 1991) has resulted in a damage mechanics formulation which is suitable for incorporation into numerical simulation codes. The model introduces a damage parameter, related to the increase in flaw size from its pre-shot average value. Damage accumulates as the flaws extend during the compressive loading and reaches some maximum value at which the rock fails unstably. The model gives no guidance to rock behavior after unstable failure. Incorporation of this damage mechanics formulation into a finite difference code, and subsequent testing and validation of the revised models, were the main topics of Rimer, et al (1998, 1999). Adaptation of the Sammis damage mechanics model for use in the ground motion simulation code is summarized in Rimer, et al (1998). The key input parameter to this model, in addition to the usual elastic moduli, is the average initial flaw size at the rock site. Since unstable compressive failure of a rock element is calculated using the adapted model to occur relatively early in the dynamic motions of interest here, i.e., usually near the propagating shock front, additional modeling was incorporated to complete the description of the stress field after this failure. Limiting the magnitude of deviatoric stresses in a failed rock element through the use of a standard friction law was shown to not provide sufficient strength reduction to simulate the ground motion measurements. In particular, calculated particle velocity time histories were still much narrower than the measured pulses for all reasonable choices of initial flaw size. The additional strength reduction required to sufficiently broaden the particle velocity pulses was obtained by using a shear damage model originally developed for soft rocks such as tuff,

described in Rimer and Proffer (1991). As discussed in Rimer et al (1999), this shear damage model was applied here only for rock elements that had experienced the onset of unstable compressive failure. Thus, a rock element was allowed to undergo significant damage before application of this treatment. The post-failure shear damage model performs an interpolation between the standard coefficient of friction of 0.60 and much lower “effective friction” values of 0.02-0.20 in the friction law used to limit deviatoric stresses. This linear interpolation is based on the maximum shear strain experienced by the failed rock element.

A series of calculations were made using the Sammis modeling, quantifying the effect of model parameters on particle velocity pulse shapes, cavity radius, and RDP. The simulation which best fits all of the PILEDRIIVER ground motion data is Run PD10. Comparisons with measured particle velocities are shown in Figure 24. In contrast with the results of pile570, made with the effective stress model, PD10 provides a much better fit to the PILEDRIIVER data at the two larger ranges, while underestimating peak velocities at the closest ranges. Subsequent analyses showed that the timing of the strength reductions for the two models were somewhat different, with the effective stress model providing an earlier reduction than the present damage model. However, calculated cavity radius and RDP with the new model are in as good agreement with the measurements as were those with the more traditional model.

The PD10 shear damage model begins the linear reduction in friction coefficient from the standard coefficient of 0.60 once failed elements experience a shear strain value,  $\epsilon_{crit}$ , of 0.1% or greater. The reduction to the lower effective friction coefficient of 0.02 for failed rock elements is completed for a shear strain value,  $\epsilon_{full}$ , of 3% or greater. In practice, calculated pulse widths were found not to be very sensitive to an order of magnitude increase in the value of shear strain used to initiate the interpolation since the onset of unstable failure usually occurred at much higher shear strains in the simulations. However, particle velocity pulse widths were sensitive to the choice of shear strain magnitude required for full strength reduction, with lower values of this parameter resulting in longer pulse duration and larger RDP. It is important to emphasize that while the shear damage model (or some other post-failure strength reduction model) is crucial to successful simulation of the ground motion data, it is the micro-mechanical damage mechanics model which primarily determines the size of the central core of weakened rock.

Another possible physical mechanism for the strength reduction and very low coefficients of friction required to simulate the wide particle velocity pulses is the “acoustic fluidization” concept proposed by Melosh (1979) to explain the low strengths (or very low angles of internal friction) apparent in a number of geologic processes, such as seismic faulting, impact crater slumping, and long runout landslides. The main concept of this proposed mechanism is that “sufficiently strong acoustic waves in rock debris can momentarily relieve the static overburden in limited regions of the rock mass, thus allowing sliding to occur in the unloaded region. If this happens frequently enough, flow of the entire rock mass results.” In terms of the explosively-induced ground motions of interest here, only the mass of failed or fractured rock would have the potential for acoustic fluidization. The dynamic fracturing process, by itself, provides enough energy to generate sufficiently strong oscillations post-failure to reduce the “effective normal stress/effective friction” to the low values required in the weak core region near the cavity.



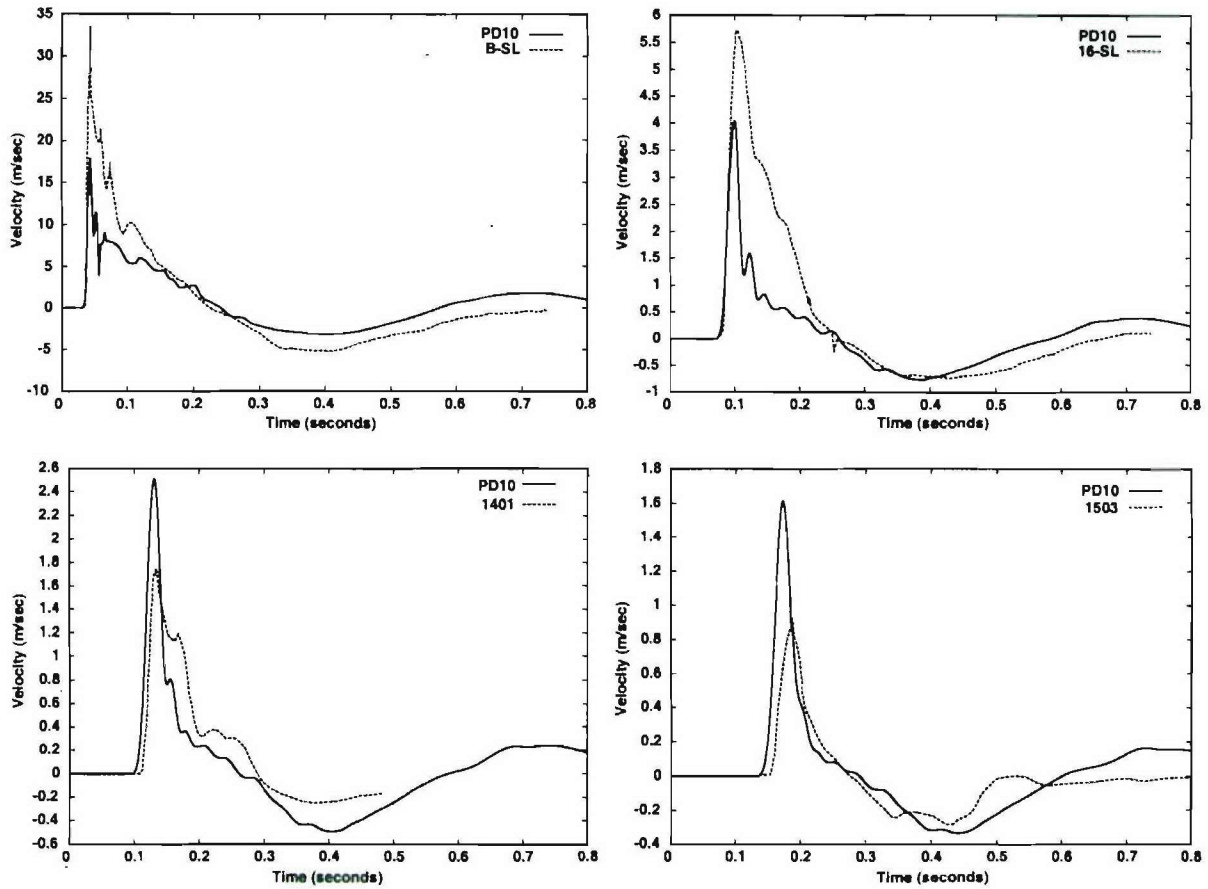


Figure 24. Calculated particle velocity pulses at four ranges for Run PD10 and PILEDRIVER measurements.

As reported in Stevens, et al (2001), we have implemented an approximate representation of acoustic fluidization within our nonlinear finite difference code and applied it to simulation of PILEDRIVER. First-principles implementation of the acoustic fluidization mechanism to the more dynamic and complex ground motion simulations is neither obvious nor direct. In particular, the mechanism presumes a strong vibrational mode, underlying the outward continuum motion of the rock mass surrounding the expanding pressurized cavity containing the vaporized rock and original bomb materials. Direct modeling of this vibrational mode is beyond the capabilities of the finite difference continuum code that computes the ground motion. However, some of the observed phenomenological features of the acoustic fluidization mechanism were included in this early version of our computational model. Simulation results using a more recent version of our acoustic fluidization model will be presented in this Section after more general discussions of both our modeling approach and of the other models used in our newer simulations of the PILEDRIVER data.

The data set from the PILEDRIVER event is being used here as a set of constraints to test out several competing mechanisms for both the “failure/rubblization process” and the post-failure “strength reduction” process. We have been concentrating on three specific strength reduction

mechanisms, the effective stress model, the shear-strain-based shock damage model (SS), and an acoustic fluidization model (AF). Application of any of these strength reduction models is explicitly limited to rock elements that have previously been failed and/or rubblized. Two rock failure/rubblization mechanisms are being used in these tests, the Sammis micro-mechanical damage mechanics model (SA) discussed above and a Yield/Failure Surface model (YF). In the present YF model, the onset of failure and rubblization in a rock element is defined using the failure surface obtained from laboratory tri-axial compression tests on fractured granite samples from the PILEDRIIVER site. We assume plastic yielding and a non-associated, no bulking, flow rule (radial return) and use the plastic work per unit volume,  $epw$ , done on a rock element after shear failure as the threshold to determine if the cell is rubblized. A standard friction law is used for rubblized rock. (The effective stress law simulation of Figure 2, pile570, used an earlier hybrid of the present YF failure model, i.e., the same failure surface and flow rule, with an  $epw$  of zero, but without a switch to a friction law post-failure.)

The PD10 simulation results of Figure 24, as reported in Rimer, et al (1999), used the Sammis Damage Mechanics-Shock Damage (SA-SS) model combination. Here, we will report the results of parametric numerical simulations of the PILEDRIIVER data made with other combinations of failure/rubblization and strength reduction algorithms. For each combination, we will show a table of results illustrating some of the effects of variations in model parameters on quantities such as final cavity radius,  $R_c$ , maximum overshoot of cavity,  $R_{max}$ , radial extent of failure, and RDP. In general, we will show comparisons between simulated and measured particle velocities only for the best fit case for each model combination (denoted by a \* next to the case number in each table of results).

In these comparisons, it should be noted that the noise in the waveforms immediately behind the shock front produced using the Sammis brittle failure model (Figure 24) is a consequence of the large strength reduction for failed rock (closer to the cavity) compared to the elastic (infinite strength) deviatoric behavior (in the undamaged rock outside of it) that was required for application of the Sammis model. (The Sammis brittle failure model is incompatible with likely plastic behavior very near the explosive source.) See Rimer, et al, 1999, for a discussion of the effects of numerical smoothing of the discontinuity between failed and damaged rock elements for the PD10 model. Use of the YF failure model instead of the SA model, in some cases, did not noticeably reduce this noise. This noise did not occur for the effective stress model results of Figure 2 because there the strength reduction occurs during the loading of the rock element, i.e., before high stress differences can occur.

Also, the elastic pressure-volume relation required by the SA model for undamaged rock is incompatible with the nonlinear loading relation measured on small samples of granite in the laboratory. For the YF cases to be discussed here, we chose to use the same elastic pressure-volume relation rather than the nonlinear loading relation. Simulation results, with the exception of peak particle velocities, were found to be insensitive to this choice of loading relation. The pile570 effective stress simulation did use the nonlinear loading relation.

All three model combinations to be discussed below (YF-SS, YF-AF, and SA-AF), as well as the SA-SS combination, use the Peyton failure surface algorithm for rocks described in Rimer, et al (1984), and also a reduction in shear modulus based on the maximum shear strain seen by the



rock element In the Peyton algorithm, the location of the failure surface in stress space is a function of the third deviatoric stress invariant. Thus, the friction law is represented here as

$$T_{\text{shear}} = bsl \ p$$

where  $T_{\text{shear}}$  is the strength in pure shear and  $p$  is the mean stress. For the parameters of the Peyton algorithm used here, a friction coefficient may be obtained from the values of  $bsl$  (or the reduced slope,  $bsfull$ , for the SS model) given in the parametric tables by multiplying  $bsl$  (or  $bsfull$ ) by  $\sim 1.15$ . The shear modulus reduction from its elastic value,  $G_0$ , of 207 kb, down to its lowest allowed value,  $G_{\text{dam}}$ , is accomplished using a linear interpolation in shear strain between  $epinit$ , where the modulus is  $G_0$ , and  $epfull$ , where the modulus is reduced to  $G_{\text{dam}}$ .

### 3.1 Results for YF-SS Model Combination

Table 5 shows the results of a subset of the parametric variations made using the YF-SS model combination to simulate the data set (particle velocity, cavity radius, RDP, etc.) from PILEDRIVER. All of the calculations shown were made using a plastic work parameter,  $epw$ , of 500 ergs/cm<sup>3</sup> as a requirement for rubblization. A higher value of  $epw$  would result in a later time for rubblization, a stronger rock, and thus narrower particle velocity pulses in the calculations. The shear strain, shear modulus, and friction slope parameters of the shear modulus and strength reduction models, defined earlier, are given for each parametric case.

**Table 5.** Results for PILEDRIVER simulations using the YF-SS model combination with  $epw = 500$  ergs/cm<sup>3</sup>.

Case #	Shear modulus reduction			Strength reduction				Results			
	$G_{\text{dam}}$ (kb)	$epinit$	$epfull$	$deinit$	$defull$	$bsl$	$bsfull$	RDP (10 <sup>3</sup> m <sup>3</sup> )	Failure (m)	Rmax (m)	Rc (m)
1	100	1e-3	1e-2	1e-2	5e-2	0.528	0.017	13.9	327	47.1	40.3
2	10	1e-3	1e-2	1e-2	5e-2	0.528	0.017	14.1	338	48.1	40.5
3	70	1e-3	1e-2	1e-2	5e-2	0.428	0.017	14.1	327	49.3	40.4
4	100	1e-3	1e-2	1e-2	5e-2	0.488	0.017	13.8	311	47.4	39.9
5	100	1e-3	6e-3	1e-2	5e-2	0.328	0.20	14.4	327	41.6	40.7
6	100	4e-4	1e-3	1e-3	3e-2	0.528	0.027	7.1	271	51.4	38.0
7	100	4e-4	1e-3	1e-2	3e-2	0.528	0.027	8.0	301	49.7	40.1
8	100	4e-4	1e-3	1e-2	3e-2	0.528	0.097	10.2	402	47.2	40.5
9	100	4e-4	1e-3	1e-3	3e-2	0.528	0.017	7.9	301	52.3	39.5
10*	100	4e-4	1e-3	1e-3	2e-2	0.528	0.017	9.4	291	55.0	39.5
11	100	4e-4	1e-3	1e-3	18e-3	0.528	0.017	6.9	360	58.7	38.6

Case 9, shown as Figure 25, uses the same parameters for shear modulus and strength reduction as did Run PD10, with the SA-SS model. This calculation gives considerably higher peak velocities and slightly narrower pulses than PD10. The best fit to the particle velocity data with the YF-SS combination, Case 10, shown as Figure 26, used a reduced  $defull$  to widen the positive pulse. The smaller but weaker core of rubble (a reduced extent of failure in Table 5)

also resulted in larger outward velocities at 0.6–0.7 sec, after cavity rebound than given by the data. Both static RDP and cavity radius are smaller in Cases 9 and 10 than given by PD10 and the data. However, a further reduction in defull in Case 11 in an attempt to increase the RDP resulted in too large a positive pulse, a much larger core of rubble, and large inward velocities that gave smaller values of final cavity radius and static RDP.

Other parametric variations of Table 5 were found to give the desired larger RDP and cavity radius, but at the expense of considerably smaller positive and/or negative pulses than given by the measurements. We were not able to provide as good a fit overall to the PILEDRIIVER data with the YF-SS combination as was done using the SA-SS models.

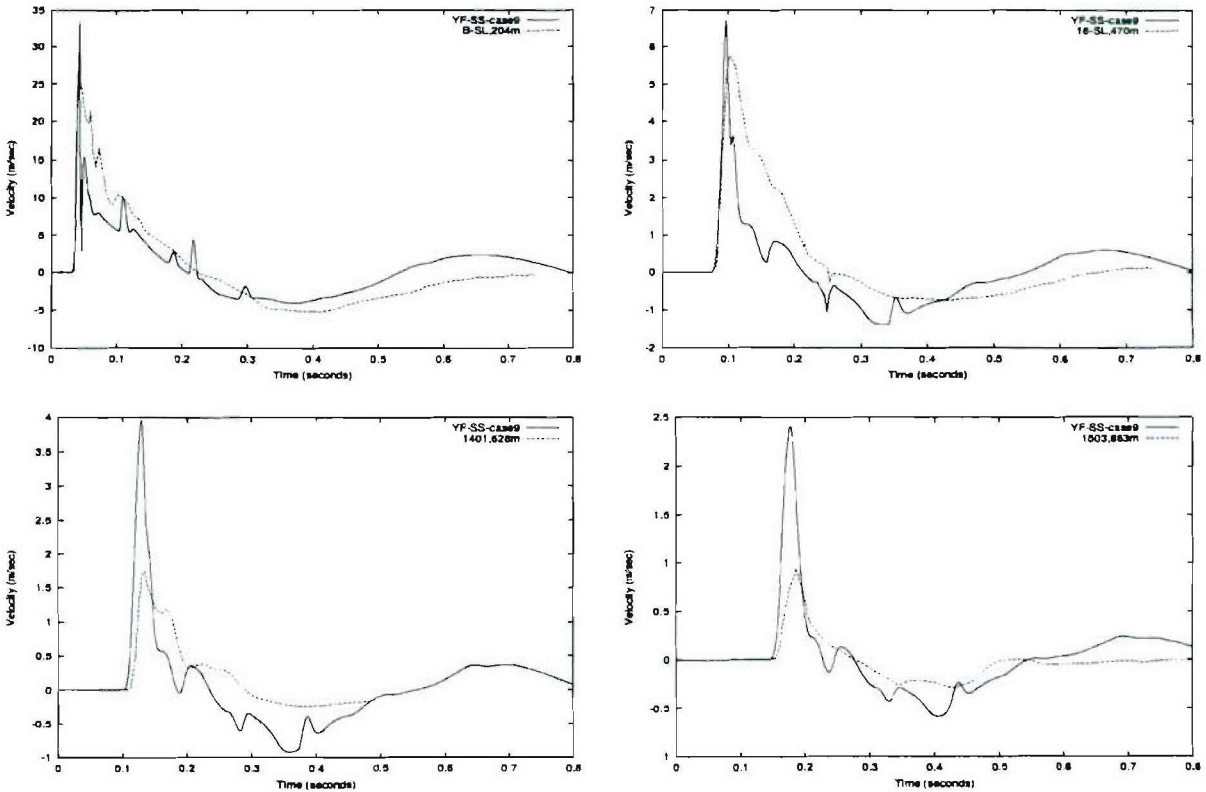


**Figure 25.** Calculated particle velocity pulses at four ranges for YF-SS case 9 vs. PILEDRIIVER data.

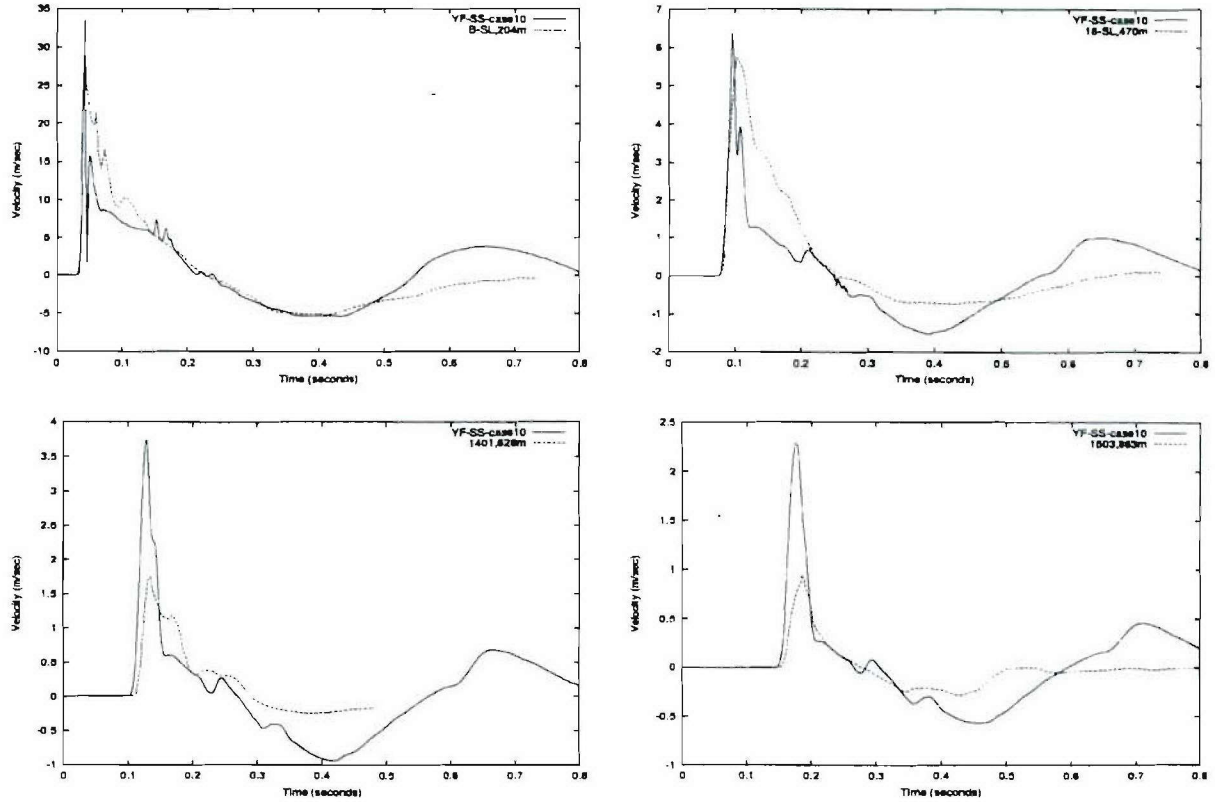


**Figure 26.** Calculated particle velocity pulses at four ranges for best fit YF-SS case 10 vs. PILEDRIVER data.

### 3.2 The Revised Acoustic Fluidization Model

The earlier implementations of the AF model discussed in more detail in Stevens, et al (2001) assumed that once a cell has failed, it is subject to acoustic fluidization, and that the acoustic fluidization occurs only after the kinetic energy reaches some critical threshold level. The second assumption is not quite right and is replaced here by the incorporation of the “block model” described in Melosh and Ivanov (1999), which represents the motion of a system of oscillating blocks as a viscous motion with an effective kinematic viscosity whenever shear stress is larger than the Bingham limit. This shear stress dependence replaces the dependence of the frictional strength upon kinetic energy in our earlier implementations.

In the finite difference code, the oscillation or vibration velocity,  $svib$ , in a failed element is given as a function of the peak velocity,  $vp$ , in the element by:

$$svib = cvib \, vp \, \exp(-dt/\tau)$$

where  $cvib$  is the vibration coefficient,  $\tau$  is the decay time, and  $dt$  is the change in time from the beginning of the oscillation. The pressure due to block oscillations,  $pvib$ , is computed from the vibration velocity using:

$$pvib = svib \, c \, \rho$$



where  $c$  is the P-wave speed and  $\rho$  is the density. This pressure is further required to be less than some arbitrary maximum pressure allowed for acoustic fluidization,  $p_{max}$ . (The simulated particle velocities are relatively insensitive to  $p_{max}$ .)

The code computes a viscous stress,  $Stvis$ , from the strain rates, the friction law, and  $p_{vib}$  as follows:

$$Stvis = Yb + \rho kvis Erate$$

where  $Erate$  is the shear strain rate invariant,  $kvis$  is the kinematic viscosity, and  $Yb$  is a reduced frictional strength due to acoustic fluidization given by:

$$Yb = bs (p - p_{vib})$$

where  $bs$  is the frictional slope and  $p$  is the mean stress in the element. (We note again that the code uses the Peyton failure surface algorithm and that  $bs$  may be easily related to the slope  $bsl$  defined earlier and given in our parametric tables. The rock frictional strength without acoustic fluidization,  $Ya$  is given by:

$$Ya = bs p.$$

Before acoustic fluidization occurs in an element, its strength is given by  $Ya$ . If the viscous stress,  $Stvis$ , is less than  $Ya$ , the code reduces the strength to  $Stvis$ . Thus, acoustic fluidization may reduce the local friction and reduce the effective strength of the rock to as low as  $Yb$ . On the other hand, the time decay in the oscillation velocity eventually returns the rock to its normal state.

The revised AF model coding includes 4 arbitrary coefficients, the decay time, the kinematic viscosity, the vibration coefficient, and the relatively insensitive  $p_{max}$  (a value of  $4 kb$  was used in almost all of our simulations of NTS and Degelen explosions). In almost all of our parametric calculations for PILEDRIIVER with this model, the decay time,  $\tau$ , was fixed at 10 sec so that the rubblized rock could remain weak to provide the required wide pulses. Thus, the AF model parameter set was reduced to 2 arbitrary coefficients for PILEDRIIVER. However, Section 4 will show that much smaller decay times are needed to fit the Degelen pulses.

### 3.3 Results for SA-AF Model Combination

In this model combination, the onset of failure and start of acoustic fluidization is defined by the Sammis damage mechanics model using an initial damage parameter of 0.1 and an initial flaw size of 1 cm for these calculations. Table 6 shows the results of a subset of the parametric variations made using the revised AF strength reduction model to simulate the PILEDRIIVER data. The best fit to the particle velocity pulses with these models, Case 7, is shown as Figure 27.



**Table 6.** Results for PILEDRIVER simulations using the SA-AF model combination.

Case #	Shear modulus reduction			Acoustic fluidization		Friction law	Results			
	Gdam (kb)	epint	epful l	cvib	kvis (cm <sup>2</sup> /s)		RDP (10 <sup>3</sup> m <sup>3</sup> )	Failure (m)	Rmax (m)	Rc (m)
1	87	4e-3	1e-2	1e-2	1e2	0.228	15.7	332	43.4	41.9
2	100	4e-3	1e-2	1e-2	1e2	0.228	15.8	333	43.3	41.9
3	100	1e-3	1e-2	5e-2	1e2	0.228	16.4	384	49.7	42.3
4	100	1e-3	1e-2	5e-2	1e3	0.228	16.4	384	49.7	42.3
5	100	1e-3	1e-2	1e-1	1e1	0.528	15.1	355	45.2	41.3
6	100	1e-3	1e-2	2e-1	1e1	0.528	16.7	408	53.0	43.4
7*	80	1e-3	1e-2	2e-1	1e2	0.528	16.0	414	53.2	42.7

For this model combination, it was fairly easy to simulate both the cavity radius and RDP data. Calculated particle positive velocity pulses at the two closest-in stations show lower peaks and are noisy, but provide reasonable negative pulses. Overall, the best fit simulation with the SA-AF model combination shown as Figure 27 is not as good as PD10 but probably superior to the simulation made using the YF-SS combination because of the better match to cavity radius and RDP.

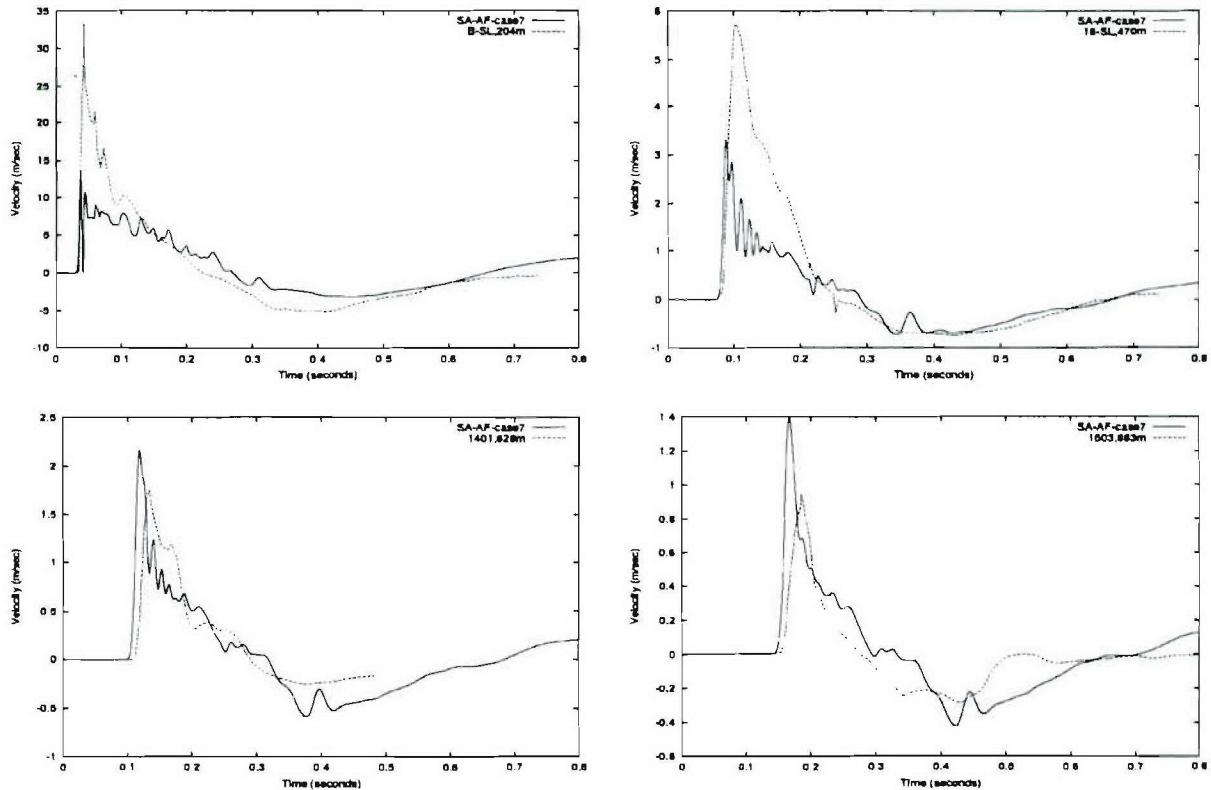


**Figure 27.** Calculated particle velocity pulses at four ranges for best fit SA-AF case 7 vs. PILEDRIIVER data.

### 3.4 Results for YF-AF Model Combination

In this model combination, failure and rubblization, and the onset of acoustic fluidization is defined by shear failure and the accumulation of 500 ergs/cm<sup>3</sup> of plastic work in a rock element. Table 7 shows the results of a subset of the parametric variations made using the revised AF strength reduction model. Particle velocity pulses from the best fit to the PILEDRIIVER data with these models, Case 4, is shown as Figure 28.

**Table 7.** Results for PILEDRIIVER simulations using the YF-AF model combination with epw =500 ergs/cm<sup>3</sup>.

Case #	Shear modulus reduction			Acoustic fluidization		Friction law	Results			
	Gdam (kb)	epinit	epfull	cvib	kvis (cm <sup>2</sup> /s)	bsl	RDP (10 <sup>3</sup> m <sup>3</sup> )	Failure (m)	Rmax (m)	Rc (m)
1	80	4e-3	1e-2	2e-1	1e2	0.528	16.3	311	51.6	40.5
2	80	4e-3	1e-2	2e-1	1e3	0.528	16.3	311	51.6	40.5
3	80	4e-3	1e-2	1.8e-1	1e1	0.528	9.9	291	50.8	37.6
4*	87	4e-3	1e-2	1.8e-1	1e2	0.528	14.7	360	54.8	41.8
5	87	4e-3	1e-2	2e-1	1e2	0.528	12.1	384	56.7	39.8
6	86.5	4e-3	1e-2	1.8e-1	1e2	0.528	11.1	301	51.5	38.0

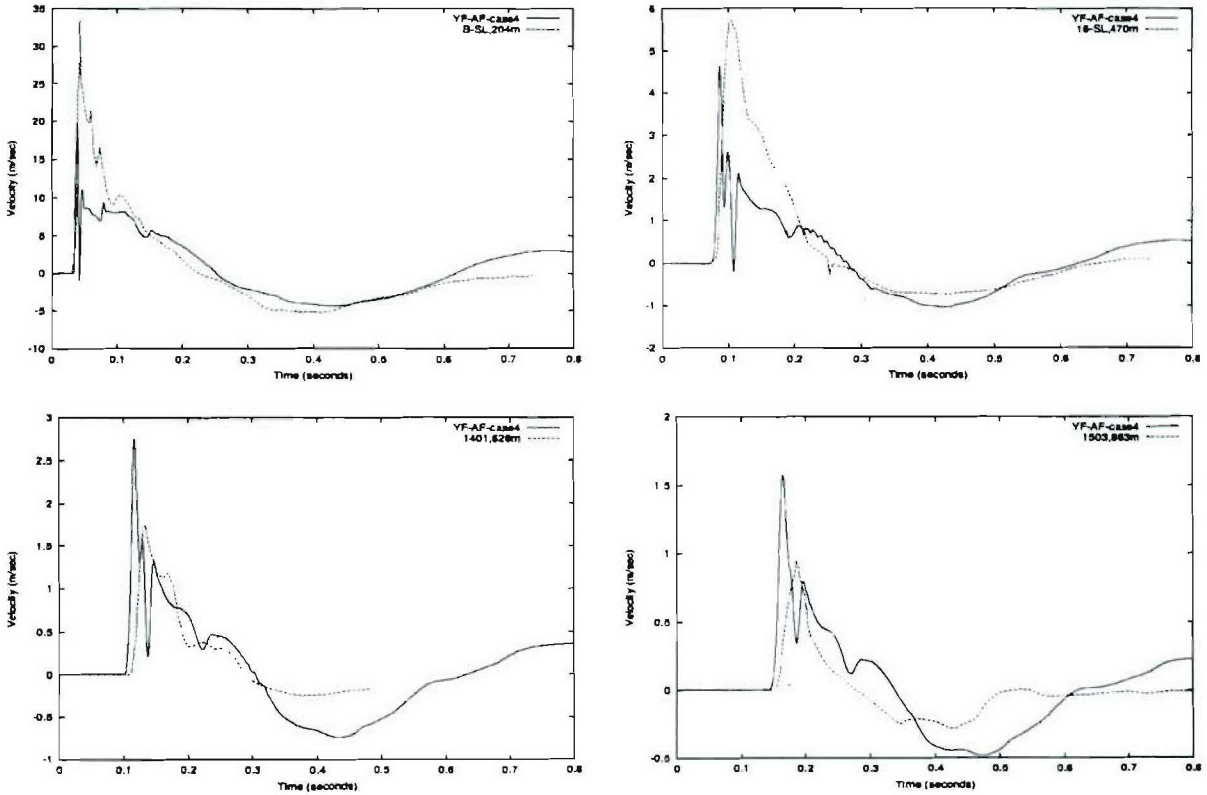


**Figure 28.** Calculated particle velocity pulses at four ranges for best fit YF-AF case 4 vs. PILEDRIIVER data. Case 4 using the YF-AF model provides a good match to cavity radius, RDP, and pulse widths. However, these pulses are even noisier behind the peaks than were those in Figure 27, for the SA-AF model. Use of the YF failure algorithms clearly gives higher peak velocities than use of the Sammis algorithms, for both the best fit combinations using the AF strength reduction model and those using the SS shock damage model.

Some observations we have made from the results of the acoustic fluidization parametric studies are consistent with those from parameter studies made using other strength reduction models to simulate PILEDRIIVER. In general, a weak central core of rock (here, due to acoustic fluidization) is required to match the large positive pulse widths, while a strong inward push (rebound) from the stronger rock outside this weakened central core is needed to simulate the long negative pulses. The results of the acoustic fluidization parametric calculations indicate that a range of cavity overshoot from 53-55 m and a rebound of 10-13 m would be ideal, with a smaller overshoot requiring a smaller rebound within these ranges to achieve the desired PILEDRIIVER cavity radius and RDP.

In summary, the near and far field data from the PILEDRIIVER event has provided a set of constraints to test out several competing mechanisms for both the “failure/rubblization process” and the post-failure “strength reduction” process. We have been concentrating on three strength reduction mechanisms and two rock failure/rubblization mechanisms.

#### Strength Reduction Mechanisms.

1. Effective Stress – Dynamic buildup of fluid pressure in joints and cracks that occurs during compaction results in reduced effective strength of the rock. Presumes no dilatant volume increases (bulking) that would reduce fluid pressure.
2. Acoustic Fluidization – Oscillations in rubblized rock greatly reduce confining pressure locally and therefore reduce strength.
3. Shock Damage – Rock element stretches laterally during the divergent outward ground motion. Strength reduction to a damaged failure surface is a function of the maximum shear strain in the element.

#### Failure and Rubblization Processes.

1. Yield and Failure Surfaces Coincide – No Bulking. Failure surface for fractured granite from laboratory tests. For the acoustic fluidization model, finite plastic work is required for rubblization. Standard friction law used for rubblized rock.
2. Sammis Damage Mechanics – Brittle failure under compressive loading due to elongation and coalescence of pre-existing small cracks in the rock increases damage parameter. After unstable failure, standard friction law used for rubblized rock.

Parameter studies have been completed using both competing failure/rubblization process together with each of the strength reduction mechanisms that are appropriate to the chosen failure process. Reasonable simulations of the PILED RIVER data (particle velocity pulses, cavity radius, RDP) have been obtained for each of the following combinations:

Yield/Failure Surface – Effective Stress  
Sammis Damage Mechanics – Shock Damage  
Sammis Damage Mechanics – Acoustic Fluidization  
Yield/Failure Surface – Acoustic Fluidization  
Yield/Failure Surface – Shock Damage.

The above model combinations have been ordered from best overall fit to the PILED RIVER data down to poorest fit.

It should be noted that the pore pressure buildup in the effective stress process is not compatible with the crack opening in the Sammis model. In the next section, we use simulations of the near and far field data from Degelen events to further evaluate and perhaps discriminate between these competing physical mechanisms.



## SECTION 4

### NUMERICAL MODELING OF DEGELEN EXPLOSIONS

As shown in Section 2, the near-field particle velocity measurements from those 14 of the Degelen explosions that appear to be giving free-field pulse shapes may be separated into wide pulse and narrow pulse subsets after scaling to a common yield of 62 kt. The wide pulse Degelen subset was also shown to encompass a significant gradation of pulse widths, from a very few that are somewhat wider than the PILEDRIVER records at similar large scaled ranges, down to those much narrower than PILEDRIVER, but still distinguishable from the much shorter duration narrow pulse Degelen subset. Parametric calculations have been performed for each of these subsets using four of the combinations of failure and strength reduction mechanisms that were discussed in Section 3 above. We did not apply the effective stress model in our Degelen simulations. A more detailed acoustic fluidization strength reduction model, based on the work of Melosh and Ivanov (1999) and on more recent personal communications with Boris Ivanov, was used in these Degelen simulations in place of earlier Implementations 1 and 2 summarized in Stevens, et al (2001). A description of this model was given in Section 3.

The results of these parametric calculations were tested against both the particle velocity measurements shown earlier in Figures 10-12 of Section 2 and the Degelen constraints given in Table 8. Note that the range of measured Degelen cavity radii in Table 8, when scaled to 62 kt, are all smaller than the best estimates for the cavity radius from PILEDRIVER (40.1 and 44.5 m). See Rimer, et al, (1998), (1999), respectively, for summaries of the post-shot damage data and for detailed comparisons between these data and parametric simulations made using the Sammis failure model and shock damage. Simulation DE12, shown earlier in Figures 8-12 of Section 2, provides a good match to Degelen cavity radius (31.1 m), post-shot P-wave speeds, and some of the measured particle velocity pulses, but gives a failure extent of 368 m, much larger than the measured damage extent given in Table 8. This simulation also gives a static RDP of about 15,000 m<sup>3</sup>, similar to PILEDRIVER simulations.

**Table 8.** Degelen modeling constraints (scaled to 62kt).

Parameter	Value
Damage extent (m)	160-200
Cavity radius (m)	28-36
P-wave speed post-shot near cavity (m/s)	1500-2500 (reduced from ~5175 pre-shot)
Overburden pressure (bars)	29-87* (120 for PILEDRIVER)

\*All of the Degelen simulations to date have been made using an overburden pressure of 50 bars.

The parametric calculations made for the 9 wide pulse explosions indicate that each of the 4 model combinations can be made to fit most of the features of the Degelen data. We have ordered the best simulations with each of the four model combinations from best overall fit to worst fit (although all are reasonably good) as follows:

- 1) Sammis Damage Mechanics – Shock Damage (SA-SS).
- 2) Yield/Failure Surface – Acoustic Fluidization (YF-AF).
- 3) Yield/Failure Surface – Shock Damage (YF-SS).
- 4) Sammis Damage Mechanics – Acoustic Fluidization (SA-AF).

This ordering was based both on our general impressions of the agreements and differences, on average, between simulated and measured pulses, and on a more systematic analysis of individual pieces of these agreements and differences which is summarized in Table 9 along with some other results of the simulations that may be compared with the model constraints given in Table 8 above. In this ordering, we have weighted agreements with details of the positive velocity pulses more heavily than agreements with the more variable negative pulse. It should be noted that all of the results in Table 9, except for the SA-SS combination, are somewhat different from those reported earlier. Additional parametric calculations have improved the simulations using the YF-SS model combination, and our AF model has also been improved.

**Table 9.** Simulation results and comparisons between some characteristics of measured Degelen pulses and best fit wide-pulse simulations using 4 combinations of failure/rubblization and strength reduction models.

Failure/rubblization model	Yield/Failure Surface (YF)		Sammis Damage Mechanics (SA)	
	Acoustic fluidization (AF)	Shock damage (SS)	Acoustic fluidization (AF)	Shock Damage (SS)
Cavity radius (m)	33.8	32.1	32.6	34.5
Static RDP ( $10^3 \text{ m}^3$ )	10.4	9.9	7.7	11.0
Cavity rebound (m)	1.2	1.0	0.1	0.2
Failure extent (m)	196	168	266	322
Reduced P-velocity near cavity (m/s)	3967	4175	4013	3100
Peak velocity relative to data	good	higher	too low	good
Positive pulse width relative to data	good	narrower	narrower	good
Positive pulse shape overall	good	good	good	good
Negative amplitude relative to data	deeper	deeper	good	good
Negative pulse width relative to data	narrower	narrower	narrower	best
Post-shock behavior	smooth	smooth	noisy	smooth

The results of the parametric simulations of the wide pulse Degelen data made using each of the four model combinations in Table 9 will be discussed next. For each model combination, we will show both parametric tables of results and particle velocity comparisons for the best fit case (denoted by an \* in the table). It should be emphasized that different model parameters are required to best fit the wide pulse Degelen data than were used in Section 3 to best fit the PILEDRIVER data.

#### 4.1 Degelen Results for SA-SS Model Combination



Our subjective observations define the best simulation to date using the SA-SS model combination (case 7 of Table 10) as our best fit so far to the wide pulse Degelen data. Perhaps, this should have been expected, since we certainly have had more extensive experience with the effects of parametric changes in these models dating back to Rimer, et al (1999) and the DE12 simulation. However, our best efforts so far have not resulted in simulations using the other model combinations that provide as good a fit to as many (but certainly not all) of the wide pulse records as did SA-SS case 7 of our parameter study. Figures 29 and 30 show comparisons between the simulated and measured particle velocity pulses from SA-SS case 7. Note that in comparison with the DE12 results shown earlier in Figures 10 and 11 of Section 2, the Case 7 peak velocities are smaller, and positive pulses are narrower, thus greatly increasing the quality of the match to much of the Degelen wide pulse data set.

**Table 10.** Results for Degelen wide pulse simulations using the SA-SS model combination.

Case #	Model		Results				
	Gslp (kb)	Do	RDP ( $10^3\text{m}^3$ )	Failure (m)	Rmax (m)	Rc (m)	Reduced P-vel. (m/s)
1	400	0.1	16	372	30.4	30.3	2300
2	400	0.01	9.7	208	33.2	32.7	3000
3	40	0.01	9.2	191	32.7	32.5	4900
4	80	0.01	9.3	195	32.8	32.6	4740
5	200	0.01	9.2	204	32.2	32.0	4280
6	200	0.1	9.7	296	35.4	35.2	3900
7*	300	0.1	11	322	34.5	34.3	3100
8 bsfull=0.4	300	0.1	8.3	296	29.1	29.0	3200
9	80	0.1	9.6	281	35.6	35.5	4700
10	40	0.1	9.5	276	35.5	35.4	4900

This improvement was accomplished by a single, but significant, change in the DE12 parameter set (Table 6-1 of Rimer, et al, 1999), i.e., a reduction of the slope, Gslp, from 400 to 300 kb, in the linear shear modulus reduction vs. damage parameter, D, relation described by Rimer et al. (We used a simpler, shear-strain dependent shear modulus reduction model for the PILEDRIVER simulations of Section 3.) This parameter change from DE12 results in less reduction in shear and bulk moduli near the cavity, less dilatant behavior near the cavity, less P-wave velocity reduction near the cavity, and thus a weaker (narrower), dilatant, second positive pulse, a smaller RDP, and about a 10% larger final cavity radius. Note also that all of the cases of Table 10, except for Case 8, used bsfull = 0.2, and shear strain values, deinit and defull, of 0.02 and 0.06, respectively, in the SS strength reduction model, while PILEDRIVER results with this model used bsfull = 0.017, i.e., a much lower damaged friction slope, and strain values of 0.001 and 0.02, respectively.

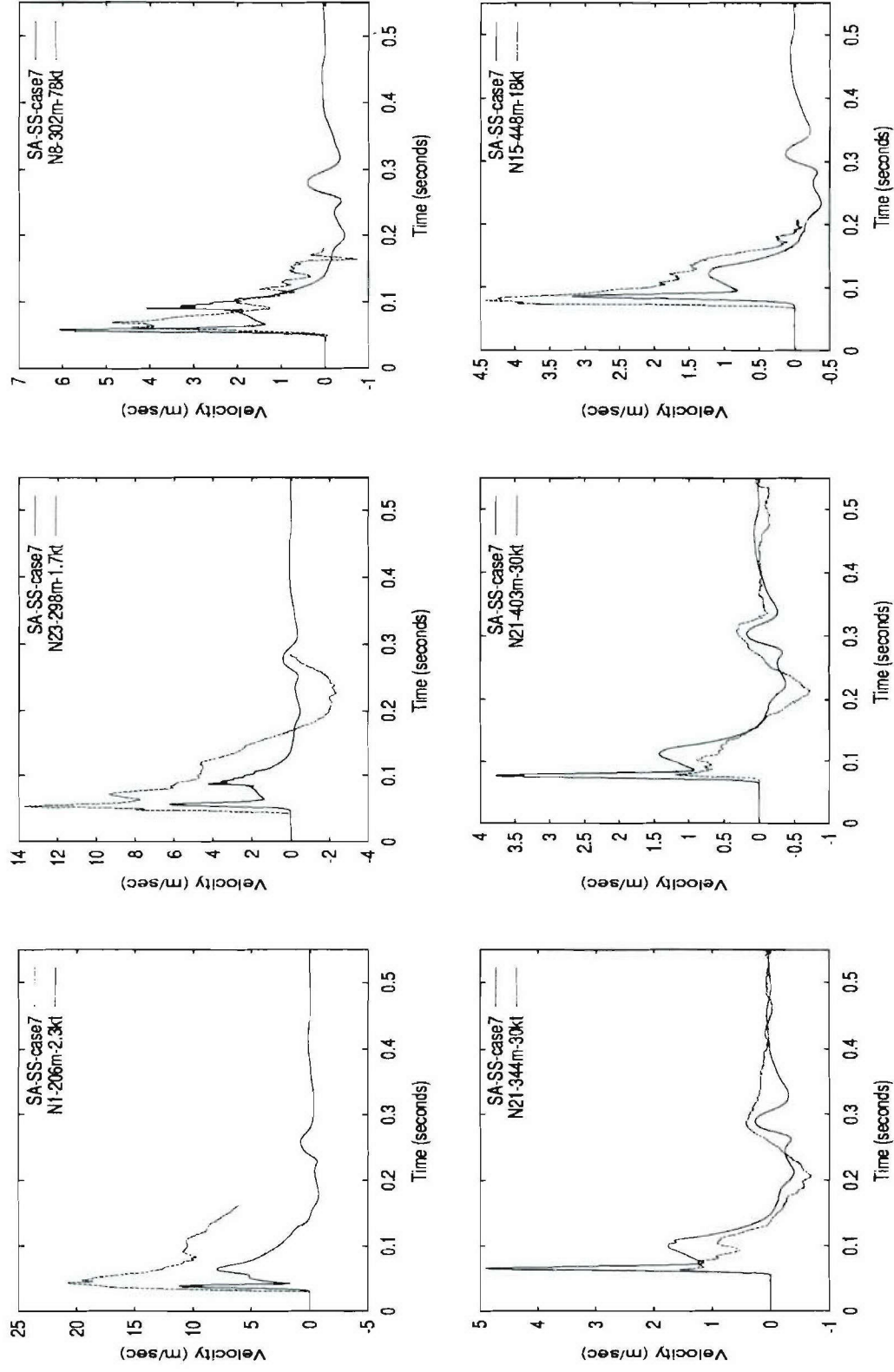


**Figure 29.** Comparison between particle velocity pulses at the smaller scaled ranges from the wide pulse Degelen data subset and the results of the best fit simulation (case 7) using the SA-SS model combination (the solid curves).



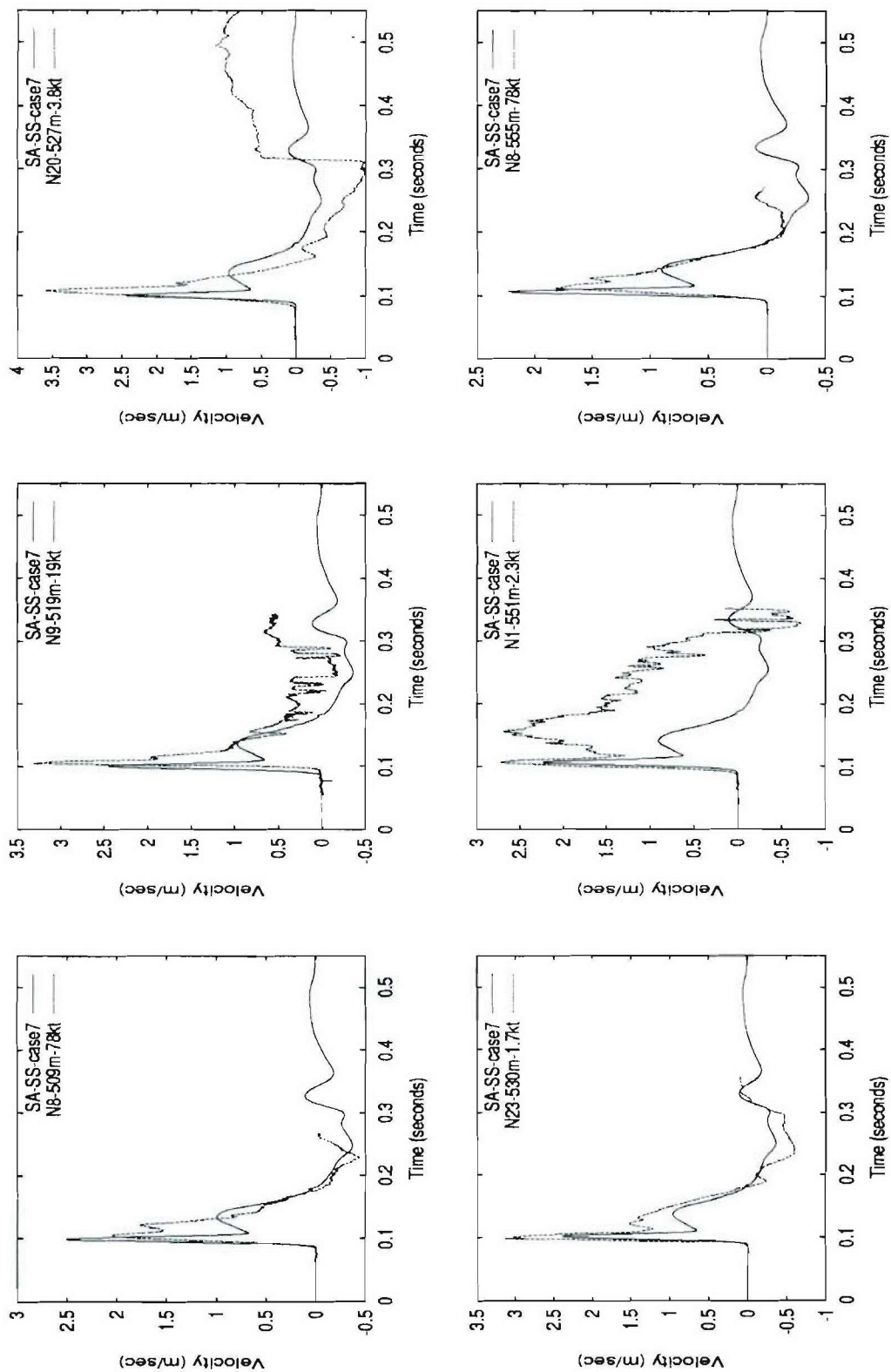
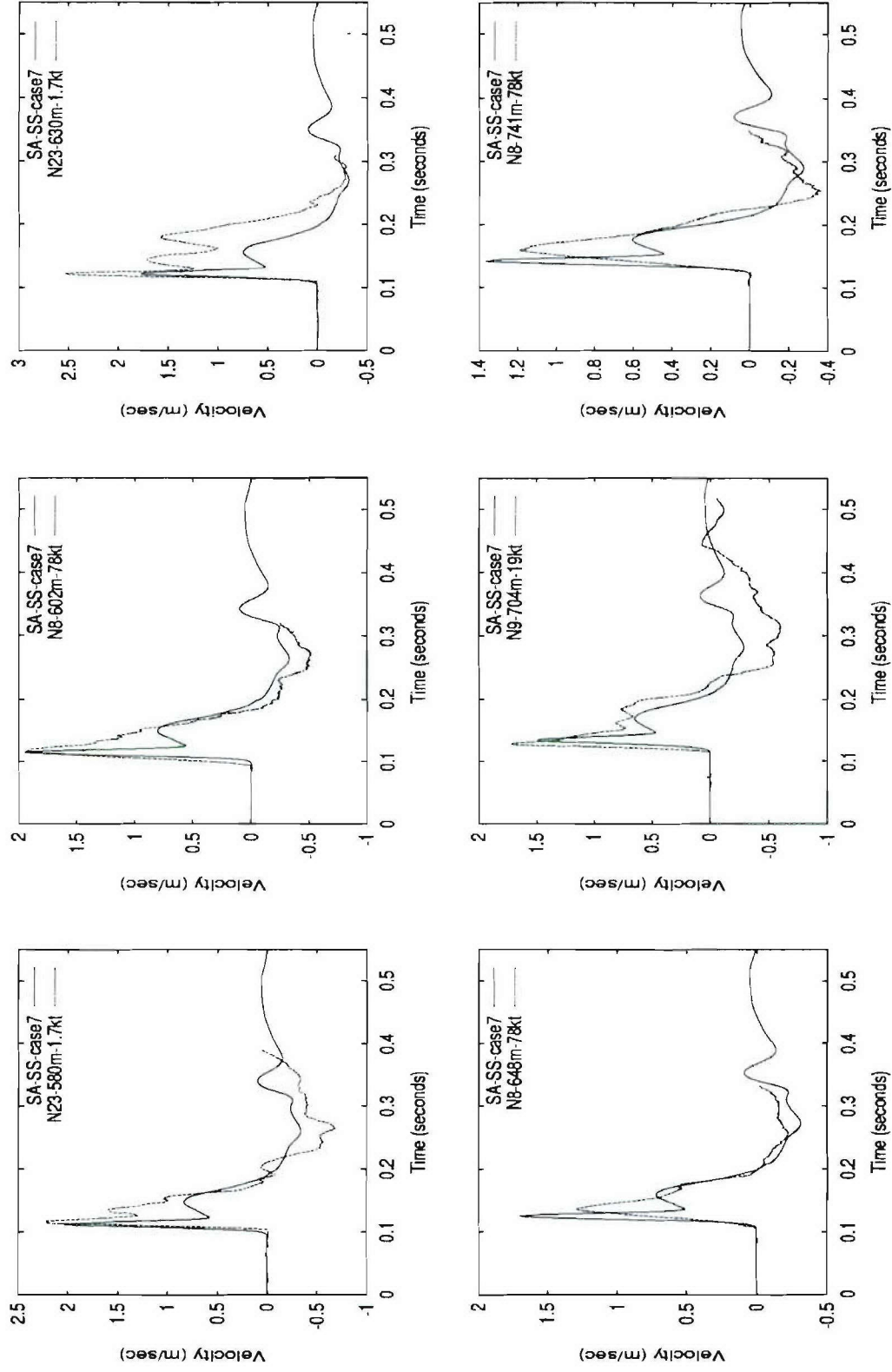


Figure 29. Continued.



**Figure 30.** Comparison between particle velocity pulses at the larger scaled ranges from the wide pulse Degelen data subset and the results of the best fit simulation (case 7) using the SA-SS model combination (the solid curves).

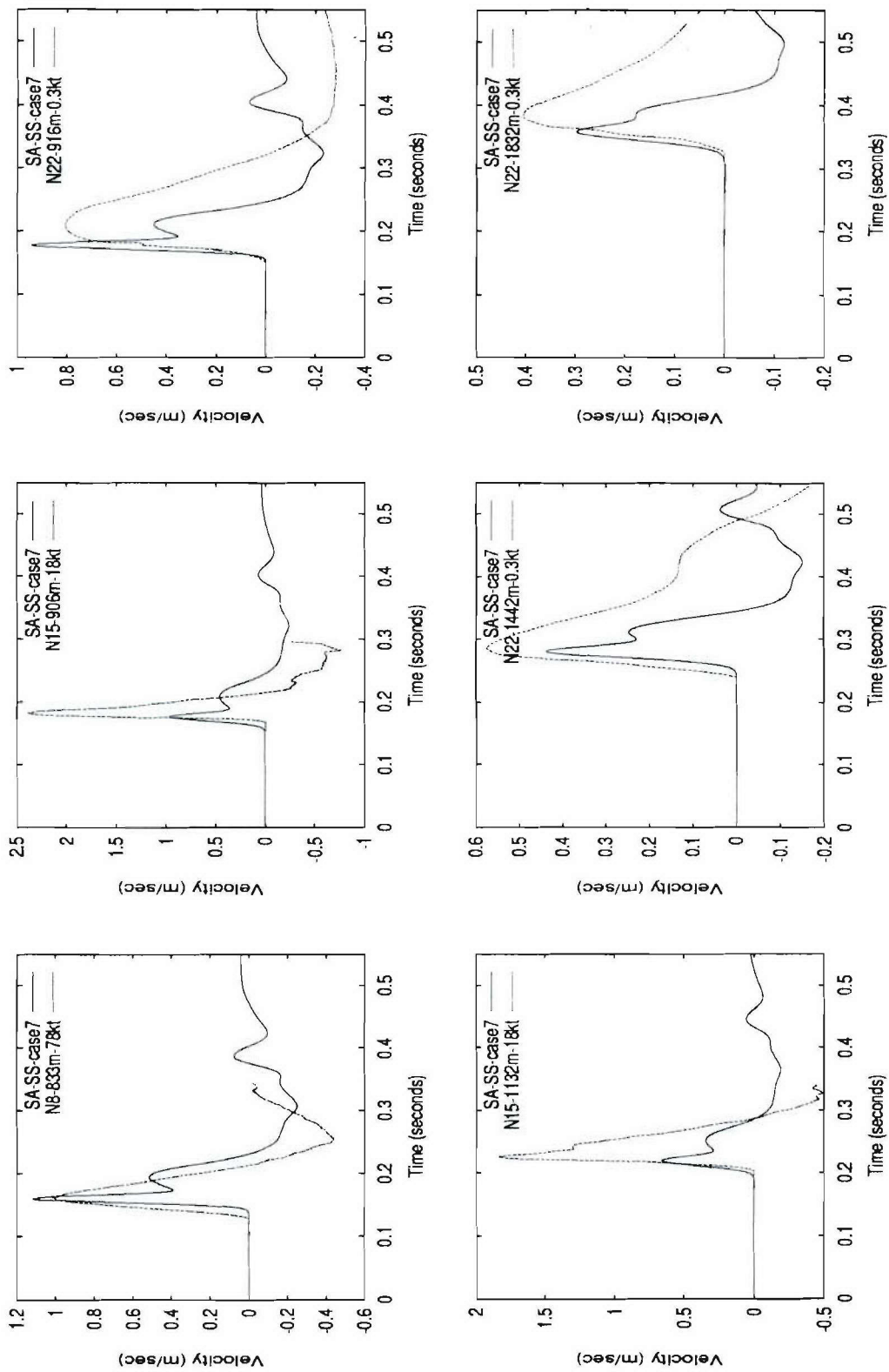


Figure 30. Continued.

## 4.2 Degelen Results for YF-SS Model Combination

Table 11 shows the results of a subset of the parametric variations made using the YF-SS model combination to simulate the wide pulse Degelen data. All of the Degelen simulations with the YF failure model (both YF-SS and YF-AF) used  $\text{epw} = 5000 \text{ ergs/cm}^3$ , a factor of 10 larger than required for the best fits for PILEDRIIVER using these two model combinations. This larger plastic work required for rubblization resulted in a smaller damaged region than for PILEDRIIVER, in better agreement with the Degelen observations of Table 8. All of these Degelen simulations also used the shear-strain dependent shear modulus reduction model with shear strain parameters  $\text{epinit}$  and  $\text{epfull}$  fixed at 0.001 and 0.06, respectively. (Parametric variations in these strains were investigated during the PILEDRIIVER simulations.) For the results shown here in Table 11, most of the parameters of the SS strength reduction model such as  $\text{bsfull}$ ,  $\text{deinit}$ , and  $\text{defull}$ , were also fixed as 0.2, 0.001, and 0.06 respectively. Thus, Table 11 investigates only the effects of variations in the total amount of shear modulus reduction and, in one case, of variation in the friction slope.

**Table 11.** Results for Degelen wide pulse simulations using the YF-SS model combination.

Case #	Model		Results				
	Gdam (kb)	bsl	RDP ( $10^3 \text{ m}^3$ )	Failure (m)	Rmax (m)	Rc (m)	Reduced P-vel. (m/s)
6	200	0.528	10.7	176	33.5	33.2	4984
7A	150	0.428	11.9	196	37.1	34.9	4720
8A	150	0.528	10.5	157	32.5	32.0	4734
9*	50	0.528	9.9	168	33.1	32.1	4175
10	20	0.528	9.9	225	35.5	34.4	3962
11	5	0.528	8.5	153	32.5	30.2	3911

Figures 31 and 32 show comparisons between simulated and measured particle velocity pulses from the best fit (case 9) simulation of the wide pulse subset with the YF-SS model combination. As indicated by the comparisons between the results with different model combinations in Table 9, this simulation is our third best overall, behind our best results with the SA-SS and YF-AF combinations.

## 4.3 Degelen Results for YF-AF Model Combination

Table 12 shows the results of some of the parametric variations made using the YF-AF model combination to simulate the wide pulse Degelen data. Here, the parametric variations investigate both the effects of the total amount of shear modulus reduction and of parameters of the AF strength reduction model. Case 2, for no AF strength reduction, will be shown later as our best fit to the narrow pulse Degelen data. Note that the PILEDRIIVER simulations with this model combination used a very slow time decay of acoustic fluidization ( $\tau = 10 \text{ sec}$ ). The best Degelen simulations with this model allowed the AF strength reduction to decay more rapidly.



**Table 12.** Results for Degelen wide pulse simulations using the YF-AF model combination.

Case #	Model Parameters				Results				
	Gdam (kb)	cvib	kvis (cm <sup>2</sup> /s)	tau (s)	RDP (10 <sup>3</sup> m <sup>3</sup> )	Failure (m)	Rmax (m)	Rc (m)	Reduced P-vel. (m/s)
1	30	1e4	1e2	1e-3	11.7	208	36.4	35.3	4018
2	30	0	0		6.1	200	30.0	29.6	4122
3	30	1e2	1e2	1e-3	9.3	221	33.6	32.8	4035
4	30	1e1	1e2	1e-3	8.0	183	31.8	31.1	4078
5	20	1	1e1	1e-3	6.8	183	30.6	29.9	4046
6	20	1e-1	1e1	1e-1	11.6	225	38.0	35.9	3949
7*	20	1e-1	1e1	5e-2	10.4	196	35.0	33.8	3967
8	30	1e-1	1e1	5e-2	10.2	172	33.6	32.5	4048

Comparisons between simulated and measured particle velocities from case 7 of Table 12, our best fit to the wide pulse Degelen data with the YF-AF model combination, are shown in Figures 33 and 34. The comparisons of Table 9 indicate that case 7 is our second best overall simulation of these data. Direct comparisons with Figures 29 and 30, the best overall fit (with the SA-SS models) show that the two model combinations provide equally good simulations of the Degelen positive velocity pulses. In fact, the results with the SA-SS models provide a better simulation of those positive pulses that show a second distinct velocity peak, while the results with the YF-AF models provide a better simulation of those positive pulses that do not show this second peak. The YF-AF model results also give smaller failure extents, in better agreement with the Degelen observations of Table 8, but do not give as good a match to the observed P-wave velocity reductions near the cavity as do the best fit SA-SS results. Moreover, the negative velocity pulses shown in Figures 33 and 34 are clearly a worse match to the measurements than are the negative pulses shown in Figures 29 and 30.

#### 4.4 Degelen Results for SA-AF Model Combination

Table 13 shows the results of some of the parametric variations made using the SA-AF model combination to simulate the wide pulse Degelen data. The parameters of the Sammis brittle failure model, with one exception, were fixed at their values given earlier for the SA-SS best fit Degelen simulation. Here, Gslp, the slope of the shear modulus reduction vs. damage parameter relation, was fixed at 200 kb, rather than the 300 kb used for the SA-SS model. Thus, Table 13 looks at the effects of variations in the AF strength reduction model parameters. Case 4 of this table corresponds to no AF strength reduction.

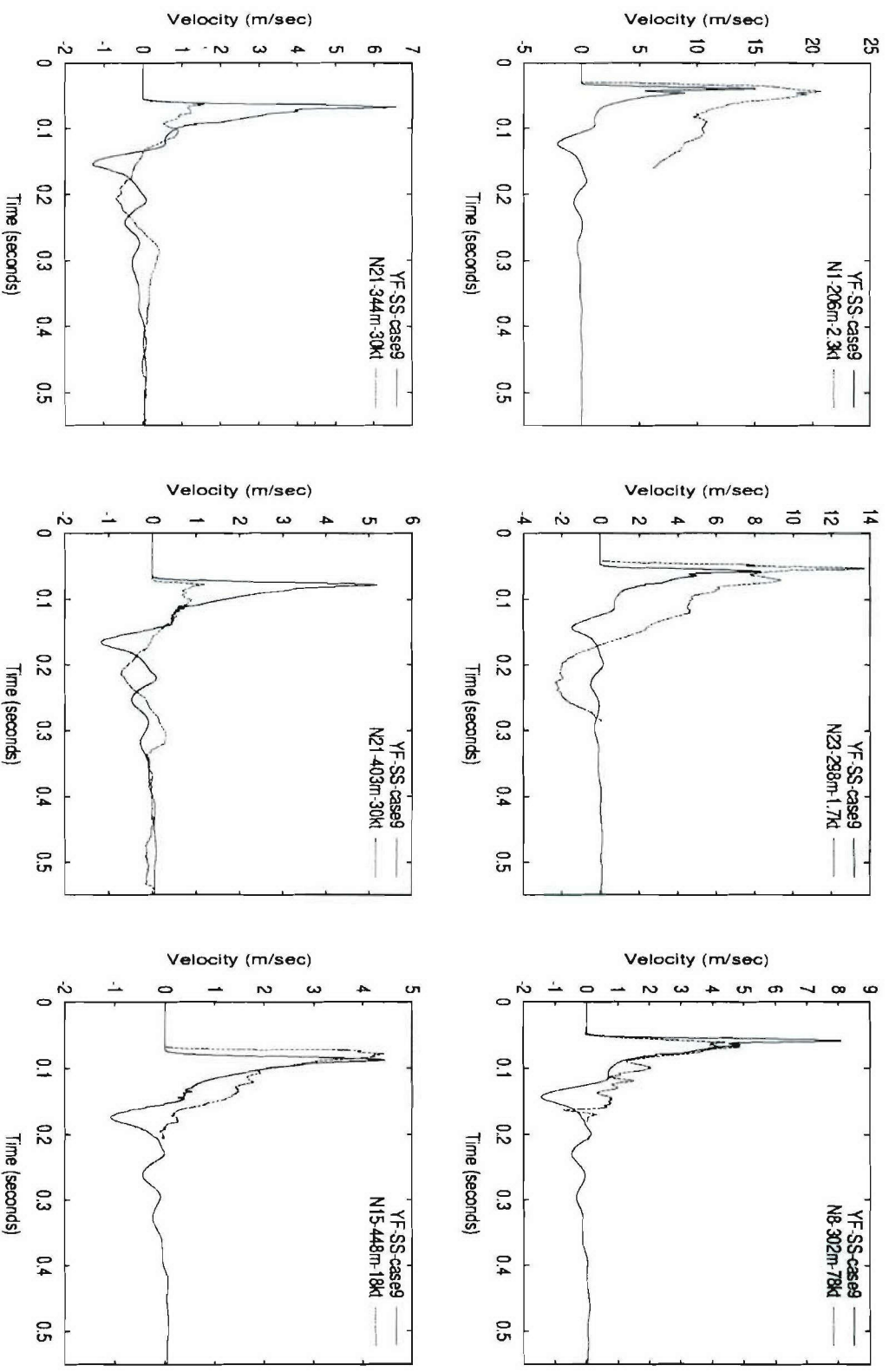


**Figure 31.** Comparison between particle velocity pulses at the smaller scaled ranges from the wide pulse Degelen data subset and the results of the best fit simulation (case 9) using the YF-SS model combination (the solid curves).

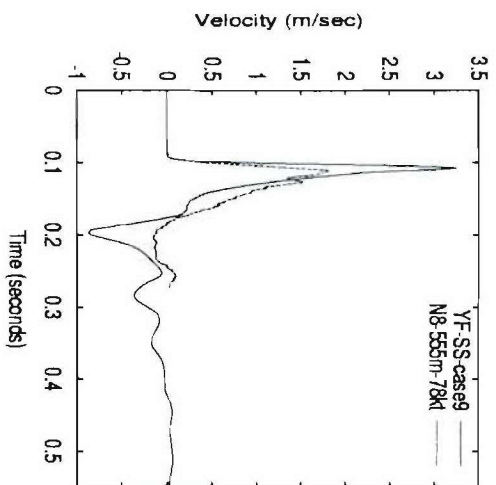
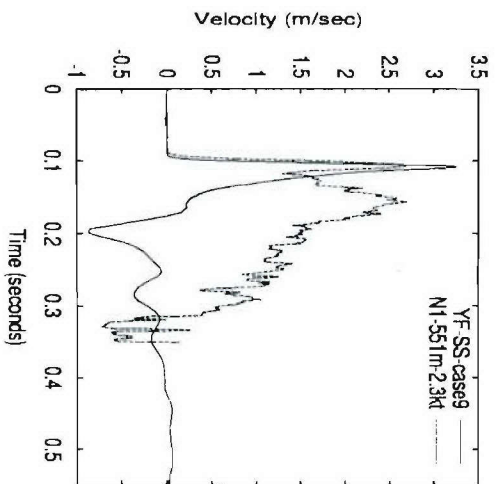
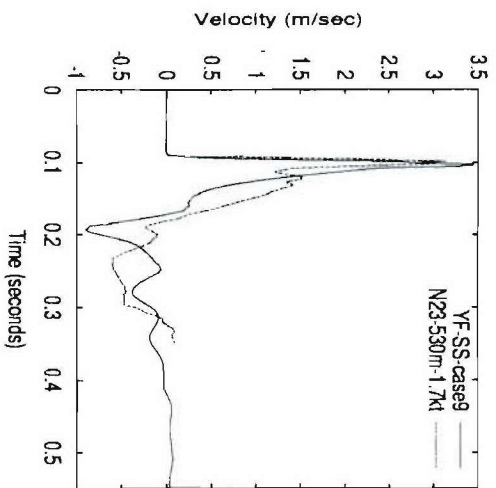
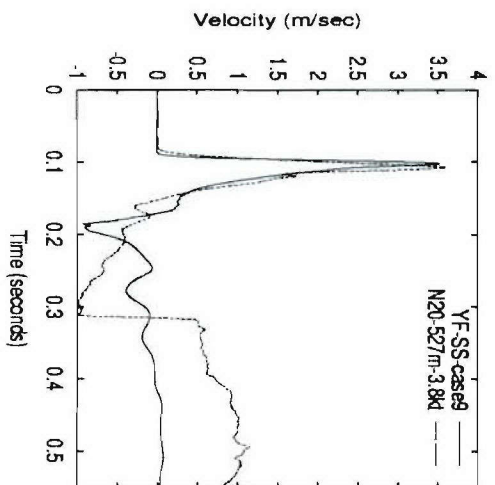
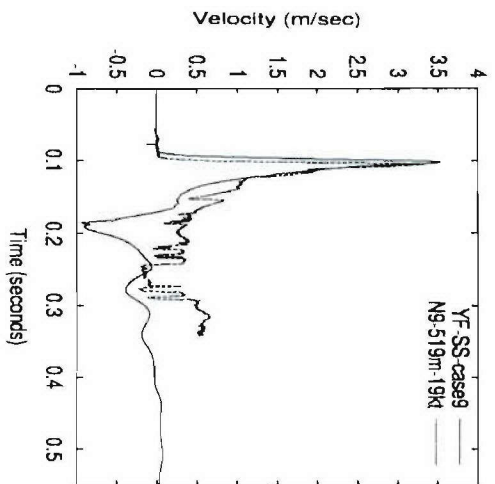
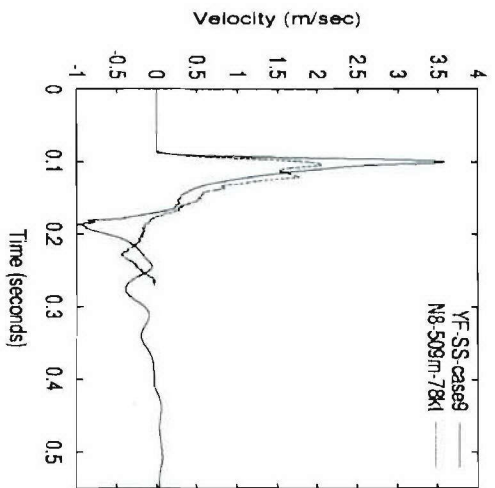
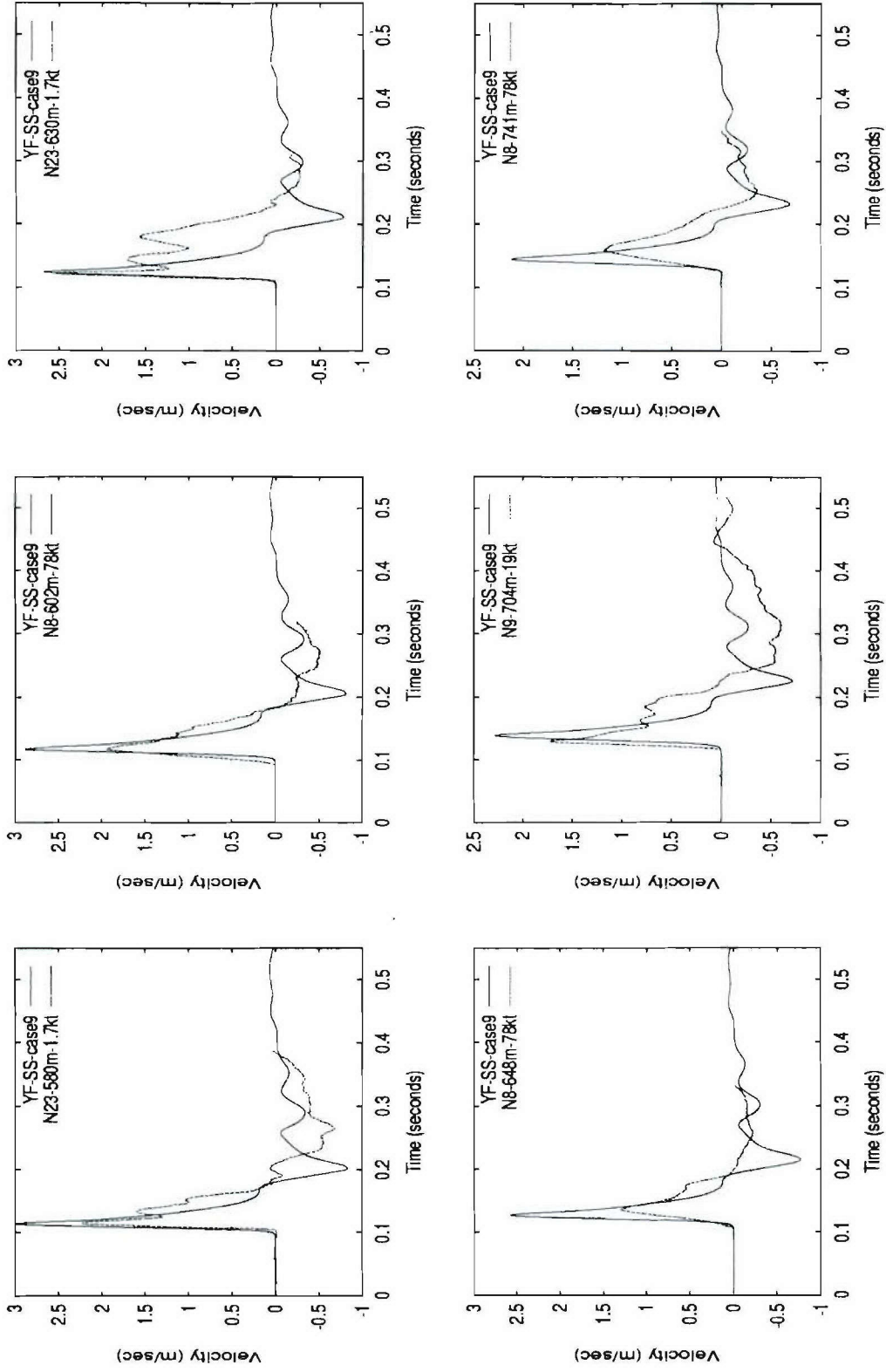


Figure 31. Continued.



**Figure 32.** Comparison between particle velocity pulses at the larger scaled ranges from the wide pulse Degelen data subset and the results of the best fit simulation (case 9) using the YF-SS model combination (the solid curves).



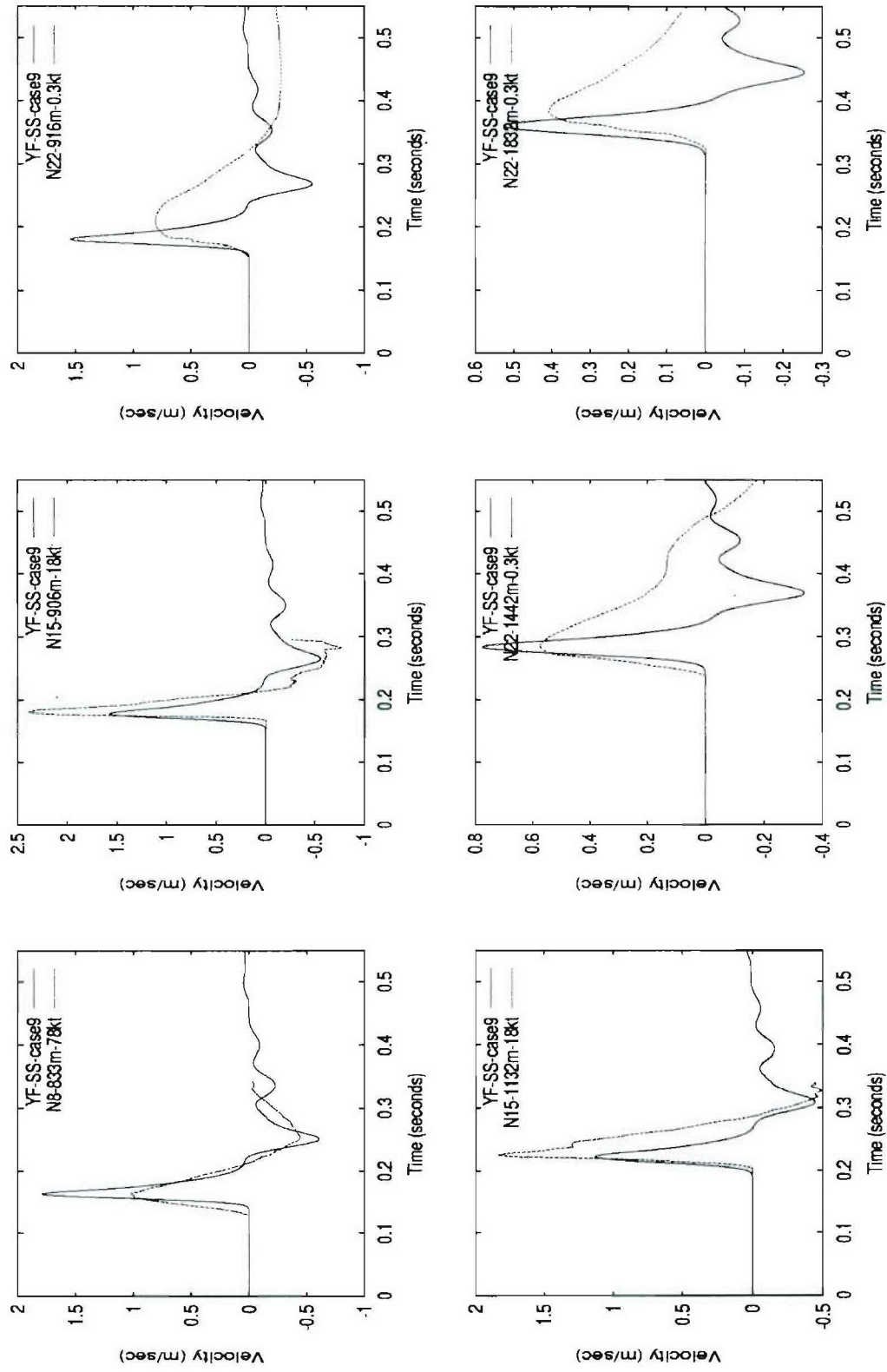
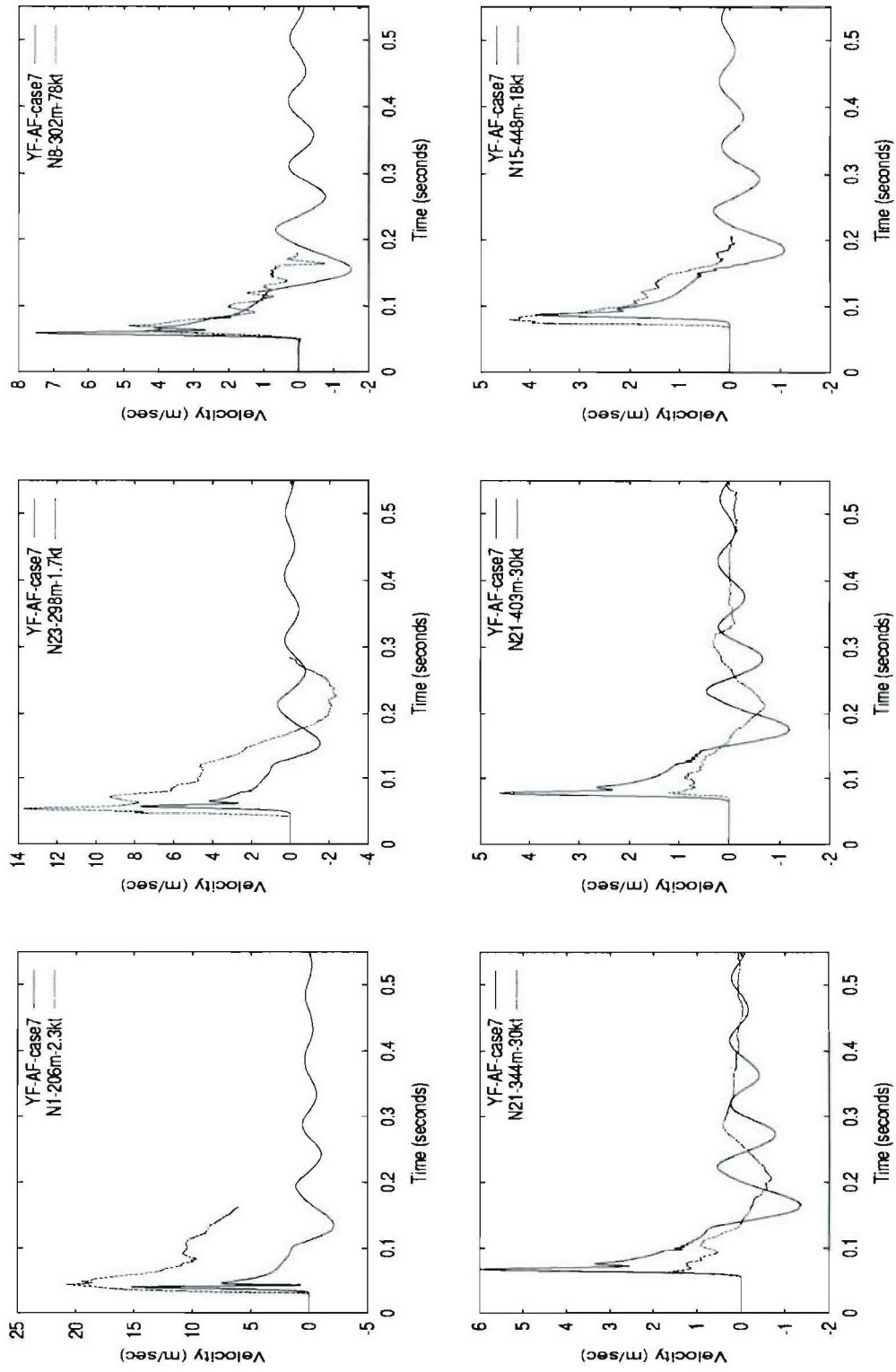


Figure 32. Continued.

**Table 13.** Results for Degelen wide pulse simulations using the SA-AF model combination.

Case #	AF Model			Results				
	cvib	kvis (cm <sup>2</sup> /s )	tau (s)	RDP (10 <sup>3</sup> m <sup>3</sup> )	Failure (m)	Rmax (m)	Rc (m)	Reduced P-vel. (m/s)
1	1e-2	1e2	1e-1	6.15	257	29.9	29.8	4010
2	1e-1	1e2	1e-1	9.8	281	36.0	35.8	4017
3*	5e-2	1e2	1e-1	7.7	266	32.7	32.6	4013
4	0	0		5.7	257	29.1	29.0	4009
5	5e-2	1e2	1e-3	5.8	257	29.4	29.3	4013
6	5e-2	1e2	1e-2	5.9	266	29.4	29.3	4014

Figures 35 and 36 shows comparisons between simulated and measured particle velocity pulses from the best fit (case 3) simulation of the wide pulse Degelen subset with the SA-AF model combination. This simulation is not as good a match to the data as the best fits for the other model combinations, primarily because of lower calculated peak velocities and more noisy signals at the smaller scaled ranges. The fourth place overall SA-AF results does give negative pulses that are superior on average to all but the first place overall best fit with the SA-SS model combination shown in Figures 29 and 30. Positive pulses in Figures 35 and 36 are also narrower than the data, but may be widened by increasing  $G_{slp}$ , thus also giving a smaller cavity radius and a larger RDP than shown in Table 13.



**Figure 33.** Comparison between particle velocity pulses at the smaller scaled ranges from the wide pulse Degelen data subset and the results of the best fit simulation (case 7) using the YF-AF model combination (the solid curves).

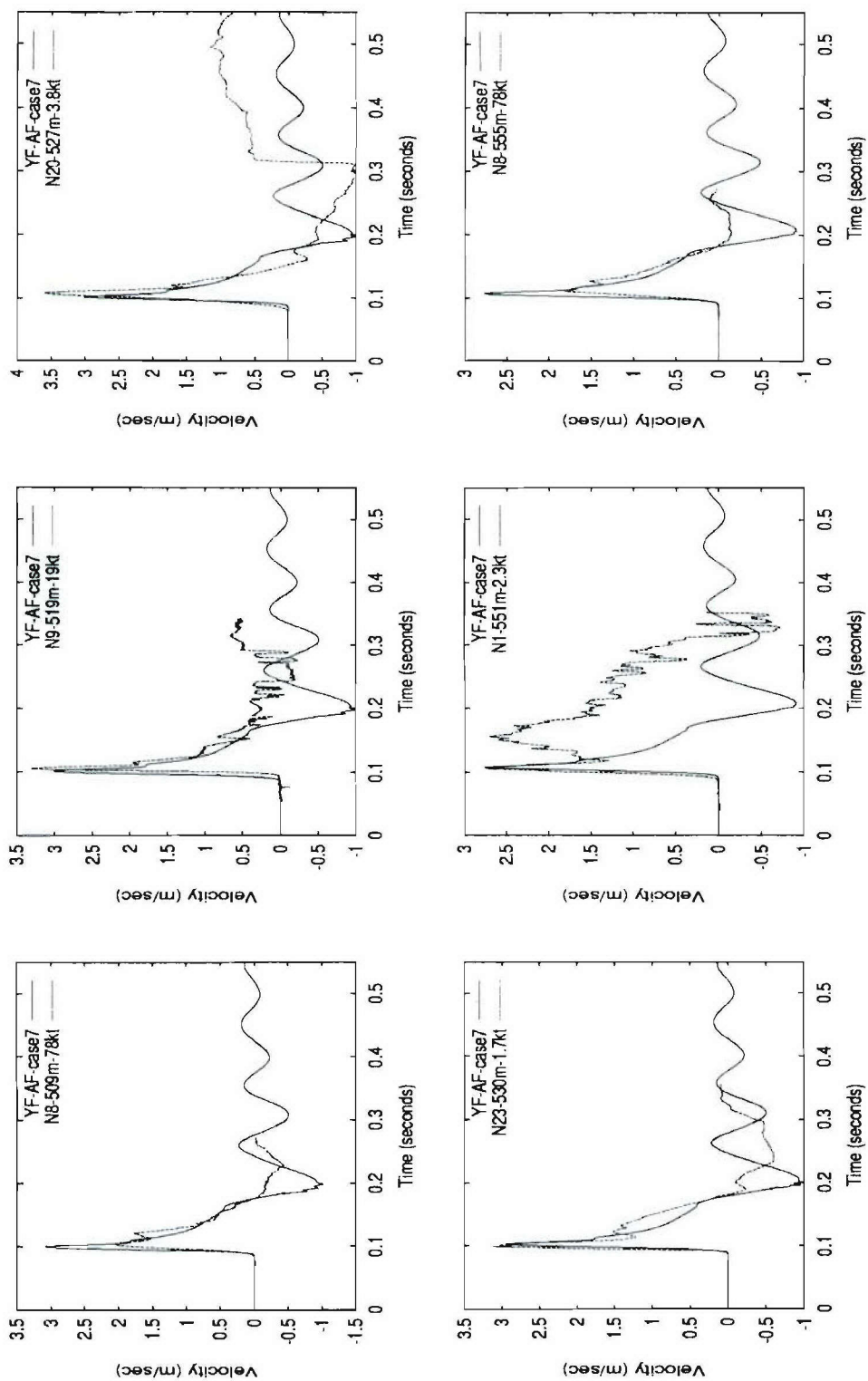
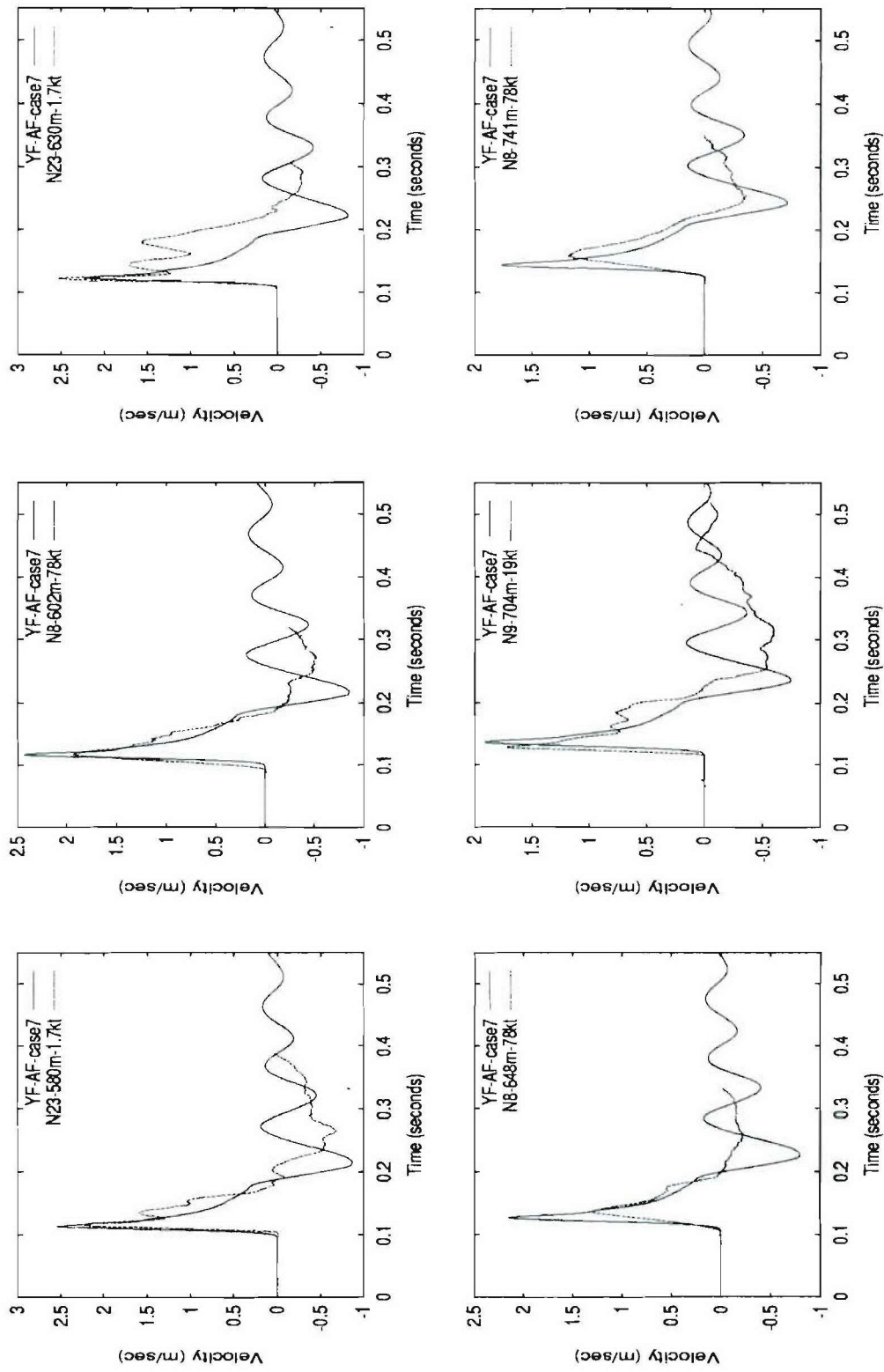


Figure 33. Continued.





**Figure 34.** Comparison between particle velocity pulses at the larger scaled ranges from the wide pulse Degelen data subset and the results of the best fit simulation (case 7) using the YF-AF model combination (the solid curves).

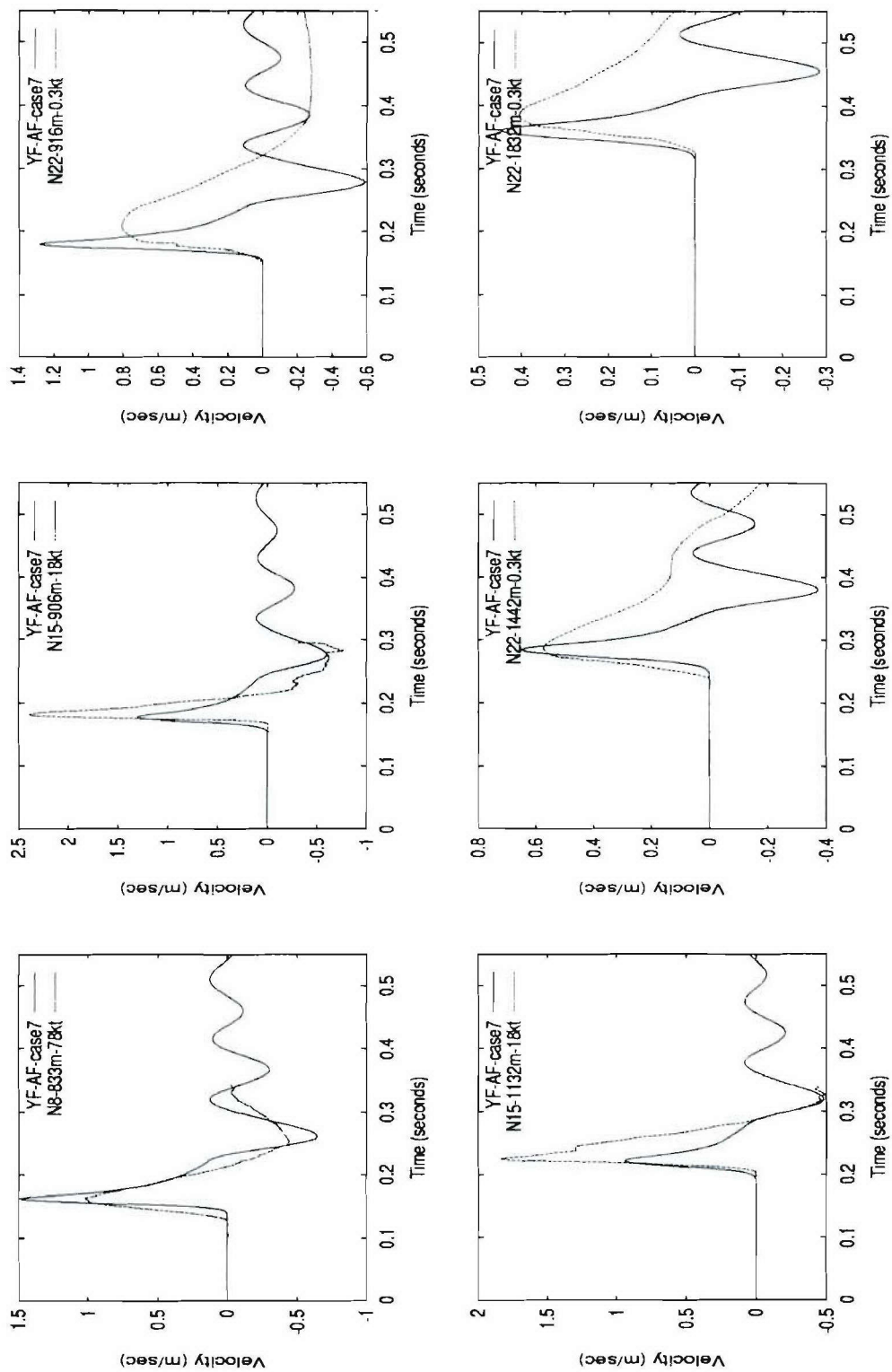
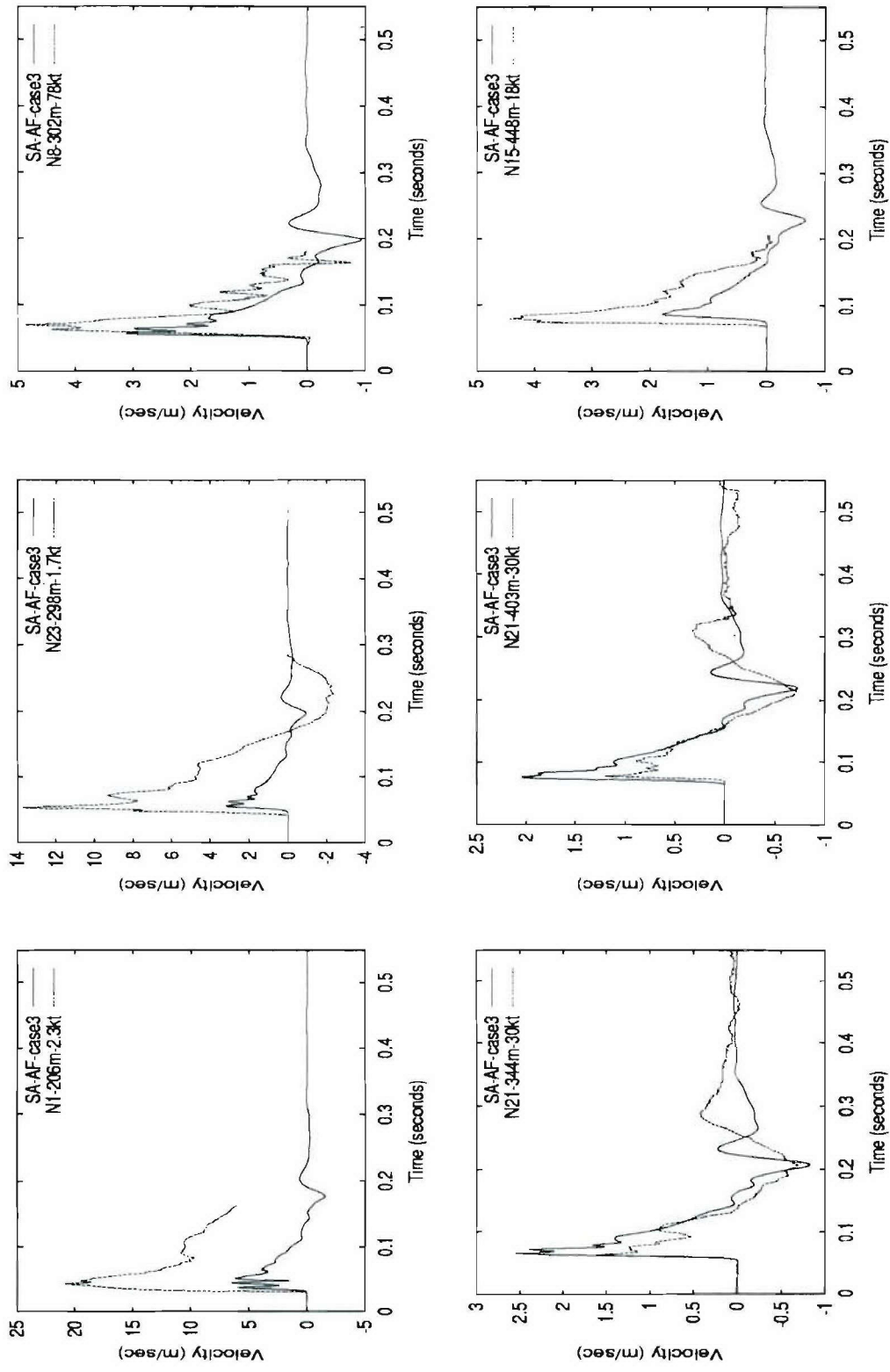


Figure 34. Continued.



**Figure 35.** Comparison between particle velocity pulses at the smaller scaled ranges from the wide pulse Degelen data subset and the results of the best fit simulation (case 3) using the SA-AF model combination (the solid curves).

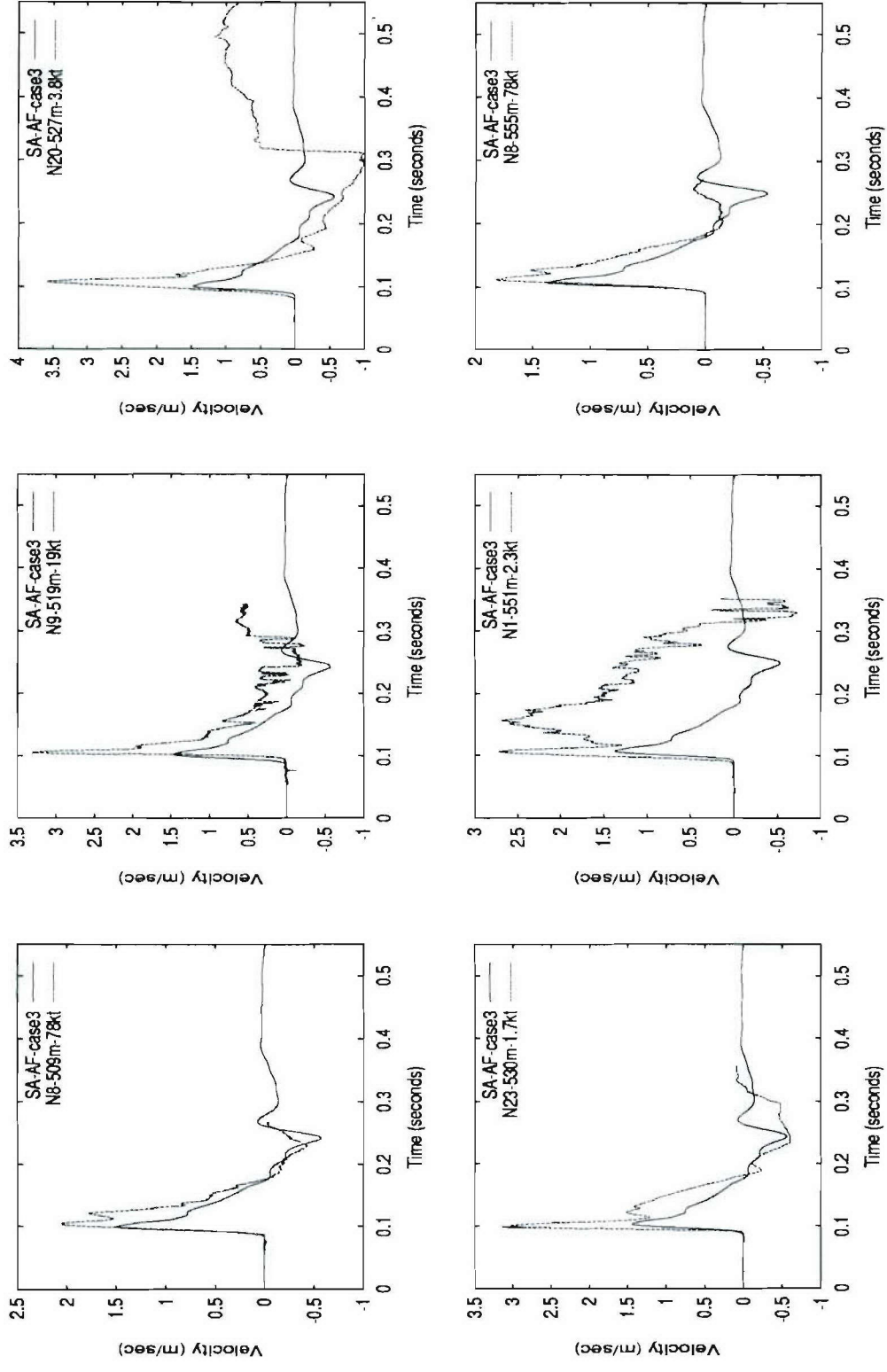
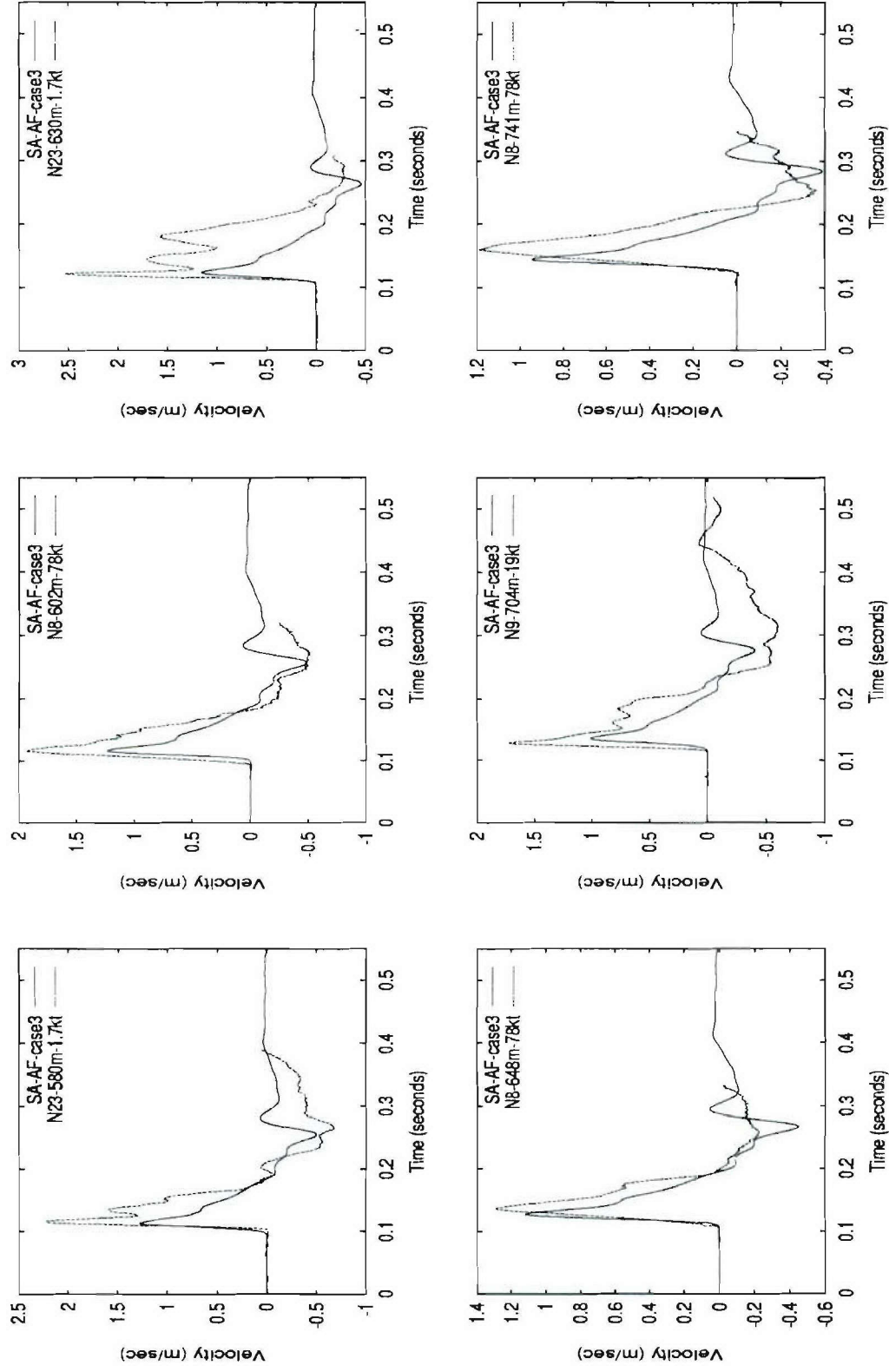


Figure 35. Continued.





**Figure 36.** Comparison between particle velocity pulses at the larger scaled ranges from the wide pulse Degelen data subset and the results of the best fit simulation (case 3) using the SA-AF model combination (the solid curves).

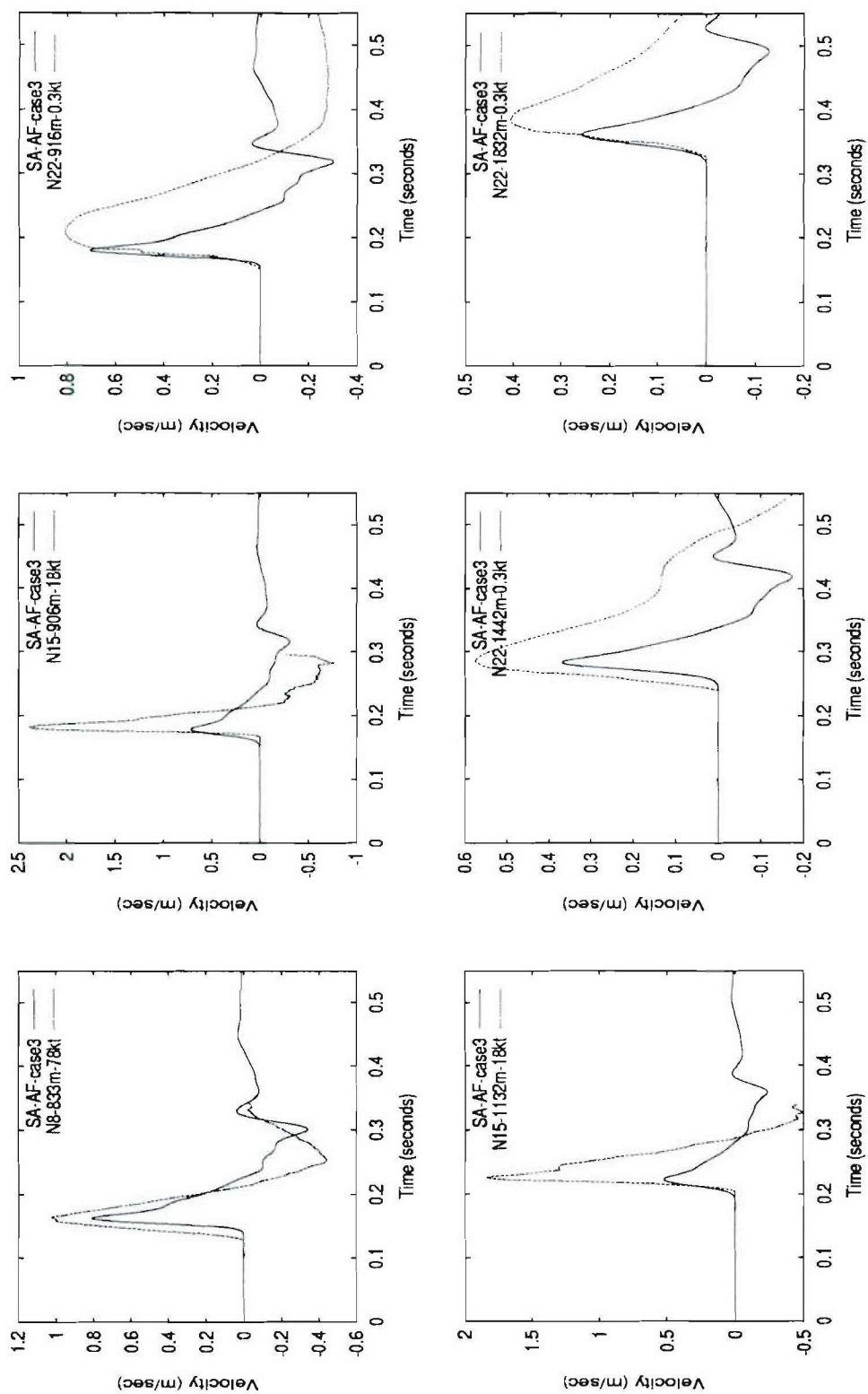


Figure 36. Continued.

## 4.5 Narrow Pulse Degelen Simulations

Our calculations of the 3 narrow pulse explosions show that the best fits to the particle velocity pulses with our chosen model combinations are obtained using the YF-AF model with acoustic fluidization turned off (Case 2 of Table 12). Figure 37 shows comparisons between the results of Case 2 and the particle velocity measurements from these three explosions. On average, the simulation is in good agreement with the measured positive pulses. The simulated negative pulses are also in good agreement with the amplitude and time duration of the data (for those measurements that show a well-defined negative pulse. However, the simulated negative peaks seem to occur roughly 0.05 seconds after the measured peaks. We have found that most of this time delay can be eliminated if we remove the post-failure friction law from the YF failure model.

The Case 2 simulation also gave a small cavity radius of 29.6 m, a failure extent of 200 m, a static RDP of  $6,100 \text{ m}^3$ , and a peak RDP of about  $7500 \text{ m}^3$ . This computed peak RDP is roughly the same as the peak RDPs, shown in Table 2 of Section 2, that were obtained from the particle velocity measurements from narrow pulse explosions.

### 4.5.1 Results for Different Depths of Burial

All of the Degelen simulations discussed in Section 4 so far have been made using an overburden pressure, povb, of 50 bars, corresponding to a depth of roughly 200 m, and considerably less than the approximately 120 bar lithostatic stress at the PILEDRIIVER depth of burial. Table 2 of Section 2 shows the depths of burial of the Degelen explosions, which vary from 112 m (~29 bars) for the shallowest buried, 1.7 kt, event down to 343 m (~87 bars) for the deepest, 125 kt, event. Tables 14 and 15 show the results of repeating, for overburden pressures of 30 and 90 bars, our best fit simulations of both the wide pulse and narrow pulse explosions using the YF-AF model combination. Use of the larger overburden pressures consistent with the larger depths of burial, as would be expected, reduce the amplitudes of the simulated RDPs. However, the particle velocity waveforms are changed only slightly.

**Table 14.** Results of overburden variations for Degelen wide pulse simulations using the YF-AF model combination.

Case #	povb (bars)	Gdam (kb)	RDP ( $10^3 \text{ m}^3$ )	Failure (m)	Rmax (m)	R (m)	Reduced P-vel (m/s)
7A	30	20	12.5	180	34.2	33.1	3976
7*	50	20	10.4	196	35.0	33.8	3967
7B	90	20	8.32	191	34.3	33.2	3975

**Table 15.** Results of overburden variations for Degelen narrow pulse simulations using the YF-AF model combination with acoustic fluidization turned off.

Case #	povb (bars)	Gdam (kb)	RDP ( $10^3 \text{ m}^3$ )	Failure (m)	Rmax (m)	R (m)	Reduced P-vel (m/s)
2A	30	30	7.3	221	30.9	30.6	4100
2*	50	30	6.1	200	30.0	29.6	4122
2B	90	30	4.9	208	29.7	29.3	4129

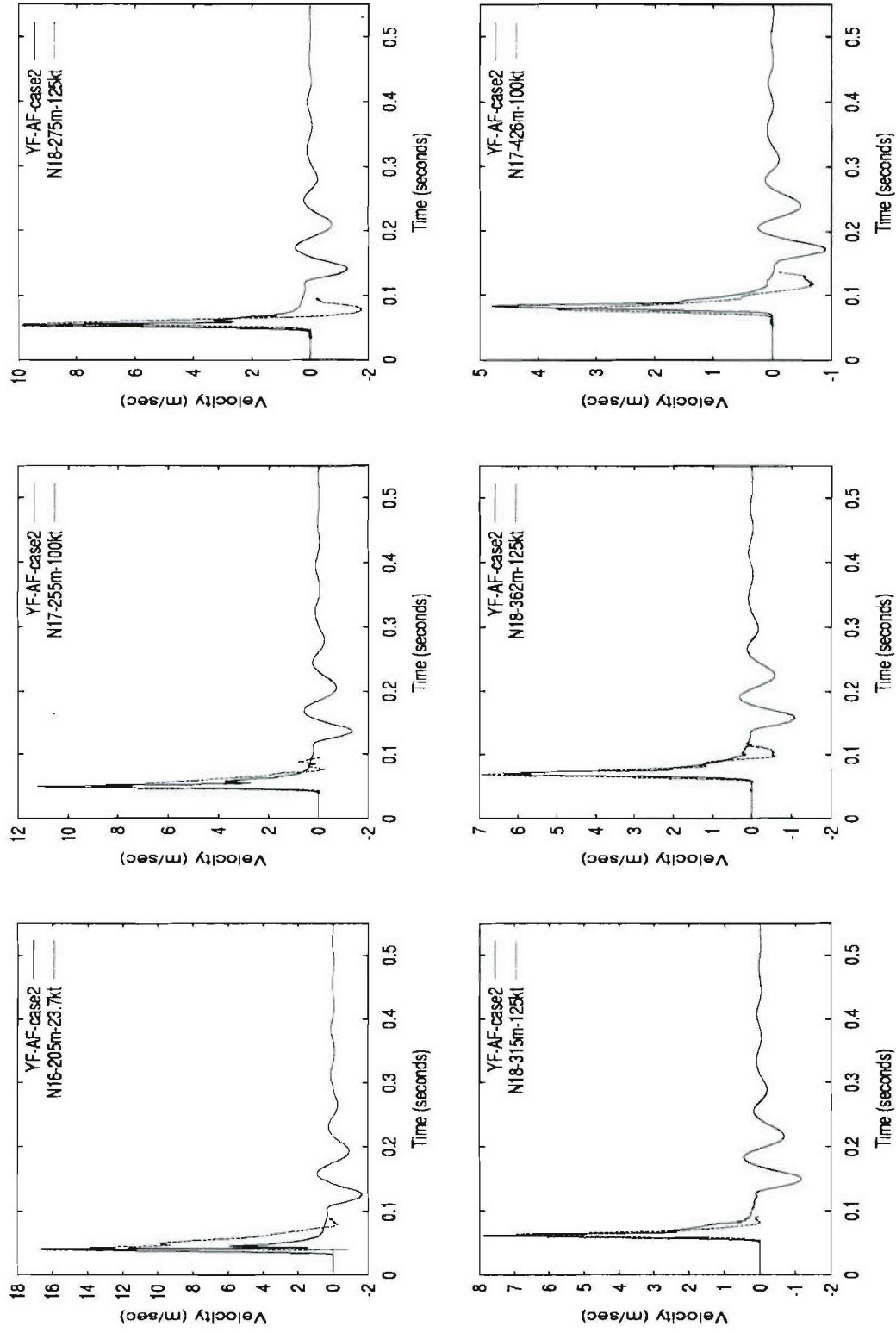


**Figure 37.** Comparison between particle velocity pulses from the narrow pulse Degelen data subset and the results of the best fit simulation (case 2 of Table 12) using the YF-AF model combination with acoustic fluidization turned off (the solid curves).



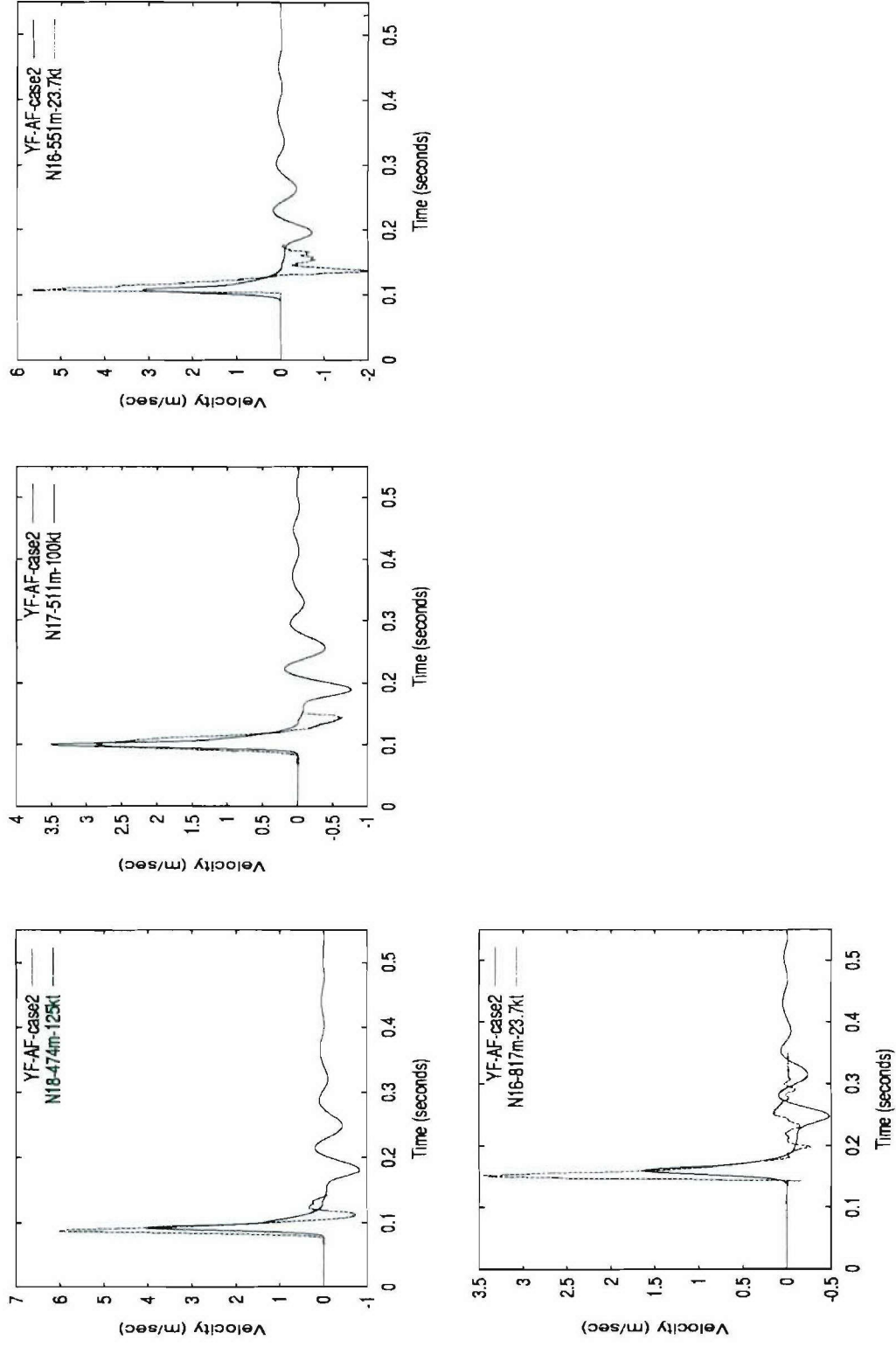
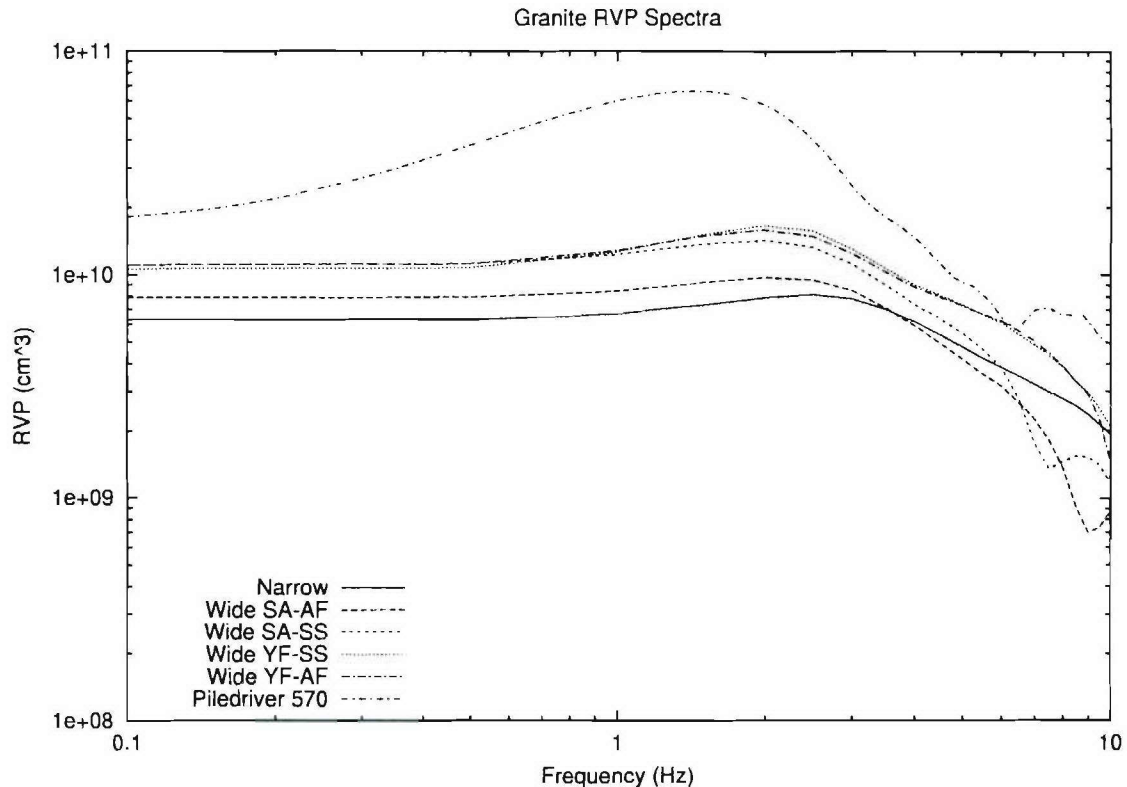


Figure 37. Continued.

#### 4.5.2 Seismic Source Functions for Degelen Models

Figure 38 shows the calculated explosion seismic source spectra (RVP) for the four best fit wide pulse models, the best narrow pulse model and for PILEDRIIVER 570. The narrow pulse source function is lower in amplitude at low frequencies than the wide pulse data, but only by about a factor of 2, and the difference decreases with increasing frequency. Strength weakening is a much stronger effect in US granite, causing the difference in source functions between the Degelen models and US granite to be much more dramatic.



**Figure 38.** Calculated source spectra (reduced velocity potential) for explosions in Degelen granite using four combinations of nonlinear models, and a calculated source spectrum for the US explosion Piledriver (evaluated at 62 KT).

Figure 38 implies that seismic waves from narrow-pulse explosions at Degelen should be smaller than seismic waves from the wide-pulse explosions. We saw earlier in Figures 20 and 21 that near regional amplitudes appear to be slightly smaller as predicted, although not definitively so, and that the far field body waves from the narrow pulse events are close to the same amplitude or slightly larger than the body waves from narrow-pulse events. One possible explanation for this anomaly is that the near field data, which are recorded at shot level, may be more affected by cracks and joints than the downgoing waves which control the far field body waves. This suggests the possibility that the explosion source function for regional phases, which have a shallower takeoff angle, may be significantly different from the explosion source function for teleseismic body waves.

## SECTION 5 CONCLUSIONS AND RECOMMENDATIONS

IDG has digitized data from 23 nuclear explosions at the Degelen test site. The complete data set consists of 77 near field waveforms recorded underground at shot depth and 115 (unique) near regional seismic records (or 283 seismic records, including multiple records of the same signal). The data set of near field and regional waveforms will be delivered DTRA and to the Center for Monitoring Research upon completion of this project.

Work at SAIC has focused both on analyses of this data set and on the development of material models that are consistent with these data and have a realistic physical basis. Some important results of our data analyses and modeling follow.

### Data Analyses:

- Near field particle velocity data from five of the lower yield Degelen explosions (yields of 0.5, 1.1, 1.4, 1.8, and 2.2 kt) had shapes more like block motion than free-field ground motion. These explosions were excluded from our analyses.
- To more easily compare these data, we scaled all of the Degelen and NTS near field data to the same yield (the PILEDRIVER yield of 62 kt). The data was then organized based on yield-scaled pulse widths and pulse shapes. Three of the higher yield Degelen explosions (the “narrow pulse” subset with yields of 23.7, 100, and 125 kt) gave scaled pulse widths that were much narrower than the other free-field Degelen events.
- The other free-field “wide pulse” Degelen explosions, including 5 higher yield events (18, 19, 30, and 78 kt) and 4 lower yield events (below 10 kt), cover a large range of scaled pulse widths and peak amplitudes. All but one of these events (a 0.3 kt event) have scaled pulse widths much narrower than PILEDRIVER, but all are much wider than the narrow pulse subset.
- Our analyses of regional waveforms and body wave magnitudes show that both the near regional data and body wave magnitudes are consistent with a single magnitude yield relation that does not clearly reflect the observed differences in near field waveforms. A possible explanation for this anomaly is that the near field data, which are recorded at shot level, may be more affected by cracks and joints than the downgoing waves which control the far field body waves.

### Modeling:

- We have modeled the near field data from the NTS and Degelen explosions using two failure/rubblization mechanisms, the Sammis brittle failure damage mechanics model and a plastic failure model, and three strength reduction mechanisms, an effective stress model, a shear-strain-based shock damage model, and an acoustic fluidization model.

- For the NTS and Degelen wide pulse data, the simulated waveforms resulting from different combinations of failure/rubblization model plus strength reduction model are all somewhat different, but provide reasonable fits overall to the measurements.
- The differences in data fit from these simulations are not sufficient to conclusively determine the failure and weakening mechanisms.
- For a given model, the best fits to the NTS waveforms are accomplished using different material parameters than are used for the best fits to the wide pulse Degelen waveforms.
- Particle velocity waveforms from the Degelen narrow pulse explosion subset can be simulated without using any strength reduction model.
- The simulations of both the wide and narrow pulse subsets with these models showed the effect of depth of burial (lithostatic stress) on waveforms to be insignificant.

In conclusion, the Degelen data set provided by IDG has clearly shown the difficulty in predicting near-field ground motions from an underground explosion at a hard rock site that has not been well characterized pre-shot. Even though IDG had provided some pre-shot and post-shot material properties data for several explosions, such as P-wave velocities, unconfined compressive strength, and fracture density, no correlation could be found between the limited material properties data provided for these explosions and the variability in measured free-field waveforms.

We recommend that an effort be made to quantify the effects on pulse widths and peak displacements resulting from changes in Degelen site conditions due to earlier nearby explosions. With the assistance of IDG, a three-dimensional mapping of explosion working points at the Degelen test site could be used to determine the location and timing of earlier explosions near the sites for which we already have near-field particle velocity waveforms. Together with estimates of explosion-driven ground motions obtained from the numerical models which best fit the data, we should be able to find any correlation between the measured free-field waveforms and damage to the site from the stresses and displacements from the earlier explosions.

#### 5.1.1.1



## SECTION 6 REFERENCES

- Ashby, M.F. and C.G. Sammis (1990), "The Damage Mechanics of Brittle Solids in Compression," *PAGEOPH*, Vol. 133, No. 3. (Unclassified)
- Bocharov, V. S., S. A. Zelentsov, and V. N. Mikhailov (1989), "Characteristics of 96 Underground Nuclear Explosions at the Semipalatinsk Test Site (in Russian)," *Soviet Atomic Energy (Atomnaya Energiya)*, 67, 210-214, September. (Unclassified)
- Day, S. M., N. Rimer and J. T. Cherry (1983), "Surface Waves from Underground Explosions with Spall: Analysis of Elastic and Nonlinear Source Models," *Bull. Seism. Soc. Am.*, 73, pp. 247-264. (Unclassified)
- Luco, J. E. and R. J. Apsel (1983), "On the Green's Functions for a Layered Half-Space. Part 1.," *Bull. Seism. Soc. Am.*, 73, 909-929. (Unclassified)
- Melosh, H. J. (1979), "Acoustic Fluidization: A New Geologic Process?," *J. Geophys. Res.*, 84, 7513, December. (Unclassified)
- Melosh, H. J., and B. A. Ivanov (1999), "Impact Crater Collapse," *Annual Rev. Earth Planet Science*, 27, pp385-415. (Unclassified)
- Murphy, J. R. (1977), "Seismic Coupling and Magnitude/Yield Relations for Underground Nuclear Detonations in Salt, Granite, Tuff/Rhyolite, and Shale Emplacement Media," Computer Sciences Corporation Technical Report CSC-TR-77-0004, December. (Unclassified)
- Murphy, J. R. (1978), "A Review of Available Free-Field Seismic Data from Underground Nuclear Explosions in Salt and Granite," Computer Sciences Corporation Technical Report CSC-TR-78-0003, March. (Unclassified)
- Rimer, N. and K. Lie (1982), "Numerical Simulation of the Velocity Records from the SRI Grout Spheres Experiments," S-CUBED Topical Report DNA-TR-82-54, September. (Unclassified)
- Rimer, N., S. M. Day, G. A. Hegemier, H. E. Read, S. K. Garg, and S. Peyton (1984), "Effect of Pore Fluid Pressure on Explosive Ground Motions in Low Porosity Brittle Rocks," S-CUBED Final Report DNA-TR-85-245, July. (Unclassified)
- Rimer, N., J. L. Stevens, and K. H. Lie (1986), "Effects of Pore Pressure and Fractures on Ground Motion in Granite," S-CUBED Final Report DNA-TR-86-227, June. (Unclassified)
- Rimer, N., J. L. Stevens, and S.M. Day (1987), "Effects of Pore Pressure, Fractures, and Dilatancy on Ground Motion in Granite," S-CUBED Final Report AFGL-TR-87-0136, April. (Unclassified)

- Rimer, N. and W. Proffer (1991), "Containment Phenomenology Using a New Shear-Strain-Based Computational Damage Model for Tuff," S-CUBED Technical Report SSS-DTR-91-12612, September, also SSS-DTR-90-11961, October. (Unclassified)
- Rimer, N., K. Lie, J.L. Stevens, J.R. Murphy, and G.G. Kocharyan (1998), "A Micro-Mechanical Damage Model for Estimating Seismic Source Characteristics of Underground Explosions in Hardrock," Maxwell Technologies Technical Report MFD-DTR-98-15985, January. (Unclassified)
- Rimer, N., J.L. Stevens, J.R. Murphy, and G.G. Kocharyan (1999), "Estimating Seismic Source Characteristics of Explosions in Hardrock Using a Micro-Mechanical Damage Model," Maxwell Technologies Final Report MTSD-DTR-99-16423, July. (Unclassified)
- Sammis, C.G. and M.F. Ashby (1988), "The Damage Mechanics of Brittle Solids in Compression," AFGL-TR-88-0160, July. (Unclassified)
- Sammis, C.G. (1991), "A Damage Mechanics Source Model for Underground Nuclear Explosions," PL-TR-91-2103, August. (Unclassified)
- Stevens, J. L. (1986), "Estimation of Scalar Moments from Explosion-Generated Surface Waves," *Bull. Seism. Soc. Am.*, v. 76, pp. 123-151. (Unclassified)
- Stevens, J. L., N. Rimer, and S. M. Day (1986), "Constraints on modeling of underground explosions in granite," S-CUBED annual report to Air Force Geophysics Laboratory, AFGL-TR-86-0264, SSS-R-87-8312, October. (Unclassified)
- Stevens, J. L., T. G. Barker, S. M. Day, K. L. McLaughlin, N. Rimer, and B. Shkoller (1991), "Simulation of teleseismic body waves, regional seismograms, and Rayleigh wave phase shifts using two-dimensional nonlinear models of explosion sources," AGU Geophysical Monograph 65: Explosion Source Phenomenology, S. Taylor, H. Patton, P. Richards, editors, ISBN 0-87590-031-3, pp. 239-252. (Unclassified)
- Stevens, J. L., N. Rimer, H. Xu, G. G. Kocharyan, B. Ivanov, and S. M. Day (2001), "Near field and regional modeling of explosions at the Degelen test site," SAIC Annual Report No. 1 to DTRA, SAIC-01/1039, June. (Unclassified)
- Sykes, L. R. and S. Ruggi (1986), "Soviet Underground Nuclear Testing: Inferences from Seismic Observations and Historical Perspective," Natural Resources Defense Council Report NWD 86-4, November, to be published in Nuclear Weapons Databook, Vol IV. (Unclassified)

**DISTRIBUTION LIST**  
**DTRA-TR-03-3**

**DEPARTMENT OF DEFENSE**

DEFENSE TECHNICAL INFORMATION CENTER  
8725 JOHN J. KINGMAN ROAD, SUITE 0944  
FT. BELVOIR, VA 22060-6201  
2 CYS ATTN: DTIC/OCA

DEFENSE THREAT REDUCTION AGENCY  
8725 JOHN J. KINGMAN ROAD STOP 6201  
FT. BELVOIR, VA 22060-6218  
2 CYS ATTN: TDND/D. BARBER

**DEPARTMENT OF DEFENSE CONTRACTORS**

ITT INDUSTRIES  
ITT SYSTEMS CORPORATION  
1680 TEXAS STREET, SE  
KIRTLAND AFB, NM 87117-5669  
2 CYS ATTN: DTRIAC  
ATTN: DARE

SCIENCE APPLICATIONS INTERNATIONAL  
CORPORATION  
10260 CAMPUS POINT DRIVE  
SAN DIEGO, CA 92121  
ATTN: J.L. STEVENS